2011

DEVELOPMENT OF PHYSIOLOGIC CONTACT MODELS FOR ARTICULAR SURFACES

John Owen
Virginia Commonwealth University

DEVELOPMENT OF PHYSIOLOGIC CONTACT MODELS FOR ARTICULAR SURFACES

A thesis submitted in partial fulfillment of the requirements for the degree of
Masters of Science in Biomedical Engineering at Virginia Commonwealth University.

By

JOHN RUSSELL OWEN
B.S., University of Virginia, 1981

Director: JENNIFER S. WAYNE, PHD
Departments of Biomedical Engineering and Orthopaedic Surgery

Virginia Commonwealth University
Richmond, Virginia
May 2011

ACKNOWLEDGEMENTS

First and foremost, I thank my God for good health and the stamina to do this work. However, I am very aware that my hard work is not the sole reason for me completing the work presented in this thesis. My success in this endeavor has been ensured by the support of many people. First, I wish to thank Drs. Adelaar, Wayne, and Zuelzer for taking a chance twelve years ago on this engineer from an unrelated field. I've greatly enjoyed working with you and have learned so much. Thank you all for supporting my graduate studies and for your encouragement. Dr. Wayne, thank you for mentoring me and patiently helping me to grow professionally. I pray that we will be conducting research together for many years to come. Also, thanks to Dr. Wayne's other graduate students (Ben, Casey, Christian, Corrie, Joseph, Karin, Kelly, Kevin, Meade, Mike, Pete, and Ruchi) for accepting this out-of-time student as one of their peers. It has been a joy to be a part of the same team with you. Special thanks go out to Meade for teaching me some tricks in pulling this document together. Your help is much appreciated.

Certainly, I could not have succeeded without the support of my family. Thank you Fran for recognizing years ago how, in your words, I "light up" when I talk about anything biomedical, for believing in me, encouraging me to pursue my interests, and for supporting me in so many ways. You are a wonderful wife and help make all of life enjoyable. Thanks also to my sons (Pete and Will), daughter-in-law (Kim), and grandson (PJ) for believing in me and for giving me the space and time to do the work required of me. And finally thanks to my mother (Jessamine Owen) for being my greatest fan. I dedicate this work in memory of you.

TABLE OF CONTENTS

LIST OF TABLES

Page

LIST OF FIGURES

Page

LIST OF ABREVIATIONS

ACT – Autologous chondrocyte transplantation
CS – Condroitin sulfate
E – Young's elastic modulus
ECM – Extracellular matrix
FEM – Finite element methods or models
Ha – Aggregate modulus
IMP – Impermeable rigid loading surface
k – Permeability
KS – Keratin sulfate
MACT –Matrix-associated autologous chondrocyte transplantation
MD/DP – Middle and deep zones in articular cartilage
NLGEOM – Nonlinear geometry
NORM-TC – Normal cartilage with STZ and MD/DP defined with TC properties
NORM-TC-TOP – Normal loading surface with TC properties
NORM-TI – Normal cartilage with STZ defined as transversely isotropic
NRM – Shorter abbreviation for NORM-TC-TOP
OA – Osteoarthritis
PAR – Parabolically distributed pressure
PER – Permeable rigid loading surface
REP-TC – Repair without STZ covering; surrounding normal STZ and MD/DP with TC properties
REP-TI – Repair without STZ covering; surrounding normal STZ defined as TI
REPwSTZ-TC – Repair with STZ covering with TC properties
REPwSTZ-TI – Repair with STZ covering defined as TI
STZ – Superficial tangential zone
Tc – Chemical-expansion stress
TC – Tension-compression nonlinearity
TI – Tranversely isotropic
π – Donnan osmotic pressure
ν – Poisson's ratio

ABSTRACT

DEVELOPMENT OF PHYSIOLOGIC CONTACT MODELS FOR ARTICULAR SURFACES

By: John Russell Owen, B.S.

A thesis submitted in partial fulfillment of the requirements for the degree of Masters of Science in Biomedical Engineering at Virginia Commonwealth University.

Major Director: Jennifer S. Wayne, PhD

Professor, Biomedical Engineering and Orthopaedic Surgery;

Director, Orthopaedic Research

The superficial tangential zone (STZ) plays a significant role in normal articular cartilage's ability to support loads and retain fluids. To date, tissue engineering efforts have not replicated normal STZ function in cartilage repairs. Finite element models were developed to examine the STZ's role in normal and repaired articular surfaces under different contact conditions. Models were developed by incrementally adding improvements which culminated in contact loading of curved models by permeable and impermeable rigid surfaces and a normal cartilage layer. In the normal STZ, permeability was strain-dependent on volumetric strain; tension-compression nonlinearity modeled collagen behavior. Nonlinear geometry accounted for finite deformation. Results showed that STZ properties of sufficient quality maybe critical for the survival of transplanted constructs in vivo. As compared to rigid surfaces, loading via normal cartilage provided more physiologic results. These models can provide guidance in identifying critical features for the design of tissue engineered articular cartilage constructs.

1. INTRODUCTION

1.1. CARTILAGE FUNCTION

1.1.1. Normal Cartilage

Articular cartilage is a thin white covering found on the ends of bones in joints. The purpose of this covering is to transmit loads across the joints while freely allowing sliding and rolling motion of the bone ends relative to each other. Load bearing joints such as the hip and knee are regularly loaded during normal activities to forces as high as six times body weight,[1-3] and they do this in a nearly frictionless manner for many years. Amazingly, the function of normal articular cartilage under such demanding conditions is not perceived by a healthy individual and therefore is often taken for granted. In the early stages of articular cartilage disease, known generally as arthritis, a person may still not be able to sense the effect of disease on cartilage's ability to function. As the disease progresses however, some pain and limitation in mobility will become noticeable. Those with highly progressed stages of arthritis may even become immobilized due to physical limitations of the diseased joints and the associated pain. Albeit after-the-fact, this loss of normal function heightens an awareness of the importance of healthy cartilage to the affected person. When considering the demands that articular cartilage must withstand on a daily basis, and the fact that it is required to do this for a lifetime, it becomes apparent that it is not simply a covering over the ends of bones in joints.

Several features of articular cartilage reveal that it is in fact a heterogeneous tissue of complex design and sophisticated function. First, articular cartilage is compositionally diverse.

It consists of a permeable solid phase that is filled with about four times as much water by weight. The solid portion, or extracellular matrix (ECM), consists primarily of proteoglycans and collagens arranged with heterogeneous variations of composition and organization throughout the cartilage thickness. The most prevalent component of the ECM is collagen, which accounts for about 60 to 85% of articular cartilage's dry weight [4]. Several types of collagen exist in articular cartilage with Type II being the predominant type, ranging from ≤80% of all of the collagens in immature articular cartilage to ≥90% in mature articular cartilage [5]. Of the other types of collagen present in articular cartilage, Type IX collagen adds to the structural integrity of Type II collagen by cross-linking with the longer Type II fibrils and with other Type IX fibrils [6,7].

Type II collagen fibrils in the resulting network vary in fibril diameter and directional organization throughout the thickness of mature articular cartilage (Figure 1.1-1). The calcified zone is at the border between subchondral bone and articular cartilage. In this zone, collagen fibrils are anchored to the bone by hard apatitic salts. In the deep zone, immediately adjacent to the calcified zone, collagen fibril diameters are at their largest and the fibrils primarily radiate outward from the bone and perpendicular to the articular surface. Superior to this region, in the middle zone, the fibril diameters are somewhat smaller and their orientation becomes randomized. In the region closest to the articular surface, the superficial tangential zone (STZ), the collagen concentration is highest, the fibril diameters are the smallest and the fibrils are oriented primarily parallel to the surface [8-10]. Some of these variations play unique roles in the function of articular cartilage, and will be discussed as other factors that interact with collagen are later described. In general, the collagen fiber network in articular cartilage is somewhat

analogous to steel reinforcing bar within concrete in that the collagen network is capable of resisting tensile stresses and strains to which articular cartilage is subjected.

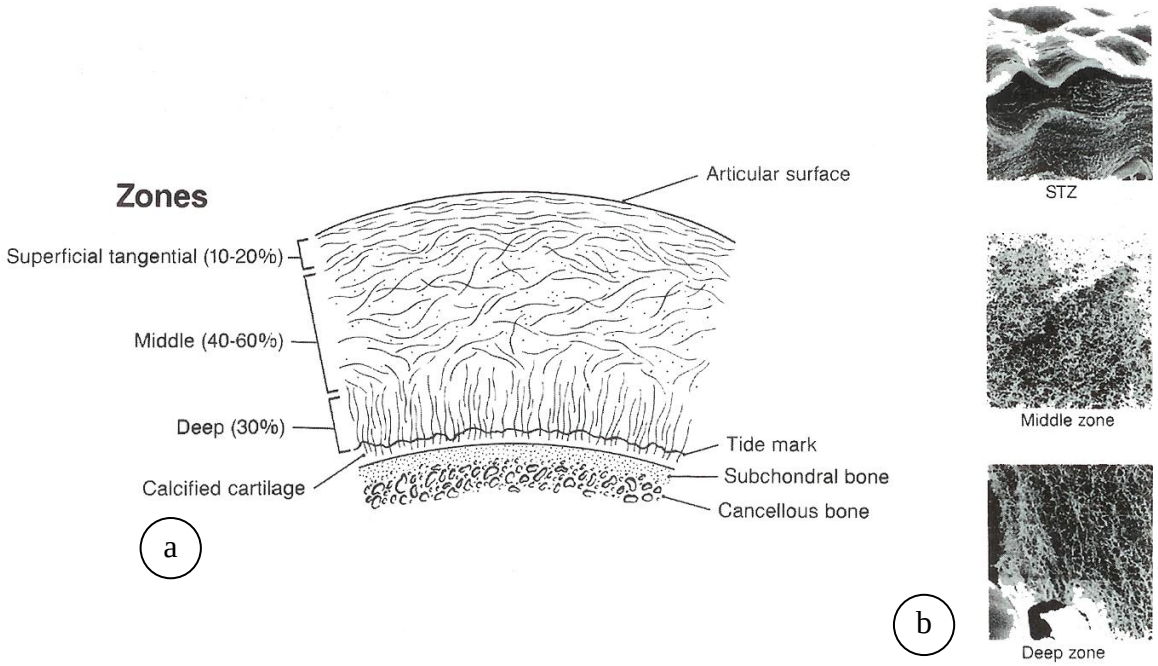

Figure 1.1-1: Collagen directional variations through the thickness of normal articular cartilage described in four zones: STZ, Middle, Deep, and Calcified Zones a) illustrated by artist's depiction, and b) observed via scanning electron microscopic [10].

Proteoglycans represent the other major component of ECM, and consists of certain building blocks. First, an aggrecan molecule is formed when keratin sulfate (KS) and condroitin sulfate (CS) glycosaminoglycan chains attach to a large protein core (Figure 1.1-2) [11-13].

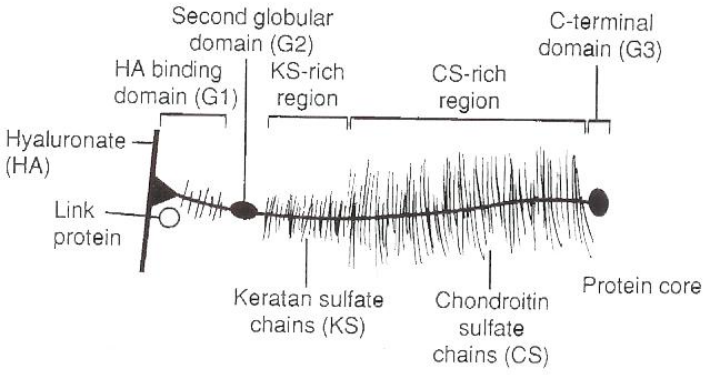

Figure 1.1-2: Illustration of an aggrecan molecule consisting of KS and CS glycosaminoglycan chains bound to a hyaluronate chain [14].

A single proteoglycan aggregate macromolecule is formed by as many as 200 individual aggrecan molecules attached to a continuous chain of hyaluronate (Figure 1.1-3) [15]. These long assemblies are effectively intertwined within the collagen fiber network such that movement of proteoglycans is restricted.

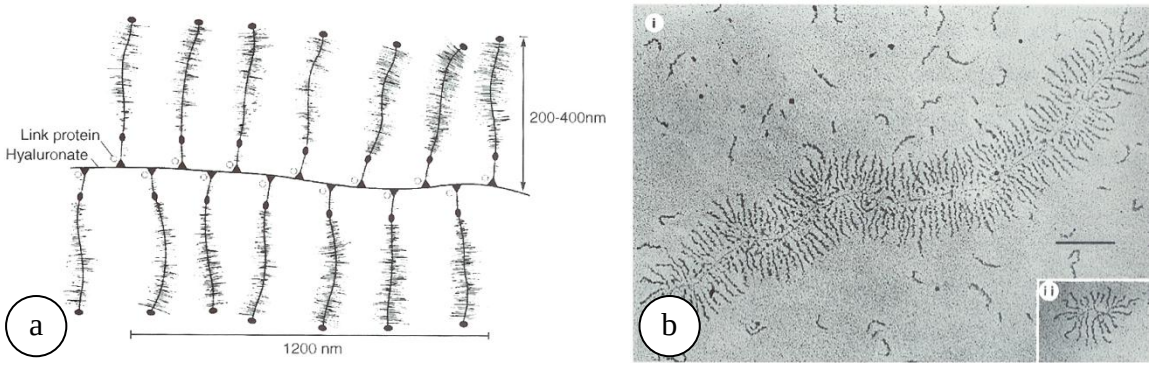

Figure 1.1-3: A proteoglycan aggregate macromolecule formed by many aggrecan molecules binding to a hyaluronate chain. a) artist's illustration, and b) scanning electron microscopic image showing a macromolecule relatively immobilized within skeletally immature (i) and mature (ii) bovine articular cartilage [15].

A major contribution of proteoglycans to the normal function of articular cartilage is its ability to resist compressive stresses and strains. The material composition of proteoglycans contributes in this regard, but not alone. The ECM's ability to resist compressive stresses and strains is largely a result of two electro-chemical phenomena. Both of which are dependent on

fixed negative electrical charges that occur on the glycosaminoglycan chains of the proteoglycan aggregates. First, in normal articular cartilage, proteoglycans are forced into a space of about one-fifth the volume that they occupy in free solution. The repulsive forces between negatively charged glycosaminoglycan chains, held in close proximity to one another, cause a swelling pressure referred to as the chemical-expansion stress (Tc). This swelling pressure expands the ECM and effectively tensions the collagen fiber network within which the proteoglycans are dispersed. When articular cartilage experiences compressive stresses and strains, the fixed negative charges are forced into even closer proximity thereby increasing resistance to counter the applied forces [16].

The second phenomenon, Donnan osmotic pressure (π), is due to interaction between the fixed charges on proteoglycans and positively charged counter-ions from fluid surrounding articular cartilage. In a tendency towards electroneutrality, negatively charged proteoglycans draw positively charged counter-ions, such as Ca^{2+} and Na^{+}, into the tissue from surrounding fluid. This creates an imbalance in counter-ion concentration between the tissue and the fluid and generates an osmotic pressure gradient into the tissue which seeks to balance osmolarities of the fluid and tissue. The negative fixed charges within the tissue essentially dictate the concentration of positively charged counter-ions in the tissue, regardless of surrounding fluid counter-ion concentration. Since counter-ion concentration within the fluid can change, it is the main factor driving the osmotic pressure gradient. Thus, a lower concentration of counter-ions in the surrounding fluid results in a higher osmotic pressure gradient. The effect of this is that a very salty solution surrounding the cartilage easily supplies the tissue with the required counter-ions without greatly reducing the counter-ion concentration within the fluid. Therefore, the osmotic pressure gradient would be small and the tissue would experience less swelling. If the

solution had a very low salt content, then a very large disparity in counter-ion concentrations would exist between the tissue and the surrounding fluid causing the osmotic pressure gradient to be very high. This would drive fluid into the tissue and make it swell [17]. Interestingly, the counter-ion concentration in the surrounding fluid also has an effect in modulating the chemical-expansion pressure such that Tc decreases exponentially with increasing fluid ion concentration[18].

As with collagen, there are also zonal variations of proteoglycans across the thickness of articular cartilage. In the calcified zone, proteoglycans are encrusted in the apatitic salts along with collagen; thereby, providing additional anchoring to the subchondral bone. Proteoglycan concentration varies through the remaining zones in a manner inversely proportional to that of collagen, with the highest concentration of proteoglycans occurring in the deep zone and decreasing through the thickness to its' lowest concentration in the STZ[19].

While previously described variations of the ECM play unique roles in the load carrying ability of articular cartilage, the ECM alone cannot support the demanding loads required of articular cartilage. The balance of the tensile and swelling forces within the ECM and the hydrophilic nature of proteoglycans enable cartilage to retain a significant proportion of water, varying from about 65% in the deep zone to about 80% in the STZ. Due to the permeable nature of the ECM, water content can change locally in response to stresses and strains within the ECM. Yet, permeability of the ECM is very low and significantly restricts fluid flow within cartilage. This permeability exponentially decreases with strain for full thickness cartilage [20-22] and has been separately quantified within the STZ, middle, and deep zonal regions [23,24]. Because of this nonlinear relationship, even greater resistance to fluid flow occurs with compressive deformation such that the ECM effectively restricts fluid flow and generates significant fluid pressure within

the tissue. Thus, fluid pressure contributes significantly in a unique load sharing relationship with articular cartilage's solid matrix allowing support of the demanding loads to which cartilage is subjected [25-27].

While the solid and fluid phases are critical to the biomechanical function of articular cartilage, chondrocytes are vital to the formation and maintenance of the tissue itself. As the only cells within articular cartilage, chondrocytes are embedded within the ECM. Though conventional thinking has been that the chondrocytes are fixed within the ECM, there is growing evidence that some motility exists, albeit virtually none as compared to other cells in the body [28]. Similar to collagen and proteoglycans, variations occur for chondrocytes throughout cartilage thickness in terms of concentration, shape, and organization. In the deep zone, chondrocytes are spherically shaped and tend to be arranged in columns (Figure 1.1-4). In the middle zone, the arrangement is more random with the cell shape still round but showing some signs of irregularity. In the superficial tangential zone, the chondrocytes are somewhat elongated in a direction parallel to the surface and packed a little closer together. Because of the avascular, aneural, and anerobic environment found in articular cartilage, chondrocytes function largely in response to mechanical, fluid pressure, and chemical signals. Under normal conditions, the chondrocytes are able to maintain the fine balance of ECM degradation and new tissue synthesis. Unfortunately when the balance of these cellular cues is thrown off by injury or disease, the chondrocytes alone often are not able to effectively repair the tissue [29].

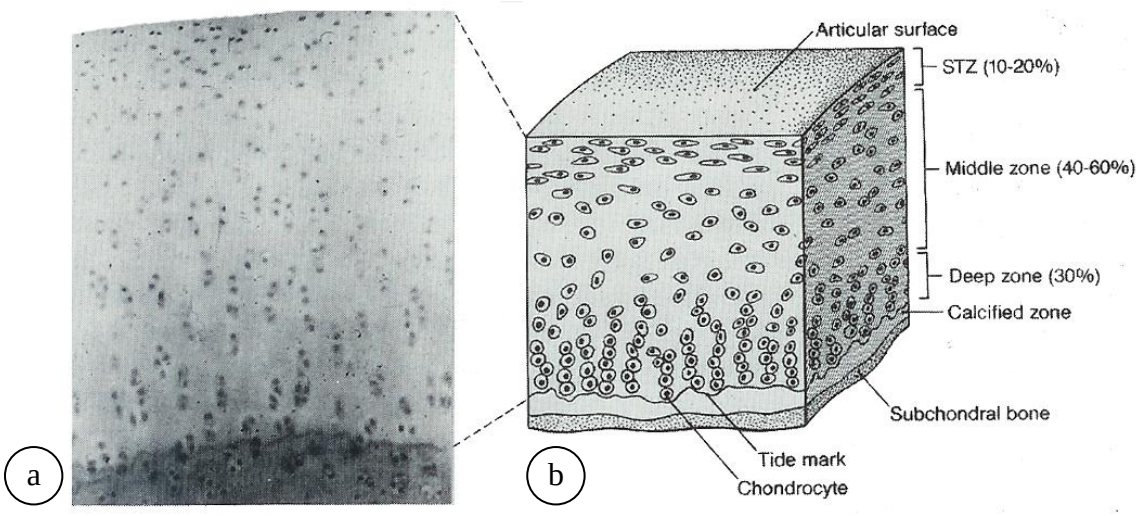

Figure 1.1-4: Variations of cellular shape and distribution through the thickness of articular cartilage as shown by a) histologic section of normal adult cartilage and b) an artist's illustration[10].

1.1.2. Disease and Injury of Cartilage

In the early stages of injury or disease, fraying of the articular surface may be observed. As the fraying progresses, cracks develop in the surface and go deeper into the cartilage. This compromises the ability of the collagen matrix to retain proteoglycans. Without sufficient restraint from the collagen network, proteoglycans expand causing the water content within the cartilage to increase greatly and allowing the loss of proteoglycans from the cartilage. In response, chondrocytes become more active. But due to their relative immobility, newly synthesized material tends to cluster around the chondrocytes and does not migrate into defects. Thus, defects are not filled with new ECM tissue. As cracks progress, so does chondrocytic cell death and articular cartilage begins to tear away and expose underlying subchondral bone. Exposure of bone generates significant pain as bone rubs together causing eburnation (i.e. hardening of the bony surface) and/or erosion of bone with bleeding. The body's inflammatory response causes clotting of the blood that fills the defect. However, the clot turns into fibrous tissue composed primarily of Type I collagen. This tissue is functionally inferior as it does not

reproduce the compositional nor structural features of normal articular cartilage. Thus, it often fails and joint replacement is a last resort solution to eliminate debilitating pain and restore mobility to the affected joint [29].

The order of events progressing from the healthy state to this permanently dysfunctional condition is not fully understood and can vary. Factors have been identified which correlate to higher incidences of osteoarthritis (OA) but are not definite predictors of the condition. For instance, there is a higher incidence of OA in the elderly population but not all elderly people succumb to it and it is also present to a lesser degree in young people. Genetic predisposition is a factor in some people whose collagen structure is altered relative to the normal population. Abnormal metabolic activity of chondrocytes in individuals with OA suggests that it may also be a factor of causation for the disease, or it may be simply a marker of other factors at play; such as altered physical conditions (e.g. stress, strain, osmotic pressure) within the solid matrix that are affecting the chondrocyte [14]. Also, arthritis can have nothing to do with events in the cartilage itself but caused secondarily by other inflammatory processes [30]. In that instance, it is referred to as rheumatoid arthristis. In any event, the process by which the diseased state is reached is a complex one beginning with disturbance of the fine balance that exists within normal healthy cartilage. Without appreciable intervention, the complexity of that process typically prevents successful recovery from the diseased state.

1.1.3. Repair of Defective Cartilage

Given articular cartilage's insufficient capacity for self-repair, various intervention techniques have been developed with the hopes of achieving successful repairs. For shallow defects, debridement involves scrapping of the articular cartilage surface to smooth out damaged areas with the hope of magnifying the repair response of underlying chondrocytes such that the

cartilage can repair itself, but this has limited benefit [31]. For full thickness defects, abrasion of subchondral bone via a burr, drilling of multiple holes into the bone, or microfractures in the bone via an awl are techniques designed to cause bleeding from the bone marrow into the cartilage defect. Large amounts of progenitor cells contained in the blood help to develop scar tissue within the defect, but as previously discussed, the resulting fibrous scar tissue does not replicate compositional and structural characteristics of normal articular cartilage [31].

Mosaicplasty seeks to fill defects with cylindrical sections of undamaged cartilage and bone transplanted from nonweightbearing areas. These autologous osteochondral cores are typically transplanted from the medial and lateral edges of the ipsilateral femoral trochlea. Sometimes, cores are taken from the contralateral joint, and occasionally from the intercondylar notch [32]. For successful grafts, bone integrates well with surrounding bone and the grafted cartilage maintains its' compositional and structural integrity while the bleeding response of the subchondral bone fills gaps between grafts with fibrous scar tissue. However, the procedure is challenging as the surgeon tries to match cartilage thickness of grafts with surrounding tissue while maintaining curvature and continuity of the articular surface. Also, the surgeon must take care to insert the graft with an "optimal" press-fit interference. Too little interference can allow micromotion while too much can cause deterioration of bone; both extremes result in poor bone-to-bone healing. Paired with the issue of press-fit is the need to moderate pressure applied on the cartilage while inserting the graft. Too much pressure can result in chondrocyte cell death leading to graft failure. Finally, the defect size that this procedure can fill is limited by the availability of autologous donor tissue [32].

Another approach has been to cover the defect site with an autologous graft of periosteum. The graft is typically attached over the defect with sutures such that the cambium

(i.e. inner) layer of the periosteal graft faces into the defect. Thus, progenitor cells that are present in the cambium layer are made available to encourage growth of new tissue in the defect. Additionally, the graft serves as a substrate onto which new tissue may attach and contains growth factors that can be beneficial to new tissue development [33]. Continuous passive motion during rehabilitation encourages new tissue growth [34]. While the tough outer fibrous layer provides some physical protection against articulation, this motion must be carefully managed to protect the graft from detachment.

Autologous chondrocyte transplantation (ACT) is a variation of this procedure that was developed to increase the concentration of cells available for new tissue development. Following the steps of the first generation ACT procedure [35], arthroscopy is performed to harvest normal articular cartilage from a minimum weightbearing area. Chondrocytes are then extracted and cultured in-vitro for two to three weeks until transplantation. At the time of surgery, a periosteal graft is sewn over the defect, as previously described, and the cultured suspension containing approximately 2.6 to 5 million cells is injected underneath the graft [35] (Figure 1.1-5).

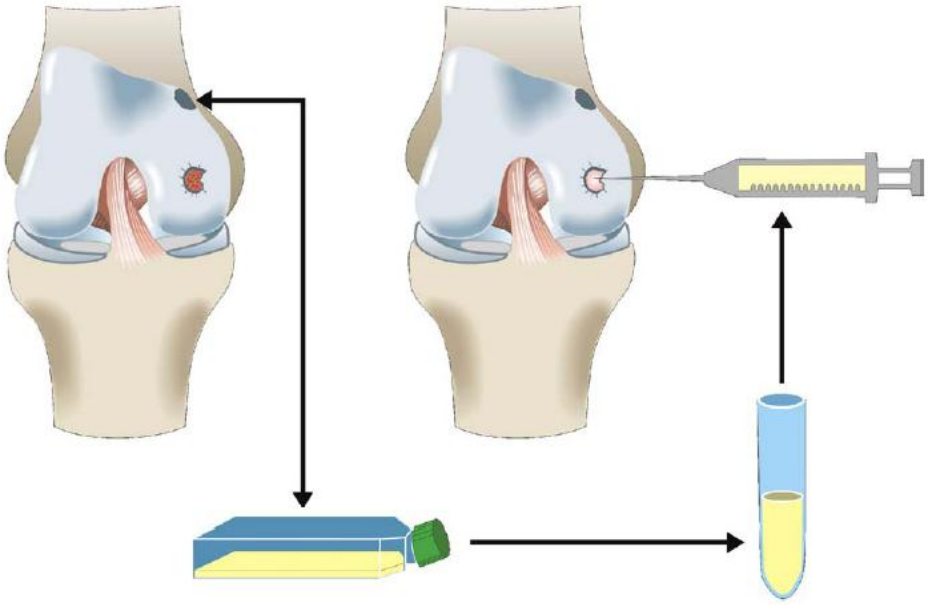

Figure 1.1-5: Illustration of the 1st generation autologous chondrocyte transplantation procedure [36].

Some success has been reported with this approach [37], but graft limitations previously described still exist. There is the possibility for the cell solution to leak out of the defect in regions of the periosteal graft edge not sutured to the cartilage, and joint stiffness is not an uncommon result of the arthrotomy required to harvest the graft [31]. Careful suturing and the application of fibrin glue have been utilized by some as a way to minimize leakage [36] (Figure 1.1-6).

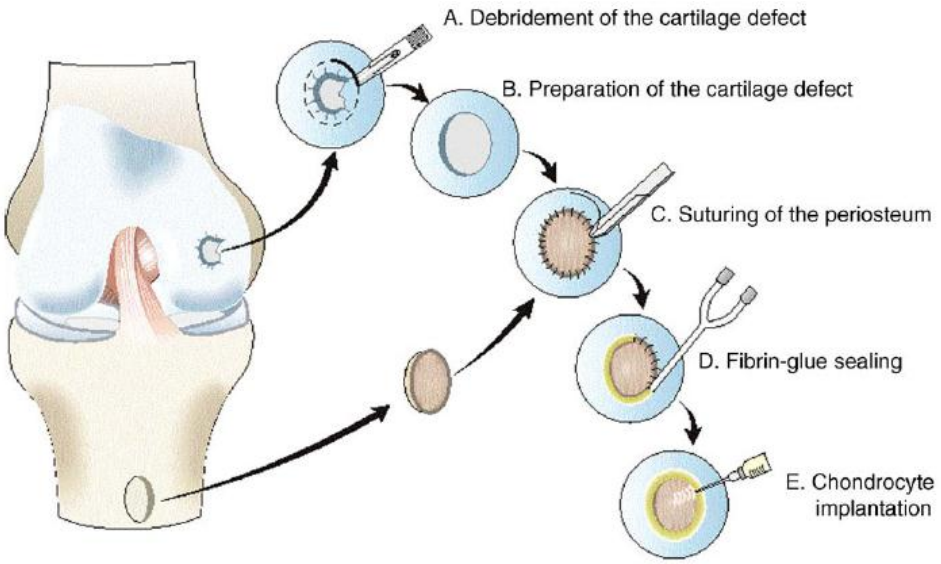

Figure 1.1-6: Illustration of careful suturing and gluing to seal the periosteal graft during autologous chondrocyte transplantation procedure to minimize leakage [36].

Additional variations of the ACT procedure have been developed with the hopes of improved results. Some have mimicked the 1st generation approach with the exception of replacing the periosteal flap with a tissue engineered collagen membrane [36] (Figure 1.1-7). This eliminates harvesting of the periosteal graft and its' associated complications.

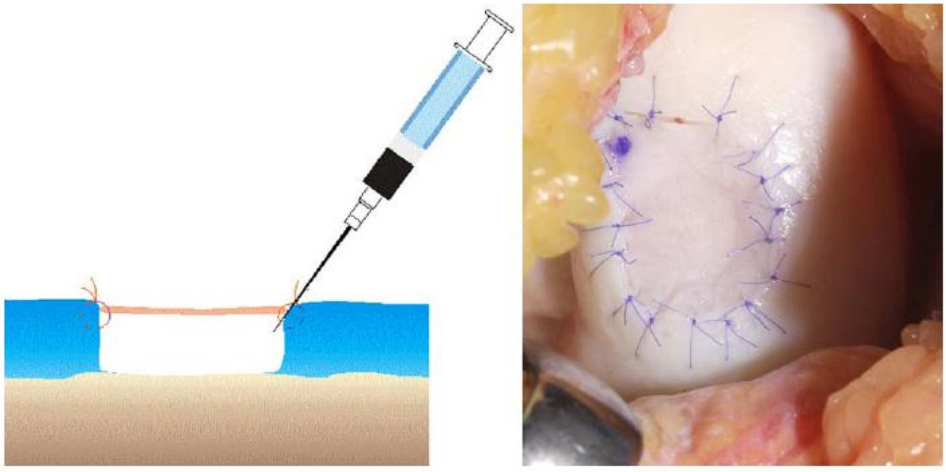

Figure 1.1-7: Example of a collagen membrane being used in place of periosteum [36].

Others have used bioabsorbable scaffolds, the type of which can vary. Harvested chondrocytes are seeded onto the scaffold prior to culturing. Later, the cultured scaffold is placed directly into the defect and secured without use of a periosteal graft [31,36] (Figure 1.1-8).

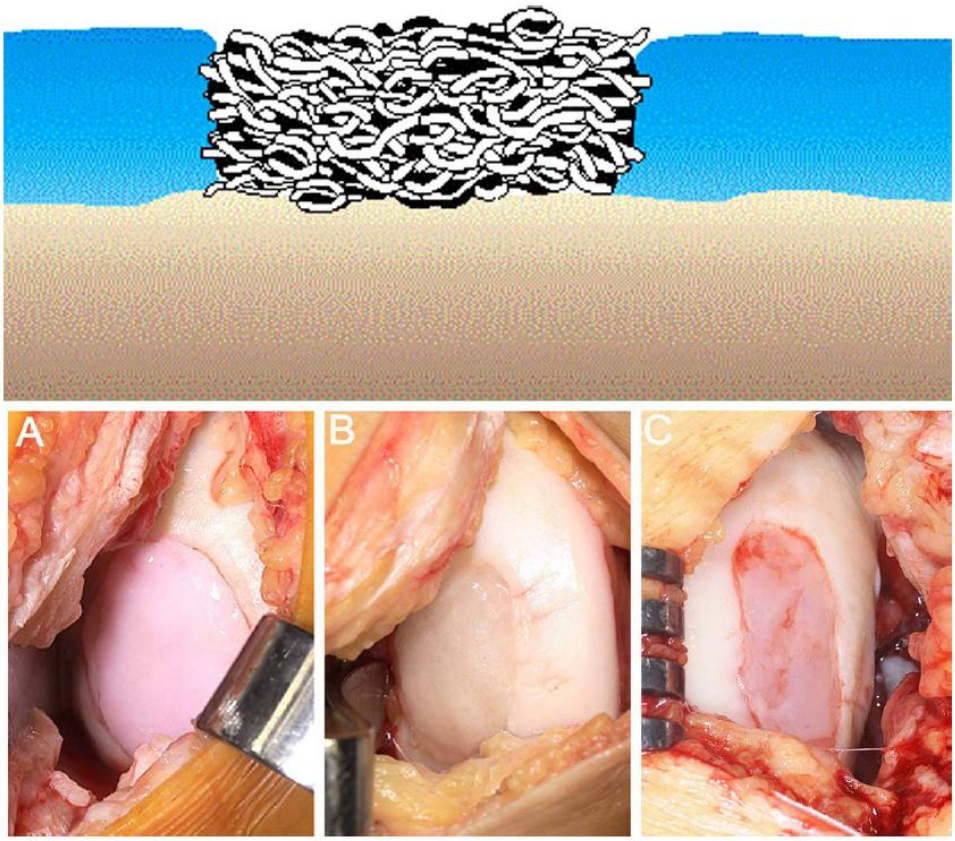

Figure 1.1-8: Tissue engineered scaffolds seeded and cultured with chondrocytes prior to implantation, cut to size and fit into the defect without a periosteal covering or fixation by sutures. top) artist's rendition, bottom: A) Matrix-associated autologous chondrocyte transplantation (MACT) using a collagen membrane (MACI™), B) a hyaluronan polymer (Hyalogryft C™) and C) a collagen gel CaReS™ [36].

Though the creation of engineered replacement tissues in vitro for the repair of articular surface defects has been a focus in recent years, it remains a challenge. It is generally appreciated that the design of engineered tissues should incorporate compositional, organizational, and mechanical features that are key to a tissue's normal function [38-40]. While efforts to create repair tissues have become more sophisticated, resulting in better outcomes, the

goal of achieving normal zonal properties in vitro or in vivo has not yet been achieved [31,41-44]. Intuition suggests that the best replacement tissue would be that which exactly replicates all normal properties; though it is very unlikely that this goal would ever be achieved prior to implantation and maturation. In reality, it appears that the best one can hope for is to achieve some of the normal properties.

This poses the question as to whether certain normal properties should be targeted for inclusion before others. Experimental studies reveal the importance of the STZ in the function of normal articular cartilage in that removal of the STZ negatively affects the remaining cartilage's ability to support axial loads, maintain fluid pressure, and retain fluid within the remaining tissue [45-47]. These findings occurred in spite of the fact that all of the remaining cartilage had perfectly normal properties and imply that engineered tissues that exactly replicate normal properties, to the exclusion of the STZ, would similarly suffer. Conversely, the impact of the STZ's absence implies that replication of STZ-like features in engineered tissues would afford benefit to those tissues, and that priority should be given to inclusion of these properties.

Still, properties which may most benefit engineered tissues initially and throughout healing remain to be identified. It has even been suggested that healing conditions may require initial material properties that differ from normal tissue [48,49]. Thus, one should avoid concluding that a particular feature, such as the STZ, should be included without first investigating the impact that it might have. A basic concern is that transplanted constructs be of sufficient mechanical quality to survive the demanding mechanical environment of the joint during the healing process. Failure to achieve this basic requirement from the moment of implantation may doom these tissues to failure, regardless of other characteristics that have been achieved. Careful

consideration of the impact that individual features can have will provide focused direction to tissue engineering efforts. As a first step, consideration of the STZ is warranted.

1.1.4. Features of the Superficial Tangential Zone

Briefly summarizing facts mentioned in prior sections will help in consideration of the STZ. Chondrocytic cells within the STZ are somewhat elongated in a direction parallel to the surface and are packed a little closer together than in the underlying zones. As compared to the middle, deep, and calcified zones, the STZ contains the lowest concentration of proteoglycans, and the highest concentration of collagen and water. Collagen fibril diameters in the STZ are the smallest and the fibrils are oriented primarily parallel to the surface. Lastly, as in the other zones, the STZ has a very low permeability that decreases exponentially with compressive strain.

Organization of collagen fibrils parallel to the articular surface within the STZ results in increased tensile stiffness in this preferred direction in comparison to a direction normal to the surface [24,50-54]. This enables the STZ to better resist radial stresses than underlying tissues. The lower proteoglycan content of the STZ means that it more easily compresses under load. However, because of the exponential relationship of permeability with strain, this compression helps to more quickly reduce permeability. Thereby, fluid flow out of the STZ is more quickly abated.

Considering variations of these features can elucidate the potential benefit that they might afford to engineered tissues. Finite element analyses can be useful in that regard.

1.2. CARTILAGE MODELING

1.2.1. Material Properties of Normal Cartilage

In order to model cartilage, a reasonable estimate of material properties is needed. Due to the complex interplay of features previously described, the response of normal articular

cartilage to loads is very dependent on the conditions of loading. Thus, various methods have been developed for assessing material properties. The most common methods used in determining compressive properties are those of confined compression, unconfined compression, and indentation (Figure 1.2-1) [55-57].

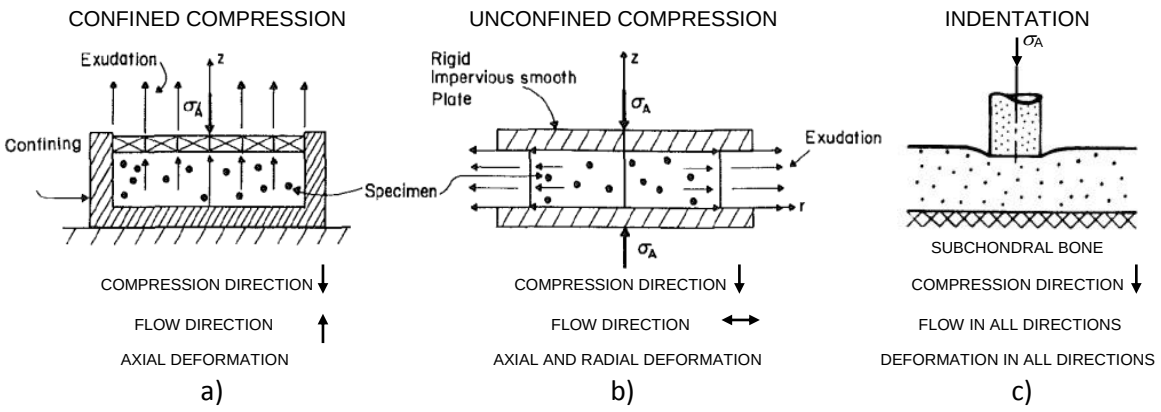

Figure 1.2-1: Three methods for assessing compressive material properties: a) confined compression, b) unconfined compression, and c) indentation [55,56].

In confined compression, the articular surface is loaded via a rigid metal filter with porosity sufficiently higher than the permeability of cartilage so as to freely allow exudation of fluid from the surface of the loaded tissue (Figure 1.2-1a). A rigid impermeable chamber prevents displacement at, and fluid flow from, the radial and base surfaces such that deformation only occurs in the direction of loading and fluid flow only occurs in the opposite direction. Only compression of the ECM occurs so that tensioning of collagen fibrils is prevented. Therefore, resistance to loading is primarily due to the inherent stiffness of the ECM and the fluid pressure that is developed from drag-induced fluid flow through the tissue. The interaction of fluid with the ECM is largely responsible for the time-dependent load response of cartilage.

In confined compression, creep and stress-relaxation are the two tests which are most commonly performed. Creep tests involve suddenly applying a step-load that is then held constant while displacement is measured over time until equilibrium occurs (Figure 1.2-2a).

Since fluid flows only out of the surface, compaction of tissue occurs first near the surface and progresses to the deeper tissue as fluid flows out over time until equilibrium is reached. Stress-relaxation involves applying a ramp displacement to a prescribed level that is then held constant until equilibrium is reached (Figure 1.2-2b). Fluid exudes from the surface only during the ramp displacement with compaction occurring primarily in the region nearest the surface. Once the displacement stops, and is held constant, fluid flow only occurs as a redistribution of fluid within the tissue until equilibrium is attained (Figure 1.2-2c). The load response occurring during the ramp displacement and relaxation is recorded. Typically, the cartilage is assumed to act like a biphasic material comprised of a homogeneous linearly elastic solid material and an incompressible fluid [58]. Analysis of the displacement versus time data yields a measure of tissue permeability (k, typically expressed in units of m^4/N-s) and the equilibrium compressive aggregate modulus (H_A, typically expressed in MPa). [57-59].

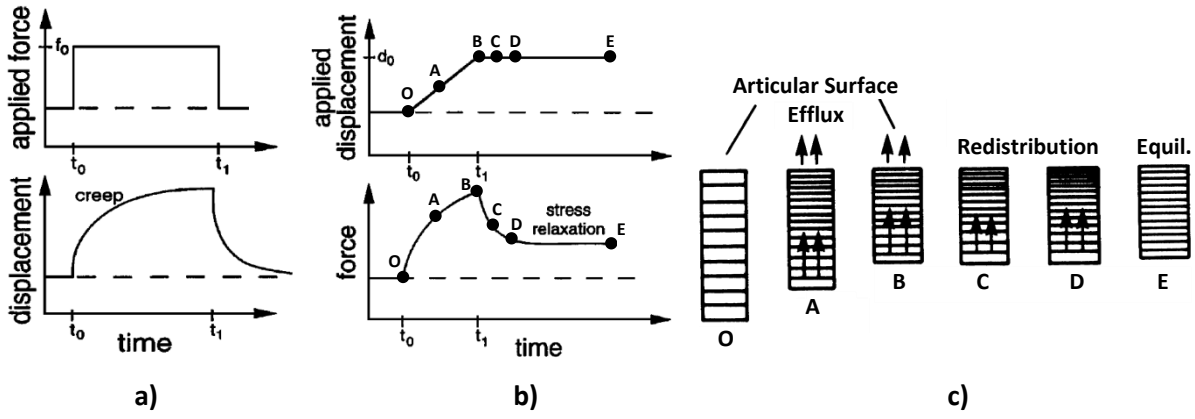

Figure 1.2-2: Time-dependent load responses: a) creep displacement after applying a sudden load and maintaining the load over time, b) stress relaxation after applying a displacement in ramp fashion and maintaining the displacement over time, c) fluid flow distribution during stress-relaxation [57,58].

In unconfined compression, the cartilage specimen is sandwiched between two rigid impermeable platens and a load is applied perpendicular to the platens. Deformation occurs in the direction of loading and radially in a direction perpendicular to the applied load (Figure

1.2-1b). Axial deformation results in compression of proteoglycans while radial expansion causes tensioning of the collagen network. Again, time-dependent creep and stress-relaxation responses are evident. As with confined compression, these tests provide a means for measuring permeability (k). In addition to confined compression, they allow measurement of Young's elastic modulus (E, typically in units of MPa) and of Poisson's ratio (ν). These parameters are related to aggregate modulus (H_A) and shear modulus (μ) by: $H_A = \frac{E(1-\nu)}{(1+\nu)(1-2\nu)}$, and $\mu = \frac{E}{2(1+\nu)}$. (Mow and Guo 2002)

Indentation testing involves pressing a metal tip onto the articular surface and recording the response in terms of load and displacement over time. Sometimes an impermeable metal tip is employed; more often a porous metal tip is used to allow fluid to freely exude from the cartilage surface under the indenter tip (Figure 1.2-1c). This method of loading results in more complex deformation and fluid flow patterns, but yields the same parameters that are typically identified with confined and unconfined compression: aggregate modulus (HA), Young's modulus (E), Poisson's ratio (ν), and permeability (k). Indentation is often preferred as it is less disruptive to tissue. Namely, cartilage is left intact on bone for in vitro test samples. Also, indentation provides the potential for assessment of cartilage properties in vivo [57,60].

Tensile properties of cartilage have been determined from uniaxial tests. Due to variation in collagen directional orientation, as well as organizational changes through cartilage thickness, tensile properties are dependent on specimen orientation and location (Figure 1.2-3a,b). The stress-strain response is nonlinear for tensile specimens since collagen fibers are progressively brought into alignment with the direction of load as the load increases (Figure 1.2-3c) [51,57,61]. These tests help describe anisotropic variations present in normal cartilage.

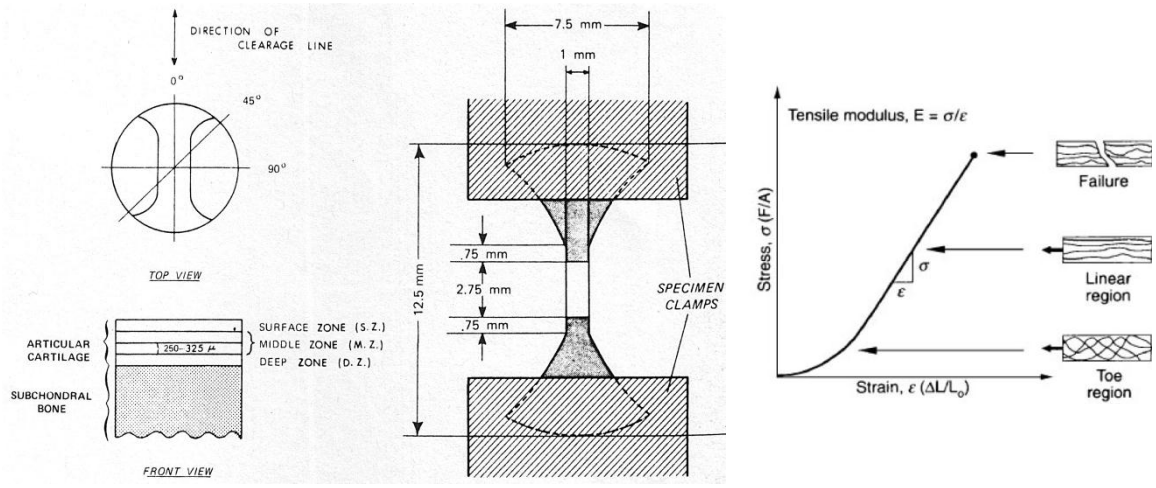

Figure 1.2-3: a) Schematics of specimen preparation for b) uniaxial tensile testing of articular cartilage, and c) a characteristic stress-strain relationship for articular cartilage in a steady strain-rate tensile experiment [57,61].

Adaptations of the above methods have been developed to further characterize these variations. For example, optical microscopy has been used in conjunction with unconfined compression to demonstrate variations in Young's modulus and Poisson's ratio in three orthogonal directions. [62,63] Others have used polarized light microscopy to correlate variations in material properties with anisotropic collagen organization [64-67]. Ultrasound also has been studied as a noninvasive way to evaluate articular cartilage viability [68-70], while some have investigated MRI as a noninvasive way to determine material properties [71-74]. The result of these efforts is a vast amount of information from which to select material properties that can be used in finite element models.

1.2.2. Modeling Approaches

In general, when creating finite element models (FEM) to solve engineering problems, one is always faced with decisions as to which complexities to include that will address features critical to the behavior being modeled and which simplifying assumptions to incorporate that

will make the solution more tractable and minimize the computational work required. The end result should be an efficient model that appropriately predicts behavior within the scope of the application. More specifically, this is the objective in the development of finite element models pertaining to the behavior of articular cartilage.

At the most basic level, some have modeled articular cartilage as simply a single-phase linearly elastic isotropic solid material (i.e. without accounting for fluid contributions). This simple approach may be appropriate when the time-dependent nature of cartilage is relatively unimportant to the problem being solved. For instance, some have taken this approach in joint implant design when the focus has been primarily on stress and strain in underlying bone [75]. In regards to cartilage, this may at times be appropriate because cartilage's low permeability can make it act like a single-phase material for short static loads, moderate to high frequency loads, or in its' middle and deep zones where fluid movement is minimal [76]. For example, this simple approach has been deemed appropriate by some for interpreting in situ and in vivo indentation data for instantaneous stiffness and equilibrium modulus [77]. Further, it has been shown to be appropriate in general cases for short-term loading responses before fluid flow effects contribute significantly [78].

When time-dependent characteristics are important, two basic approaches have been taken: 1) modeling cartilage as poroelastic; that is, as a porous solid whose pores are filled with liquid, or 2) modeling cartilage as a mixture of solid and liquid phases. The first approach is based on theory initially developed specifically for one-dimensional compression in soil mechanics [79], and later generalized for three-dimensional deformation of porous materials [80]. The second approach is based on mixture theory where cartilage is represented as a mixture of different material phases. The first application of mixture theory to cartilage was in the

treatment of cartilage as a biphasic mixture of solid and liquid [58]. While the poroelastic and mixture theory approaches differ in mathematical treatment, they afford comparable results when modeling cartilage and are accepted as equivalent approaches [81]. They both allow modeling of tissue permeability, fluid pressure, and the effects of fluid movement within cartilage. Thereby, time-dependent effects can be modeled, as well as short-term loading responses and equilibrium states.

In addition to time-dependent effects, stiffness anisotropies due to collagen fibril orientation have been included by various approaches. Some have modeled full cartilage thicknesses as transversely isotropic [82-86]. Others have modeled just the portion of models adjacent to the surface as transversely isotropic to simulate the higher tensile stiffness of the STZ and the underlying portion as isotropic to approximate the middle and deep zones [66]. Thereby, higher tensile stiffness experienced in directions parallel to articular surfaces due to collagen fiber orientation have been approximated. Transversely isotropic models can be suitable when stress and strain in the plane of higher stiffness are predominately tensile. However, if compressive loads are experienced in this plane, the higher modulus used in transverse isotropy would still be applied resulting in less reliable stress and strain predictions. Some have addressed this limitation through the use of cone-wise linear isotropy [87]. In this approach, the cartilage solid is defined as bilinearly isotropic where the stress-strain relationship is defined by different moduli of linear elasticity in compression and tension [88]. In this manner, a region of interest such as the STZ can be defined to have greater stiffness in tension than in compression.

Still others have sought to increase levels of material anisotropy by modeling collagen fibrils as a third constituent in a poroelastic solid filled with liquid. In these fibril-reinforced models, collagen fibrils are modeled as spring elements that can only support tension and are

aligned within the model to simulate natural fibril orientations [89-91]. Other nonlinearities related to solid materials have been added alone or in combination with approaches previously described; such as, viscoelasticity [92-94] and hyperelasticity [95,96].

Additional nonlinearities have also been addressed. As previously mentioned tissue permeability varies exponentially with strain in cartilage. Models including strain dependent permeability have shown better agreement with experimental results [97-101]. Geometric nonlinearity has been included by some to address finite deformation that occurs in some loading scenarios [102]. Finally, nonlinearities due to boundary conditions have been modeled with changing contact area between loading surfaces and flow restrictions in some areas [83,103-105].

1.2.3. Models of Repairing Cartilage

While much has been done to develop computational models approximating normal articular cartilage behavior, a limited number of studies has been published which focus on repaired states. The aim of those studies have varied from modeling experimental tests of homogenous repair tissues under load[106,107], understanding fluid flow and pressure influences in cartilage defects filled with agarose gel [108], investigating parameters affecting in vitro assessment of repair tissue properties [109-111], understanding parameters important to successful osteochondral plug transplantation [112,113], predicting new tissue growth in full thickness defects [114], to developing clinical tools for assessment of repairs [115]. Despite the documented importance of the STZ to normal cartilage, models have only begun to study the effects of an STZ on the mechanical environment of underlying repair tissues. Finite element models have predicted excessive axial deformation of repair cartilage without the STZ [106,116], but none have specifically modeled the benefit that normal STZ properties can have on repairing cartilage. The inclusion of an STZ may be a critical element for success of cartilage repairs. Thus, models simulating the

STZ's effect on underlying repair tissues can be beneficial in providing guidance to tissue engineers seeking to design replacement tissues.

1.3. OBJECTIVE

It was the objective of this thesis to develop computational contact models that can elucidate the effect that the STZ can have on underlying repair tissues and provide guidance to tissue engineers in identifying parameters for inclusion in repair tissues. ABAQUS® (Dassault Systèmes Simulia Corporation, Warwick, RI), a commercially available software that has been validated for use in modeling the biphasic nature of cartilage as a poroelastic tissue [117], was used here to develop these models. User-defined FORTRAN code was written to supplement the ABAQUS software as needed. The solution to the stated objective was developed incrementally beginning with a simple 2D axi-symmetric model of a flat articular surface loaded by a constant parabolic pressure distribution, proceeding to flat and concave models loaded by permeable and impermeable rigid surfaces, and ending with contact between two incongruent deformable layers for different repair models. The pros and cons of the added complexities will be discussed as each development is presented.

2. MODELS INVESTIGATED

2.1. OVERVIEW

This chapter describes models developed in this thesis to explore the influence that higher tensile stiffness and strain dependent permeability in the STZ can have on the behavior of normal and repaired articular surfaces. In general for all models, the relative response to load was of interest for three cartilage layer types representing a normal cartilage layer, a full thickness defect filled with inferior repair tissue, and a defect filled with the same inferior repair tissue but covered with a normal STZ covering. Model geometry, material property definitions, and loading conditions were the elements varied during development which resulted in model improvements.

ABAQUS (Dassault Systèmes Simulia Corporation, Warwick, RI) finite element analysis software was used to develop and analyze all models. The ABAQUS/CAE software interface was used to build the models and to assign material properties to specific regions. Input file code was generated for each model via ABAQUS/CAE; then ABAQUS/STANDARD was used to run the analyses. User-defined FORTRAN code specific to each model was written and called upon as needed by ABAQUS/STANDARD during the analyses. Post-processing of output files was facilitated via ABAQUS/CAE to extract data from the results and to generate contour and vector plot images representing variations in parameters of interest (e.g. stress, strain, fluid pressure, etc.).

2.2. GEOMETRY OF SURFACES TO BE LOADED

2.2.1. Flat Cartilage Layers - Geometry

A 2D axisymmetric structure, 1mm thick and 12mm in radius, was developed to represent the radial cross-section for all of the flat articular cartilage layers modeled (Figure 2.2-1). The thickness was partitioned into regions simulating zones naturally occurring within cartilage. The top 20% (0.2mm) of the 1mm layer thickness represented the STZ, while the remaining 80% (0.8mm) defined the combined middle and deep zones (MD/DP). Radially, a partition was placed at 3mm to facilitate simulation of a repair cartilage plug in the specific repair models. Other partition lines were added to facilitate desired variations in the finite element mesh. Mesh convergence was assessed during initial model development revealing that further reducing the chosen element sizes had little impact on overall results. Mesh size was further refined in areas where more localized predictions were desired or where larger gradients were expected in parameters of interest.

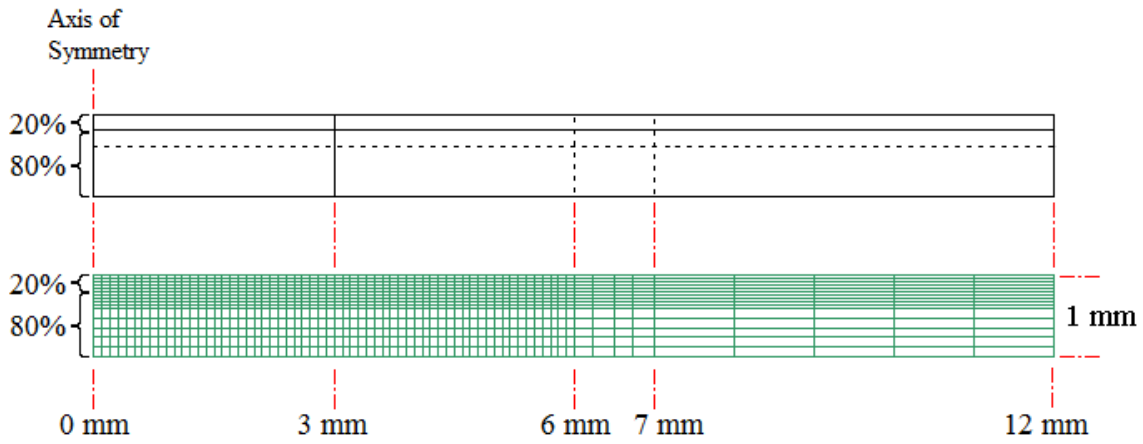

Figure 2.2-1: Finite element model dimensions and applied mesh. Partition lines are shown in the top image where solid lines represent those which facilitate material property assignments, and dashed lines facilitate mesh variations.

The thickness was divided into 15 elements; five 0.04mm thick elements were placed in the first 20% of thickness (the STZ), five 0.04mm thick elements were placed in the adjacent

20%, and five 0.12mm thick elements were placed in the remaining 60%. Radially, the geometry was divided into 69 elements. Sixty 0.1mm wide elements were placed within the central 6mm radius where large gradients were expected to occur and taper off. Outside of this area, minimal changes were anticipated; thus, wider elements were used to reduce computational requirements: four 0.25mm wide elements were placed between 6mm and 7mm of radius, and the remainder was divided into five 1mm wide elements. In total, the structure was divided into 1035 quadratic quadrilateral elements (3274 nodes) using 8-node biquadratic displacement, bilinear pore pressure, reduced integration pore fluid/stress elements (CAX8RP) for all cartilage regions (Figure 2.2-1).

2.2.2. Concave Cartilage Layers - Geometry and Meshing

A 2D axisymmetric structure, 1.5 mm thick with 26.5mm radius of curvature through a 30º arc, was developed to represent the radial cross-section for all of the concave articular cartilage layers (Figure 2.2-2). The top 20% (0.3mm) of the 1.5mm layer thickness represented the STZ, while the remaining 80% (1.2mm) defined the MD/DP zones. Similar to the flat models, a partition was placed at a 3mm arc on the surface to facilitate simulation of a repair cartilage plug in the specific repair models. Other partition lines were added to facilitate desired variations in the finite element mesh. Unlike the flat models, where bone could be simulated by fixing the bottom edge of the model, the curved models required creation of a rigid bone region. This was specifically a requirement of the top convex normal cartilage layer that required application of a load directly to the bone (described later in Section 2.3.2), but was uniformly applied to the bottom curved layer.

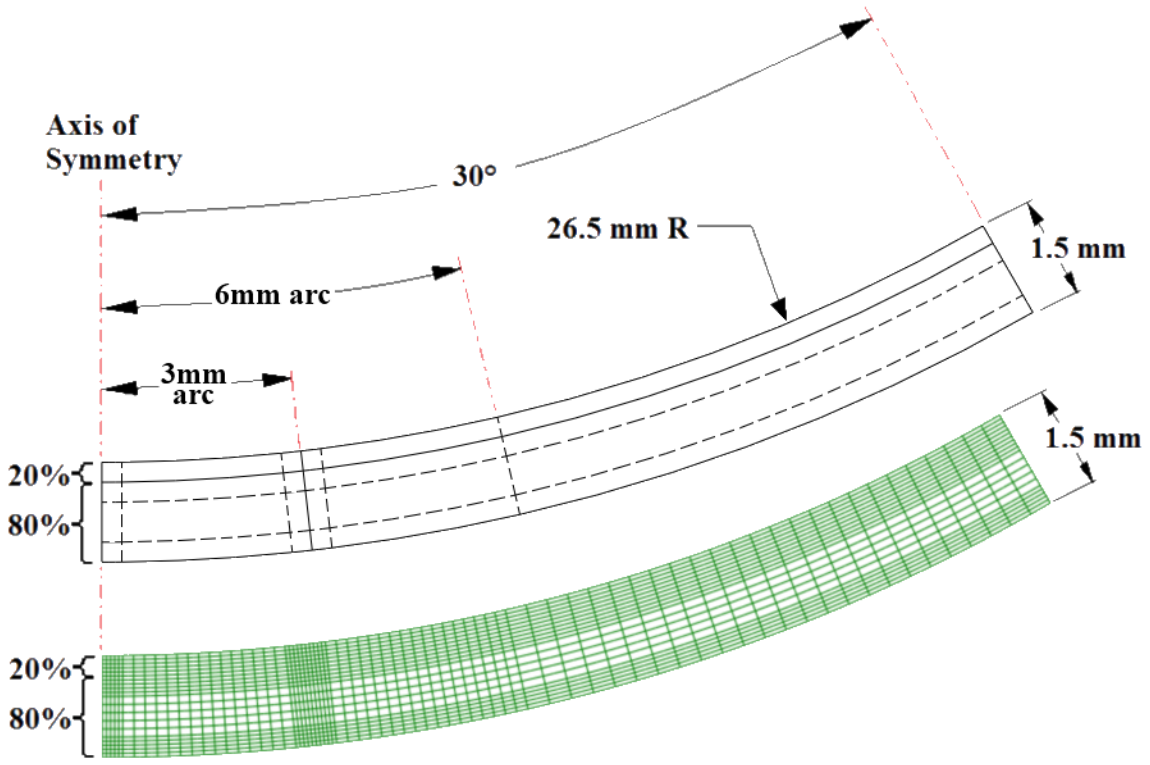

Figure 2.2-2: Finite element model dimensions and applied mesh for concave cartilage layers (rigid bone layer not shown). Partition lines are shown in the top image where solid lines represent those which facilitate material property assignments, and dashed lines facilitate mesh variations.

The cartilage thickness was divided into 20 elements; five 0.06mm thick elements were placed in the first 20% of thickness (the STZ), five 0.06mm thick elements were placed in the adjacent 20%, five 0.12mm thick elements were placed in the next 40%, and five 0.06mm thick elements were placed in the deepest 20%. Radially, following the layer's curvature, the geometry was divided into 72 elements. Five 0.06mm wide elements were placed adjacent to the centerline and to either side of the partition for the repair/normal tissue interface, 15 evenly sized elements (0.16mm wide) filled the space between these locations and 17 extended beyond this central region up to a 6mm arc on the articular surface. Twenty five evenly sized elements (0.32mm wide) extended beyond to fill the remaining tissue, where minimal changes were anticipated. In total, the concave cartilage layer was divided into 1440 quadratic quadrilateral

elements (4505 nodes) using 8-node biquadratic displacement, bilinear pore pressure, reduced integration pore fluid/stress elements (CAX8RP) for all cartilage regions.

Since the bone region was completely rigid, varying its thickness and number of elements were immaterial to the outcome of the analyses. Thus for convenience, a 0.3mm thick rigid region was added to the underside of the cartilage layer with five elements (0.06mm thick) spaced through the bone's thickness exactly matching the number, size, and spacing of elements along the curvature of the cartilage immediately adjacent to the bone. Thus, the bone region was divided into 360 quadratic quadrilateral elements (1235 nodes) using 8-node biquadratic, reduced integration stress elements (CAX8R).

2.3. GEOMETRY OF LOADING SURFACES

2.3.1. Contact Loading of Flat Cartilage Layers

Flat cartilage layers were loaded by contact from relatively rigid impermeable and permeable surfaces each modeled as 2D axi-symmetric convex disks 6mm in radius with a thickness decreasing from 1.92 mm at the center to 1mm at the outermost edge as defined by a 20mm radius profile of the loading surface (Figure 2.3-1). This small radius approximates that found in human joints, such as the humeral head [118], and is similar to that employed by other models [104,105]. When acting on a flat surface, its effective radius of curvature (20mm) falls within the 20-100mm range seen in joints such as the knee [119]. These loading disks were divided into 14 evenly spaced elements throughout the thickness and 61 elements throughout the radius yielding a total of 854 quadratic quadrilateral elements (2713 nodes). This resulted in element sizes within the disk which were comparable to the width of elements in the cartilage surface. As with the cartilage layer, these were 8-node biquadratic displacement, bilinear pore pressure, reduced integration pore fluid/stress elements (CAX8RP).

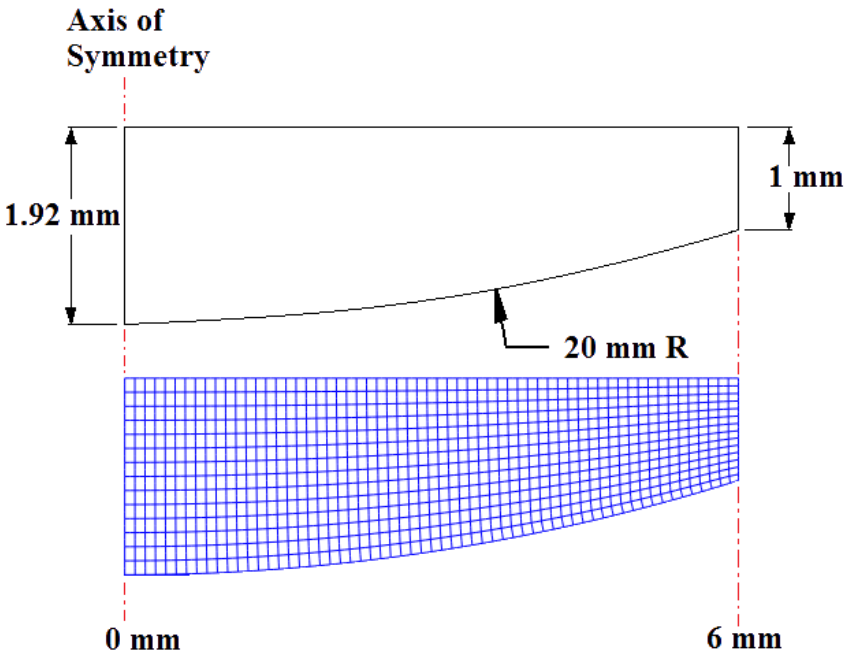

Figure 2.3-1: Finite element model dimensions and applied mesh for the relatively rigid convex impermeable and permeable disks used to load models of flat cartilage layers.

2.3.2. Contact Loading of Concave Cartilage Layers by Convex Surfaces

A 2D axisymmetric structure, 1.5 mm thick with 20.5mm radius of curvature through a 38.8º arc, was developed to represent the radial cross-section for all of the convex articular cartilage layers (Figure 2.3-2). Contact with the previously described 26.5mm concave surface was representative of a diarthrodial joint such as the hip [120]. It's effective radius of curvature (90.5mm) falls within the 20-100mm range seen in joints such as the knee though to the upper end of the range [119]. As with the concave layers, the top 20% (0.3mm) of the convex 1.5mm thick layer represented the STZ, while the remaining 80% (1.2mm) defined the MD/DP zones. Partitions and elements mirrored that of the concave layers. Thus, the convex layer was divided like the concave cartilage layer into 1440 quadratic quadrilateral elements (4505 nodes) using 8-node biquadratic displacement, bilinear pore pressure, reduced integration pore fluid/stress elements (CAX8RP) for all cartilage regions. A 0.3mm thick rigid region also was added to the

convex layer to represent underlying impermeable bone. When the convex layer was used to model rigid impermeable or permeable loading surfaces, the entire layer was modeled using the 8-node biquadratic, reduced integration stress elements (CAX8R).

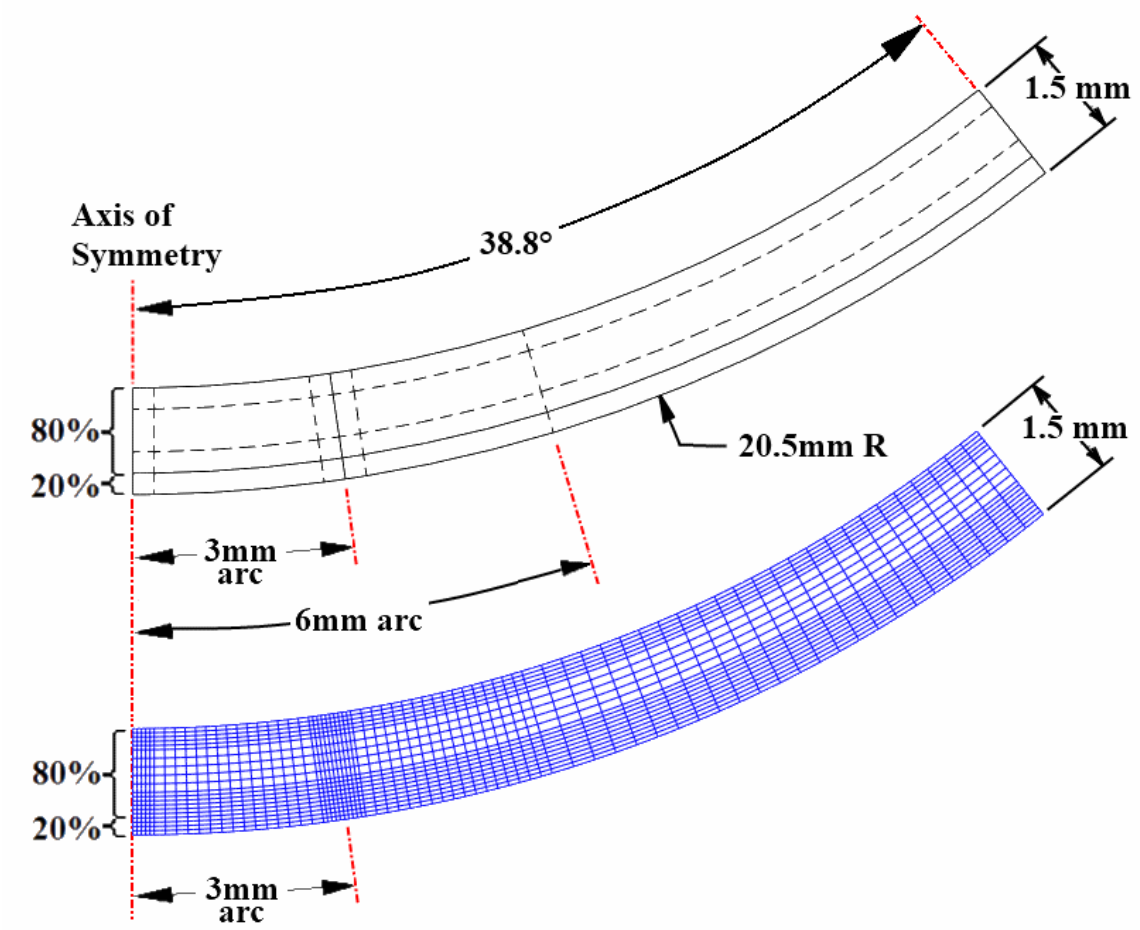

Figure 2.3-2: Finite element model dimensions and applied mesh for the cartilage and rigid impermeable or permeable convex layers used to load concave cartilage surfaces.

2.4. MATERIAL PROPERTIES

2.4.1. Transverse Isotropy – Flat Models

As mentioned in chapter 1, simplifying assumptions are always required to some degree in computational models. For earlier flat models, the solid matrix of cartilage was modeled as linearly elastic and either as isotropic (i.e. the same in all directions) or transversely isotropic

(i.e. the same in all directions within a plane while different in a direction perpendicular to that transverse plane). Using the previously described flat cartilage layer structure, three basic model types were created by strategically assigning these material properties within the regions as described below (Figure Figure 2.4-1):

NORM-TI

Normal articular cartilage was modeled by normal isotropic cartilage in the middle and deep zones and normal transversely isotropic cartilage in the STZ. In the STZ, the plane of isotropy was parallel to the articular surface with the higher modulus in the radial direction.

REP-TI

A repaired full thickness defect was modeled by assigning isotropic properties reflective of homogeneous inferior repair cartilage tissue to the entire defect. Outside of this repair area, normal cartilage was modeled as in NORM-TI, with normal isotropic properties in the middle and deep zones and normal transversely isotropic cartilage in the STZ.

REPwSTZ-TI

A repaired full thickness defect was modeled similar to REP-TI with the exception that the homogeneous repair tissue was only assigned to the middle and deep zones of the defect. The STZ above this repair tissue was assigned normal transversely isotropic properties to simulate covering the repair with a normal STZ. The STZ covering was assumed integrated to surrounding normal tissues and the underlying repair.

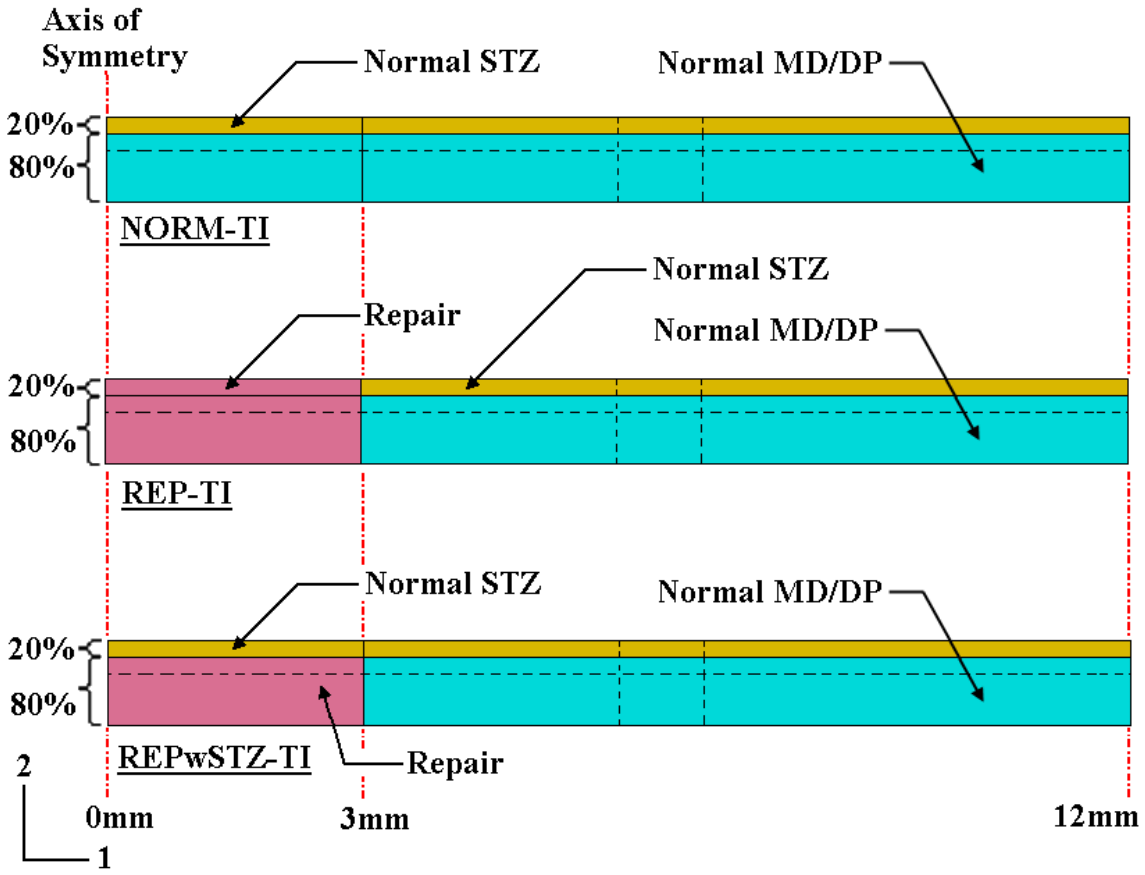

Figure 2.4-1: Schematic diagrams of the flat finite element models analyzed showing assignment of material behavior to various regions within NORM-TI, REP-TI, and REPwSTZ-TI. Transversely isotropic properties were assigned to the normal STZ.

The only parameters required to sufficiently define linearly elastic isotropic materials, as specified in the repair and MD/DP tissues of the above models, are Young's modulus (E) and Poisson's ratio (v). For the linearly elastic transversely isotropic material, as defined in the STZ, two Young's moduli must be specified: one for the plane of isotropy (i.e. parallel to the articular surface), and one for the transverse direction (Appendix A). To that end, material properties comparable to those found in the literature [82] were assigned to the regions as dictated by the TI models (Figure 2.4-1, Table 2.4-1).

Table 2.4-1: Material properties for the respective regions in each of the TI models, with values comparable to the literature (Cohen et al, 1993). 1 ≡ radial, 2 ≡ axial, 3 ≡ circumferential directions; *p* ≡ plane of isotropy, *t* ≡ transverse plane.

Material Property	Normal MD/DP Isotropic	Repair Isotropic
$E_1 = E_2 = E_3$ (MPa)	0.46	0.1
$\nu_{13} = \nu_{31} = \nu_{21} = \nu_{23} = \nu_{12} = \nu_{32}$	0	0
$G_{12} = G_{23} = G_{13}$ (MPa)	0.23	0.05

Material Property	Normal STZ Transversely Isotropic
$E_p = E_1 = E_3$ (MPa)	5.8
$E_t = E_2$ (MPa)	0.46
$\nu_p = \nu_{13} = \nu_{31}$; $\nu_{tp} = \nu_{21} = \nu_{23}$; $\nu_{pt} = \nu_{12} = \nu_{32}$	0
$G_p = G_{13}$ (MPa)	2.9
$G_t = G_{12} = G_{23}$ (MPa)	0.37

2.4.2. Tension-Compression Nonlinearity – Flat and Curved Models

Tension-compression nonlinearity has been observed in cartilage due to collagen structure anisotropy [88] and occurs throughout the thickness of articular cartilage, though to a lesser degree outside of the superficial zone [24,91]. As an improvement over the TI models, both normal STZ and MD/DP tissues were modeled as bilinearly elastic to simulate this tension-compression nonlinearity. For this approach tissues were still modeled as linearly elastic but with different stiffnesses when in tension versus compression. Thus, the higher tensile stiffness of the STZ could be modeled for flat and curved models and the lower degree of tension-

compression nonlinearity observed in the MD/DP tissue of normal cartilage could be added. Comparable to the TI models, three basic models were created with tension-compression nonlinearity as described below for both flat (Figure 2.4-2) and curved models (Figure 2.4-3):

NORM-TC

The STZ and MD/DP zones were defined with bilinearly elastic material properties reflective of that normally found in cartilage for those regions.

REP-TC

Inferior repair isotropic cartilage was modeled throughout the thickness in a central region (3mm arc on the surface). Outside of this repair area, normal cartilage was modeled as in NORM-TC, with normal properties defined as bilinearly elastic in the STZ and MD/DP zones.

REPwSTZ-TC

The entire STZ was modeled with normal bilinearly elastic properties to simulate covering the underlying deficient repair with a normal STZ. Repair isotropic cartilage was modeled under the STZ in a central region equivalent in width to REP-TC. The normal MD/DP tissue surrounding the repair region was defined as bilinearly elastic. The STZ covering was assumed integrated to surrounding normal tissues and the underlying repair.

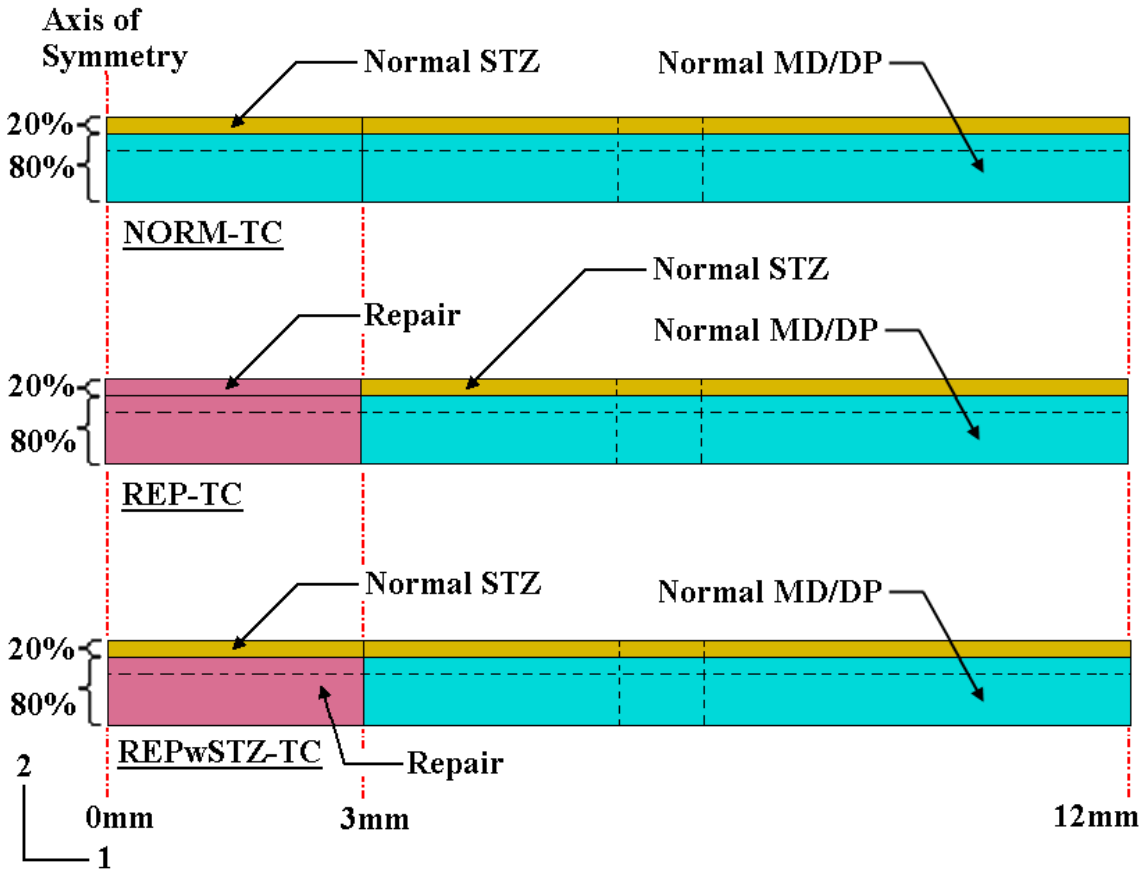

Figure 2.4-2: Schematic diagrams of the flat finite element models analyzed showing assignment of material behavior to various regions within NORM-TC, REP-TC, and REPwSTZ-TC. Normal bilinearly elastic properties were assigned to the normal STZ and MD/DP zones.

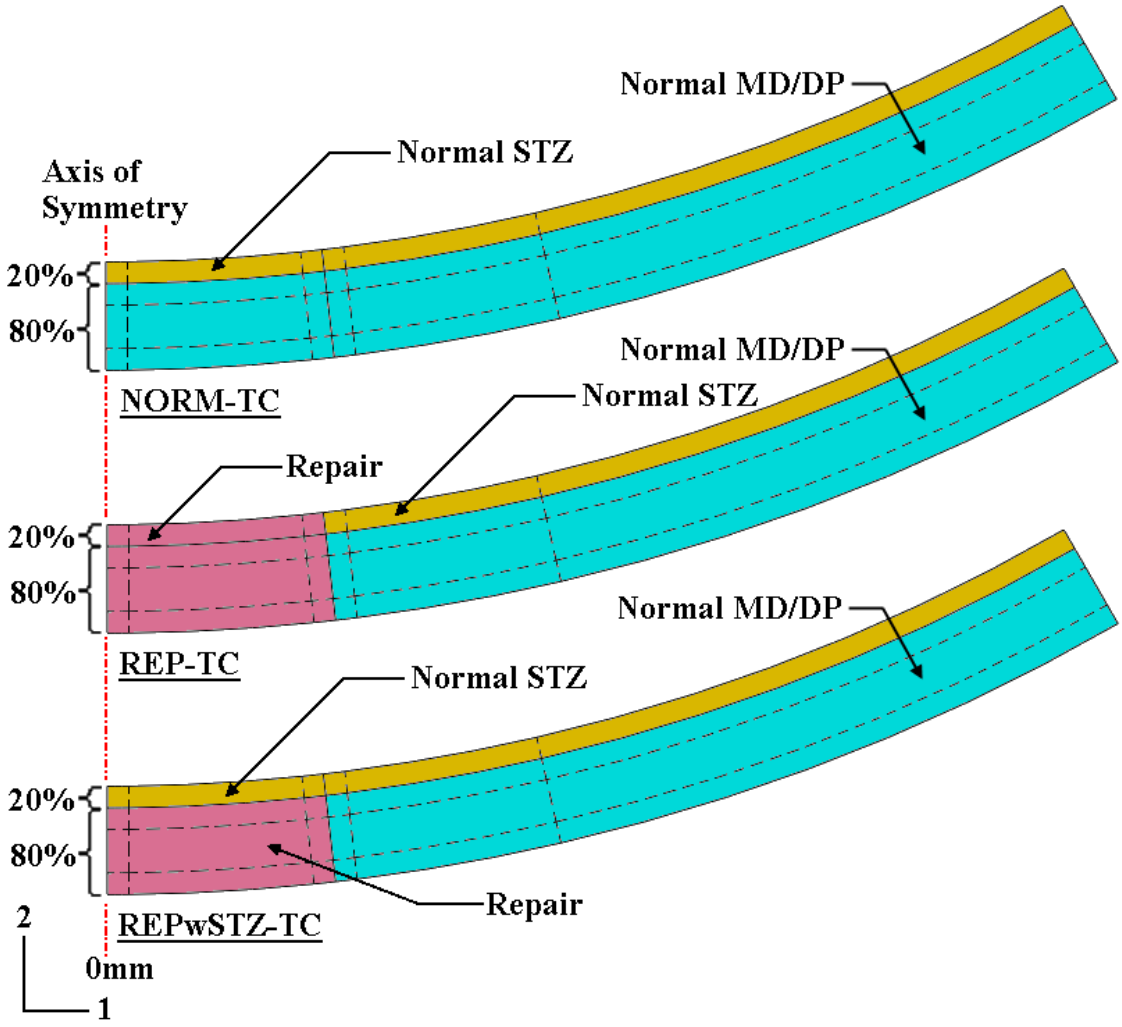

Figure 2.4-3: Schematic diagrams of the concave finite element models analyzed showing assignment of material behavior to various regions within NORM-TC, REP-TC, and REPwSTZ-TC. Normal bilinearly elastic properties were assigned to the normal STZ and MD/DP zones.

Similar to transverse isotropy, two Young's moduli must be specified to define tension/compression nonlinearity: one to define tensile stiffness, and one for compressive stiffness. Material properties comparable to those observed experimentally and modeled by others [24,82,88,91] were assigned to the regions as indicated by the models (Figure 2.4-2, Figure 2.4-3, and Table 2.4-2).

Table 2.4-2: Material properties for the respective regions in each of the TC models, with values comparable to the literature [24,82]. 1 ≡ radial, 2 ≡ axial, 3 ≡ circumferential directions.

Material Property	Normal STZ Bilinearly Elastic	Normal MD/DP Bilinearly Elastic	Repair Isotropic
Tension: $E_1 = E_2 = E_3$ (MPa)	5.8	2.0	0.1
Compression: $E_1 = E_2 = E_3$ (MPa)	0.46	0.2	0.1
$\nu_{13} = \nu_{31} = \nu_{21} = \nu_{23} = \nu_{12} = \nu_{32}$	0	0	0
$G_{12} = G_{23} = G_{13}$ (MPa)	0.23	0.1	0.05

2.4.3. Material Properties – Strain Dependent Permeability

For all of the above models, strain-dependent permeability was prescribed for the normal STZ only, using the exponential relationship $k = k_0 exp^{M\varepsilon}$, where $k_0 \equiv$ initial permeability, $M \equiv$ a material-specific constant, and $\varepsilon \equiv$ volumetric strain [20,22]. Volumetric strain (ε) was defined in terms of void ratio (e) as $\varepsilon = (e - e_0)/(1 + e_0)$, where $e_0 \equiv$ initial void ratio. Four levels of M were chosen ($M = 0$, 1, 5, and 10) to investigate a range of low to high levels around values normally found in articular cartilage [23,24,121] (Table 2.4-3). These four levels of strain-dependent permeability were investigated in the TI models. Once the effect of varying strain dependent permeability was established, only a mid-range value of M = 5 was used in the TC models to approximate that normally found in cartilage. Paired values of void ratio and the corresponding permeability, adjusted to units of mm/s (k_0'), were entered into Abaqus/CAE in tabular form as required by Abaqus, where $k_0' = k_0\gamma$ and $\gamma \equiv$ the specific gravity of the fluid in units of N/mm^3. The table was defined for void ratios from 0.5 to 4.0 in increments of 0.5, a level chosen to minimize the effect of linear interpolation between defined values.

Table 2.4-3: Permeability properties for the respective regions in each of the models, with values comparable to the literature [23,24,121].

Permeability Property	Normal MD/DP	Normal STZ	Repair Tissue
k_0 (x 10^{-3}mm^4/N-s)	5.1	5.1	10
M	0	0, 1, 5, and 10	0
e_0	4	4	4
γ (N/mm^3)	9.761 x 10^{-6}	9.761 x 10^{-6}	9.761 x 10^{-6}

2.5. LOAD AND BOUNDARY CONDITIONS

2.5.1. Flat Models – Parabolic Pressure Loading

Early TI models were loaded without contact by a constant pressure distribution which was instantaneously applied directly to the articular surfaces via a user-defined FORTRAN subroutine that prescribed a parabolic pressure profile which decreased from a maximum of 0.1MPa at the center to 0MPa at a 4.5mm radius (Figure 2.5-1). The applied pressure was maintained for 30sec at which point comparisons were made among the three models. Throughout loading, zero pore fluid pressure was maintained on the articular and outer radial surfaces to ensure unrestricted fluid flow. The base of each model was fixed to simulate attachment to subchondral bone.

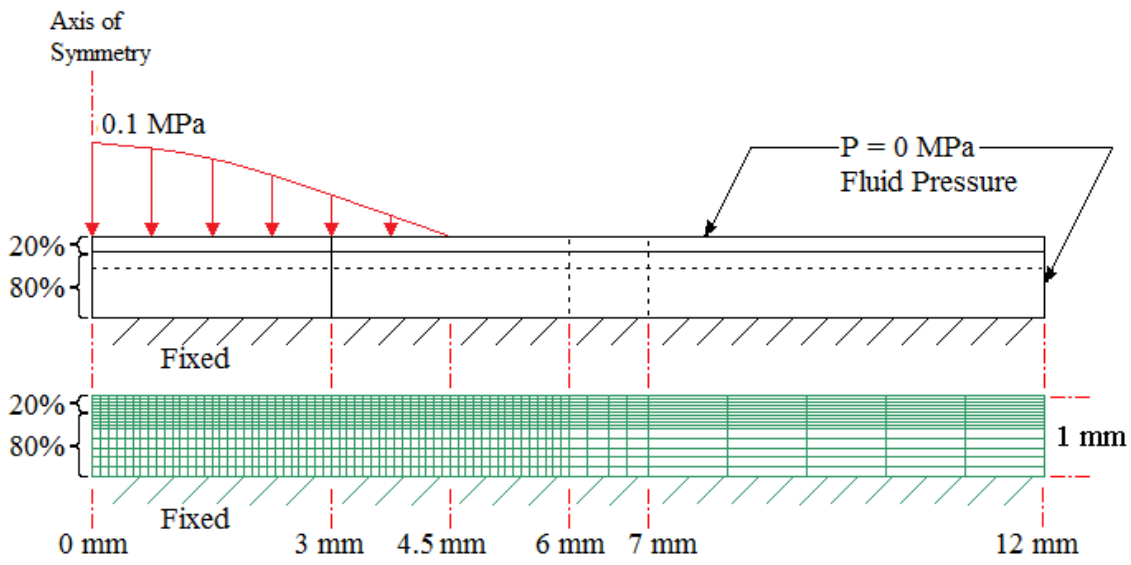

Figure 2.5-1: Finite element model dimensions and applied mesh showing parabolic pressure load profile and boundary conditions for flat TI models.

2.5.2. Flat Models – Contact Loading

Later TI and flat TC models were loaded by the relatively rigid impermeable and permeable 20mm radius disks previously described (section 2.3.1). A 1N downward load was effectively applied by subjecting the top surface of the loading disk to a uniform pressure (0.008842 MPa over a 6mm radius) in ramp fashion over 0.5 sec and was then held constant for 30 sec to evaluate short-term creep (Figure 2.5-2). Displacement of the disk was only allowed in the axial direction such that the applied load was transferred from the disk to the center of the articular surface via the area of contact resulting between the surfaces. Initially, zero pore fluid pressure was defined on the entire articular surface and the outer radial surfaces of the cartilage layer to ensure unrestricted fluid flow out of the layer. Throughout loading by the impermeable sphere, this free-draining condition was maintained except within the region of contact where flow from the surface was shut off. For loading by the permeable sphere, the free-draining condition was maintained for the entire surface at all times. A user-defined FORTRAN

subroutine was used to regulate axial fluid flow from the articular surface for both loading scenarios. The bottom edge of each model was fixed to simulate attachment to subchondral bone. Nonlinear geometry was incorporated in TC models to accommodate finite deformation. Six combinations thus existed for both TI and TC flat models for three bottom layers (NORM-TC, REP-TC, and REPwSTZ-TC) loaded by top layers (IMP and PER). (Figure 2.5-3).

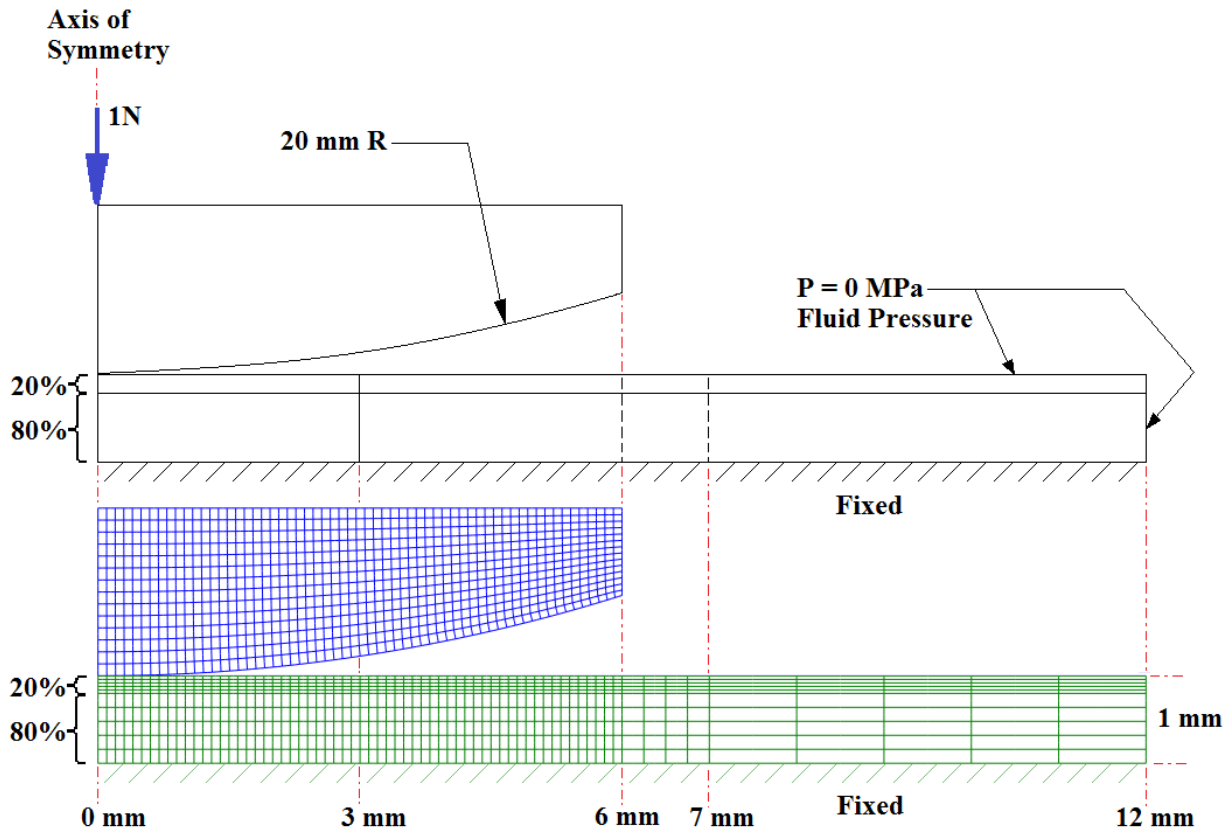

Figure 2.5-2: Finite element model dimensions and applied mesh for a flat cartilage layer (TI or TC) loaded by a relatively rigid convex shaped disk showing applied load.

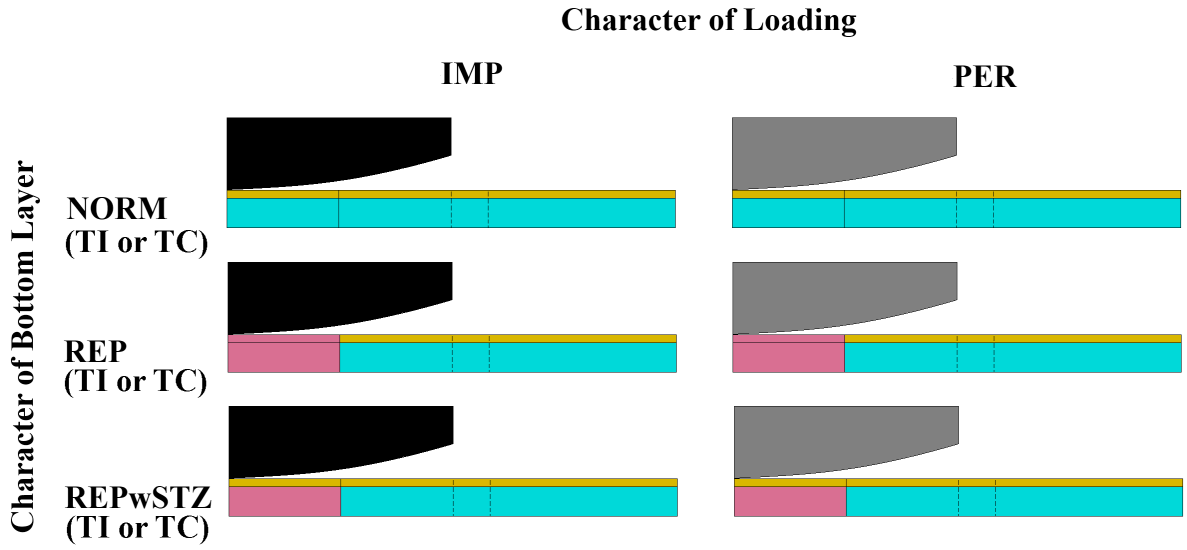

Figure 2.5-3: Two convex surfaces (IMP and PER) loading three flat surfaces with TI or TC properties (NORM-TI or -TC, REP-TI or -TC, and REPwSTZ-TI or -TC) resulting in six models.

2.5.3. Curved Models – Contact Loading

Concave TC models were loaded by the rigid impermeable, rigid permeable, and normal 20.5mm radius convex layers previously described (section 2.3.2). A 5N concentrated load was directly applied to the top center of each convex layer via a rigid bone region and was transferred to the bottom concave layer through the contact area between the center regions of the top convex surface and the underlying concave cartilage layer (Figure 2.5-4). The load was applied in ramp fashion over 0.5s and then held constant for a simulated 48-h period to ensure that equilibrium was achieved. Short-term creep was evaluated at 30 s. Long-term creep was evaluated at equilibrium (defined as within 0.1% of the value at 48 h). Displacement of the convex loading layer was only allowed in the axial direction. Initially, zero pore fluid pressure was defined on the entire articular surface and the outer radial surfaces of the cartilage layer to ensure unrestricted fluid flow out of the layer. Throughout loading by the impermeable sphere, this free-draining condition was maintained except within the region of contact where flow from

the surface was shut off. For loading by the permeable sphere, the free-draining condition was maintained for the entire surface at all times. For loading by a normal cartilage layer, this free-draining condition was maintained on both the convex loading and concave loaded surfaces except within the region of contact where fluid flow occurred between NORM-TC-TOP and the loaded surfaces in a manner that maintained continuity of pore fluid pressure at the surfaces. A user-defined FORTRAN subroutine was used to regulate axial fluid flow from the articular surface for each loading scenarios. Nonlinear geometry was incorporated to accommodate finite deformation. Nine combinations were thus modeled for three bottom layers (NORM-TC, REP-TC, and REPwSTZ-TC) loaded by three top layers (IMP, NORM-TC-TOP, and PER) (Figure 2.5-3).

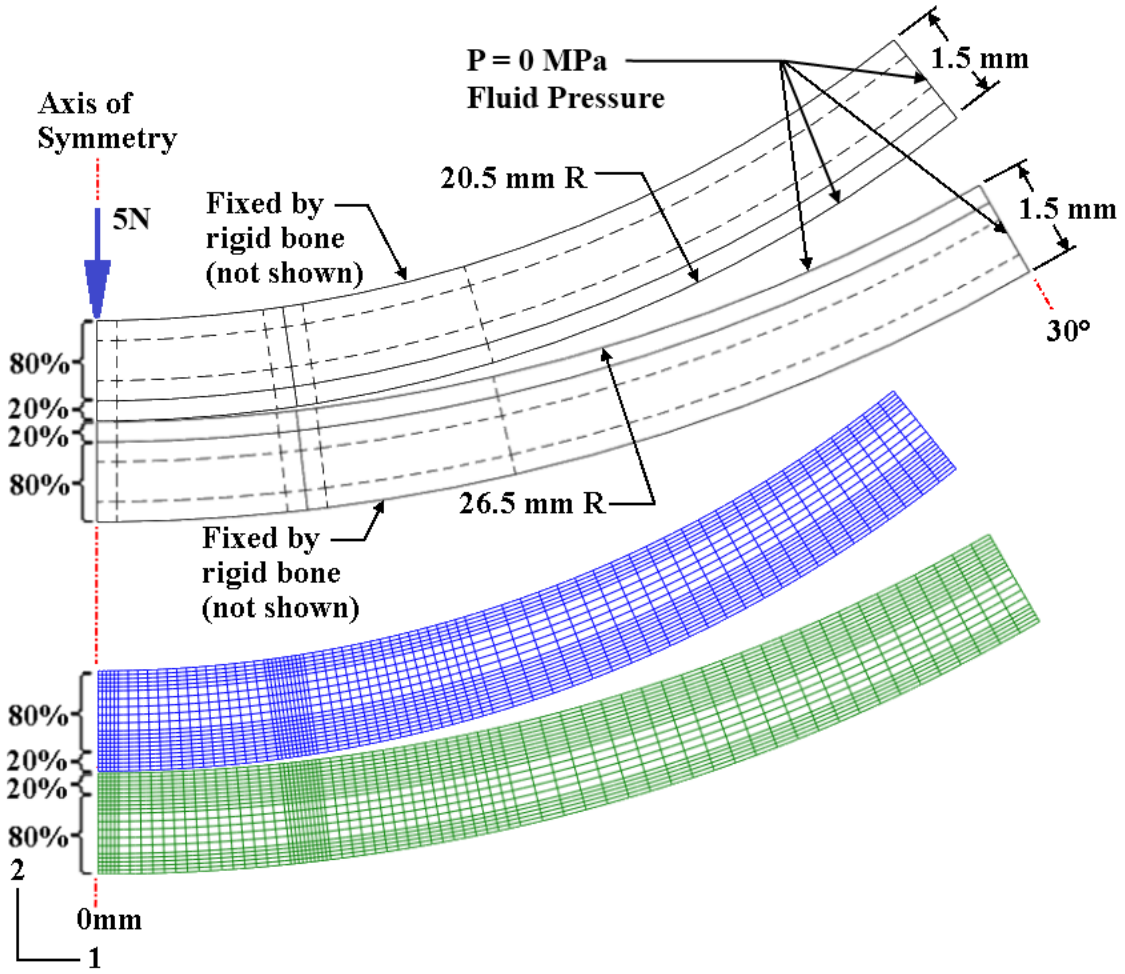

Figure 2.5-4: Finite element model dimensions and applied mesh for a concave cartilage layer loaded by a convex layer. Rigid bone layers only provide rigid fixation of the boundaries to which they are attached and are not shown here.

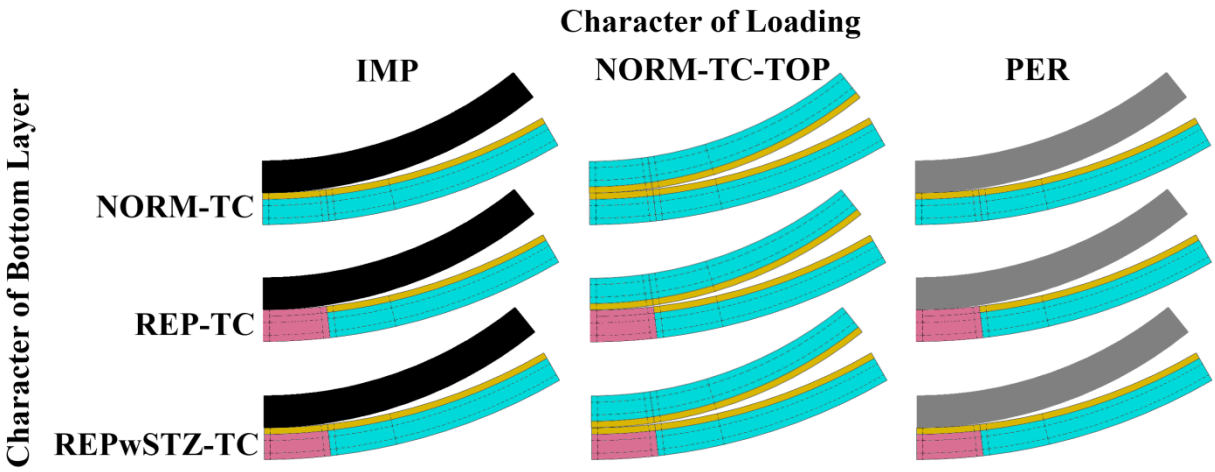

Figure 2.5-5: Three convex surfaces (IMP, NORM-TC-TOP, and PER) loading three concave surfaces (NORM-TC, REP-TC, and REPwSTZ-TC) resulting in nine models.

2.6. SUMMARY

Models have been described which were used to investigate the response of three cartilage layer types (i.e. normal, repaired without an STZ, and repaired with a normal STZ covering) to various loading conditions. Transverse isotropy was used in the STZ of early flat models loaded by parabolic pressure distributions [122] or by contact loading of relatively rigid impermeable and permeable convex disks [123]. For these models, a range of strain-dependent permeability values in the STZ were investigated. Later models replaced transverse isotropy in the STZ with tension-compression nonlinearity and included it in the middle and deep zones. One value of strain-dependency, reflective of normal cartilage, was implemented in the STZ for these later models. Nonlinear geometry was included to account for finite deformation. With these features, flat cartilage layers were modeled for contact loading by relatively rigid impermeable and permeable disks [124]. Concave cartilage layers were modeled for contact loading by rigid impermeable and permeable convex layers, and by a normal cartilage layer [125].

The following chapters will present results from these analyses while comparing and contrasting the outcomes of the different models.

3. STRAIN DEPENDENT PERMEABILITY - PRESSURE LOADING

3.1. OVERVIEW

Model results reported in this section represent the initial effort to examine the influence that higher tensile stiffness and strain dependent permeability in the STZ can have on the behavior of normal and repaired articular surfaces, and has been published [122]. In the STZ only, directional stiffness was modeled via transverse isotropy and a range of strain-dependent permeability values were investigated (Figure 2.4-1). All other tissues, normal and repaired, were modeled as isotropic linearly elastic materials having constant permeability. Model surfaces were loaded by a nonlinear pressure distribution applied over a constant area and held constant over time (Figure 2.5-1). Finite deformation was not accounted for in these models.

3.2. RESULTS

3.2.1. Full Thickness Axial Compression

The full thickness repair in REP-TI, without an STZ, had an overall axial compression of all zones of the cartilage layer at center of 23.8% (Figure 3.2-1). This compression was unaffected by changing M in the surrounding normal STZ and was 3.3 to 4.9 times greater than that of NORM-TI, for increasing values of M (Table 3.2-1). Axial compression of the articular surface at the center of REPwSTZ-TI was 55% to 68% less than REP-TI, as M increased in the STZ. While the behavior of REPwSTZ-TI was still 48% to 56% greater than NORM-TI, as M increased, this was markedly reduced from the fourfold increase of REP-TI compared to NORM-TI.

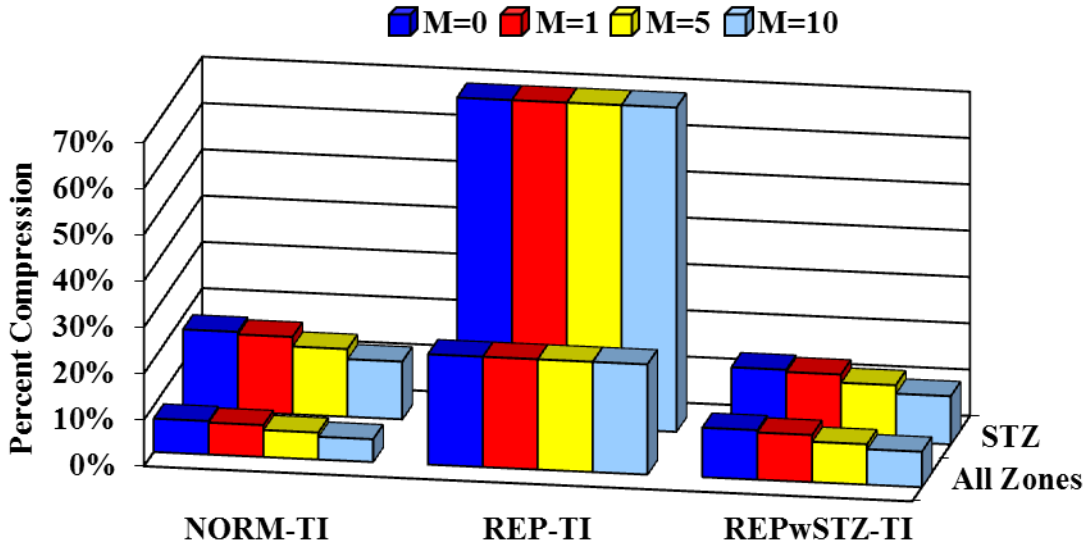

Figure 3.2-1: Percent compression of the entire cartilage layer (All Zones) and of the STZ only for increasing levels of strain-dependent permeability in the normal STZ at center of the models after 30 sec of loading.

Table 3.2-1: Relative changes in compression of the entire cartilage layer and of the STZ only after 30 sec of loading between the three models investigated (NORM-TI, REP-TI, and REPwSTZ-TI) at each level of strain-dependent permeability modeled in the normal STZ.

	Full thickness compression at center		
RATIOS →	REP-TI / NORM-TI	REPwSTZ-TI / REP-TI	REPwSTZ-TI / NORM-TI
M=0	3.31	0.45	1.48
M=1	3.46	0.43	1.48
M=5	4.10	0.37	1.50
M=10	4.85	0.32	1.56

	STZ compression at center		
RATIOS →	REP-TI / NORM-TI	REPwSTZ-TI / REP-TI	REPwSTZ-TI / NORM-TI
M=0	4.07	0.21	0.84
M=1	4.20	0.20	0.84
M=5	4.80	0.17	0.84
M=10	5.64	0.15	0.84

3.2.2. STZ Compression

Compression of the uppermost 20% region, that corresponding to the location of the STZ, was compared among the models. This uppermost region of REP-TI, filled by a full thickness isotropic repair, was compressed by 70.1% of its original dimension at the center of applied stress, from 0.2 mm undeformed thickness to 0.06 mm (Figure 3.2-1). This compression was unaffected by changing M in surrounding normal STZ and was 4.1 to 5.6 times greater than that of NORM-TI's STZ compression, for increasing values of M (Table 3.2-1). Compression of REPwSTZ-TI's STZ was 16% less than the compression of NORM-TI's STZ for all values of M. This was 79% to 85% less than the same region in REP-TI, for M increasing from 0 to 10.

3.2.3. Strain Beneath the STZ

The central point of REP-TI, which would have been just beneath the STZ had it not been a full thickness isotropic repair, experienced 44% axial strain regardless of changing M in surrounding normal STZ (Figure 3.2-2). This was 3.4 to 6.1 times greater than the axial strain of NORM-TI at the same point, for increasing values of M (Table 3.2-2). While REPwSTZ-TI's axial strain at this point was 2.6 to 2.8 times greater than that of NORM-TI, it was 22 to 56% less than REP-TI, for increasing values of M.

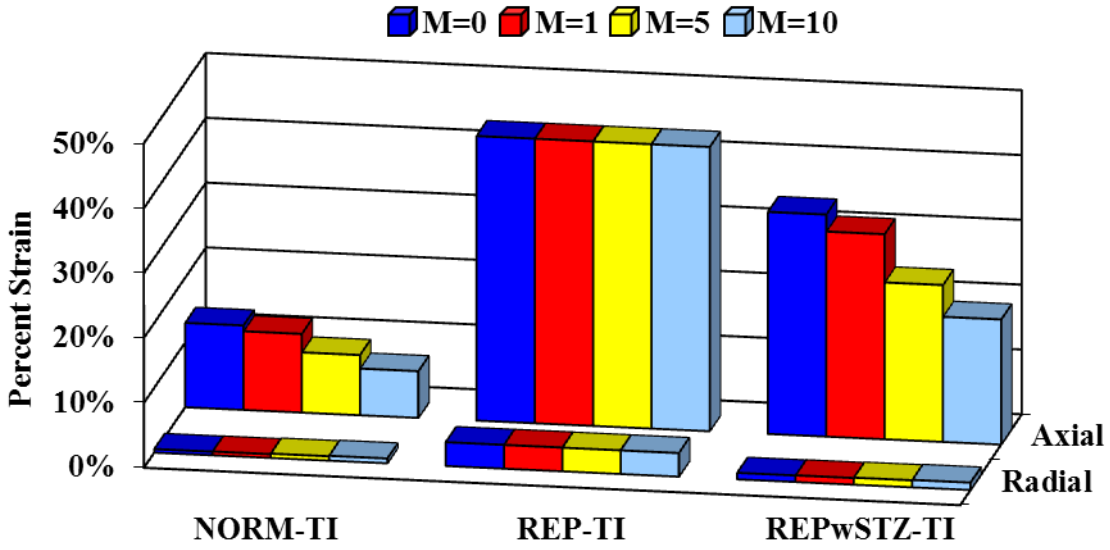

Figure 3.2-2: Percent radial (e11) and axial (e22) strains occurring at the model center just beneath the STZ region after 30 sec of loading for increasing levels of strain-dependent permeability in the normal STZ.

Table 3.2-2: Relative changes in axial (e_{22}) and radial (e_{11}) strain at center immediately beneath the STZ region after 30 sec of loading between the three models investigated (NORM-TI, REP-TI, and REPwSTZ-TI) at each level of strain-dependent permeability modeled in the normal STZ.

	Axial strain under STZ at center		
RATIOS →	REP-TI / NORM-TI	REPwSTZ-TI / REP-TI	REPwSTZ-TI / NORM-TI
M=0	3.37	0.78	2.63
M=1	3.62	0.72	2.61
M=5	4.73	0.55	2.61
M=10	6.09	0.44	2.68

	Radial strain under STZ at center		
RATIOS →	REP-TI / NORM-TI	REPwSTZ-TI / REP-TI	REPwSTZ-TI / NORM-TI
M=0	6.75	0.27	1.84
M=1	6.41	0.28	1.78
M=5	5.51	0.30	1.63
M=10	4.93	0.31	1.55

Radially directed strain at the same point in REP-TI, experienced about 3.6% strain regardless of changing M in surrounding normal STZ (Figure 3.2-2). This was 6.8 to 4.9 times greater than the radial strain of NORM-TI at the same point, for increasing values of M (Table 3.2-2). REPwSTZ-TI's radial strain at this point was 73 to 69% less than REP-TI and 1.8 to 1.6 times greater than NORM-TI, for increasing values of M.

3.2.4. Stress in the Solid Matrix

Contour plots of von Mises stress show higher elastic stresses in the STZ of NORM-TI and REPwSTZ-TI, affording protection for underlying tissue (Figure 3.2-3). Because of the inferior properties in REP-TI, the surface compresses substantially more than in REPwSTZ-TI, while REPwSTZ-TI more closely approximates the stress patterns seen in NORM-TI. Stress in REPwSTZ-TI remains highest in the STZ similar to the behavior in NORM-TI. However, both REP-TI and REPwSTZ-TI developed greater stress gradients at the normal/repair interface than NORM-TI.

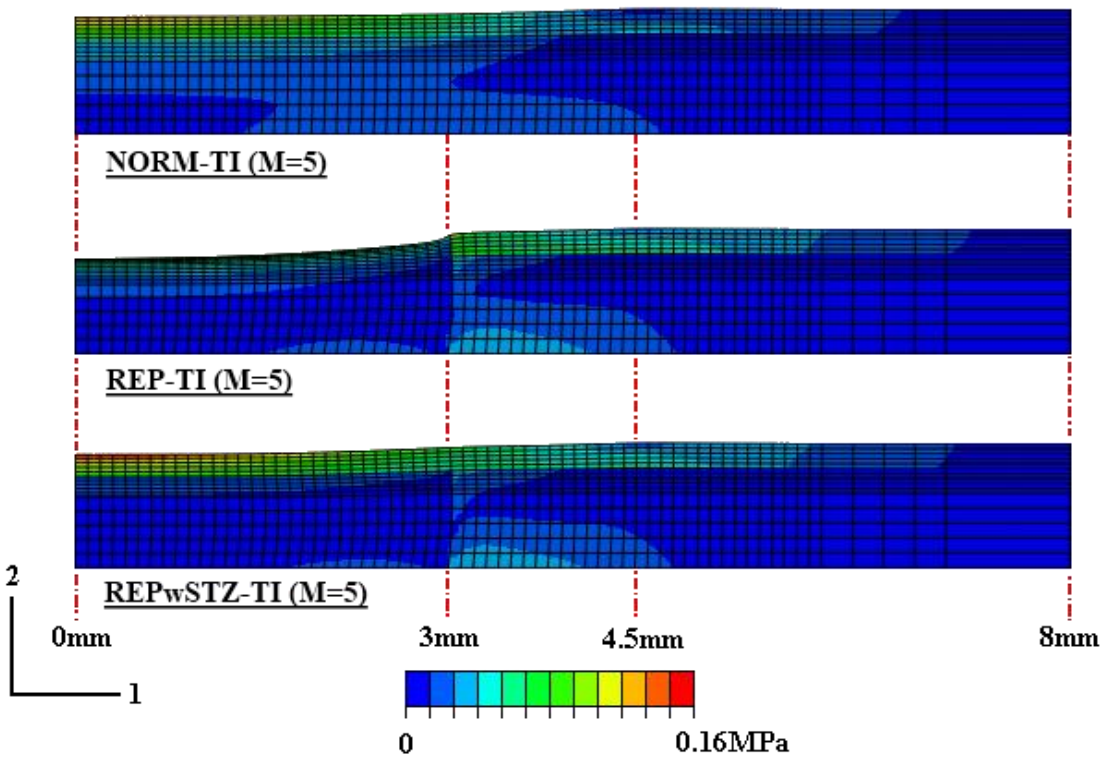

Figure 3.2-3: Von Mises stress distributions superimposed on a deformed mesh for a strain-dependent permeability value of M=5 in NORM-TI, REP-TI, and REPwSTZ-TI models after 30 sec of loading. Only results for the mid-range value of M=5 are shown, but are representative of patterns seen for all values. Regions outside of the 8mm radius did not experience stress changes and are not shown.

Von Mises stress at the center of the articular surface for the full thickness repair in REP-TI was the same for all models, regardless of values for M in the surrounding normal STZ (Figure 3.2-4). For M increasing from 0 to 10, this stress was 17% to 26% less than NORM-TI (Table 3.2-3). Von Mises stress at the center of the articular surface for REPwSTZ-TI was 41% to 52% greater than REP-TI and 17% to 13% greater than NORM-TI, for M increasing from 0 to 10, indicating this zone to be supporting large stresses in protection of underlying repair tissue.

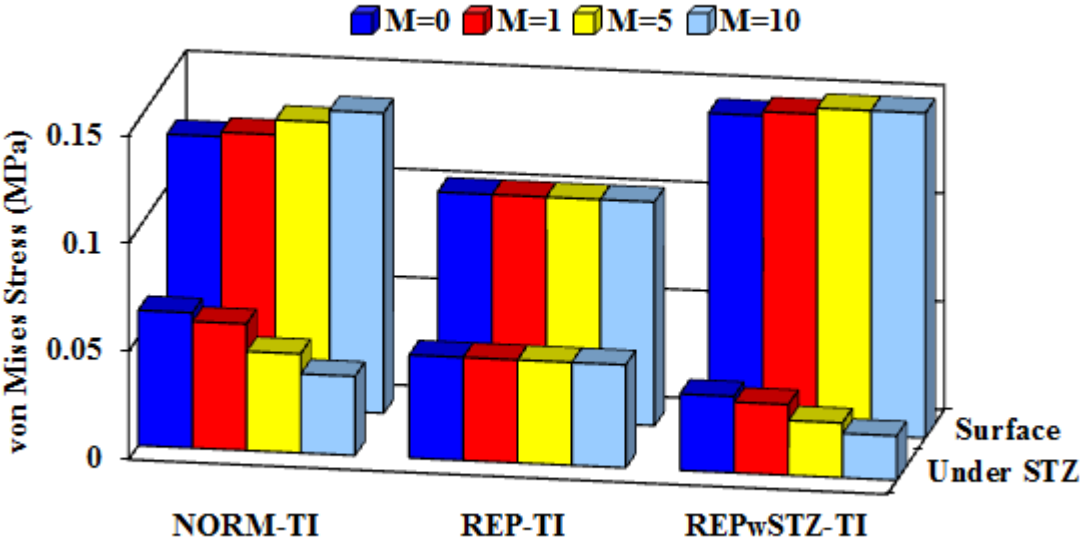

Figure 3.2-4: Von Mises stress at the center of the articular surface and immediately beneath the STZ after 30 sec of loading for increasing levels of strain-dependent permeability in the normal STZ.

Table 3.2-3: Relative changes in von Mises stress at the center of the articular surface and immediately beneath the STZ region after 30 sec of loading between the three models investigated (NORM-TI, REP-TI, and REPwSTZ-TI) at each level of strain-dependent permeability modeled in the normal STZ.

	von Mises stress on surface at center		
RATIOS →	REP-TI / NORM-TI	REPwSTZ-TI / REP-TI	REPwSTZ-TI / NORM-TI
M=0	0.83	1.41	1.17
M=1	0.82	1.43	1.17
M=5	0.78	1.48	1.15
M=10	0.74	1.52	1.13

	von Mises stress under STZ at center		
RATIOS →	REP-TI / NORM-TI	REPwSTZ-TI / REP-TI	REPwSTZ-TI / NORM-TI
M=0	0.76	0.74	0.56
M=1	0.81	0.69	0.56
M=5	1.04	0.53	0.55
M=10	1.30	0.43	0.56

At the central point of REP-TI's repair, just beneath the region which would have been filled by STZ had it not been a full thickness repair, von Mises stress for REP-TI was virtually unaffected by changing values for M in the surrounding normal STZ (Figure 3.2-4). In comparison to NORM-TI's von Mises stress at this point, REP-TI's stress was less than NORM-TI by 24% for M=0 and 19% for M=1, and was greater than NORM-TI by 4% for M=5, and 30% for M=10 (Table 3.2-3). Von Mises stress at this point in the repair region of REPwSTZ-TI was 26% to 57% less than REP-TI. Furthermore, von Mises stress in REPwSTZ-TI, at this point, was consistently less than NORM-TI by 44%.

3.2.5. Fluid Pressure

As a prescribed boundary condition, fluid pressure was zero at the articular surface for all models at all time-points. At the central point of REP-TI's repair, just beneath the region which would have been filled by STZ had it not been a full thickness repair, fluid pressure for REP-TI was virtually unaffected by different values of M in the surrounding normal STZ (Figure 3.2-5). In comparison to NORM-TI's fluid pressure at this point, REP-TI's fluid pressure was greater than NORM-TI by 39% for M=0 and 26% for M=1, and was less than NORM-TI by 3% for M=5, and 16% for M=10 (Table 3.2-4). Fluid pressure at this point in the repair region of REPwSTZ-TI was 19% to 45% greater than REP-TI, for M ranging from 0 to 10, and was 65% to 21% greater than NORM-TI, for M ranging from 0 to 10.

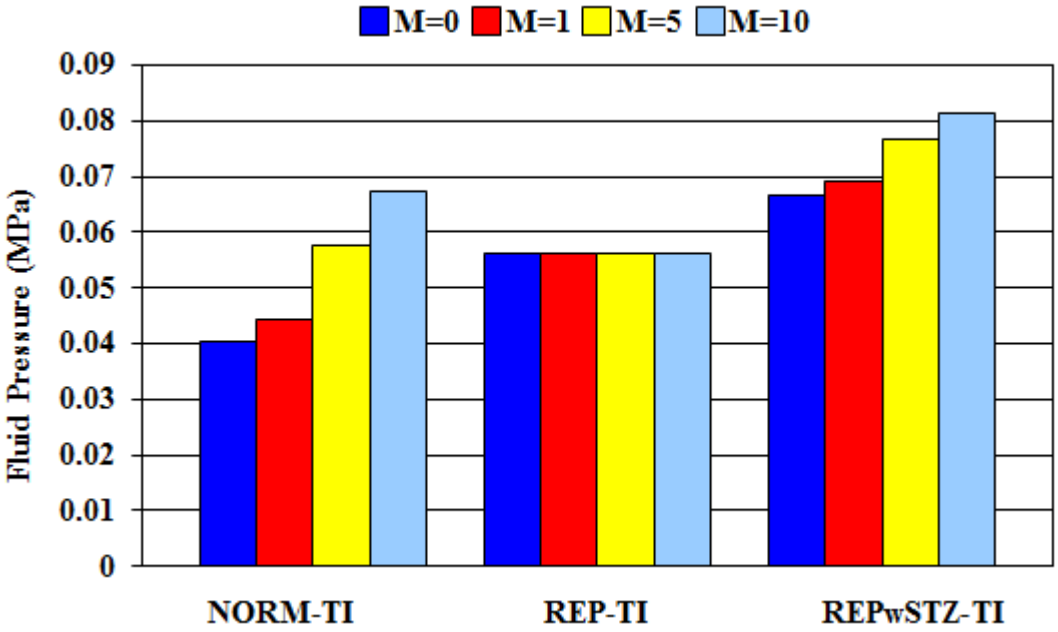

Figure 3.2-5: Fluid pressure at the center of repair tissue immediately beneath the STZ after 30 sec of loading for increasing levels of strain-dependent permeability in the normal STZ.

Table 3.2-4: Relative changes in fluid pressure immediately beneath the STZ region at center after 30 sec of loading between the three models investigated (NORM-TI, REP-TI, and REPwSTZ-TI) at each level of strain-dependent permeability modeled in the normal STZ.

RATIOS →	Fluid pressure under STZ at center		
	REP-TI / NORM-TI	REPwSTZ-TI / REP-TI	REPwSTZ-TI / NORM-TI
M=0	1.39	1.19	1.65
M=1	1.26	1.23	1.56
M=5	0.97	1.36	1.33
M=10	0.84	1.45	1.21

3.2.6. Rate of Fluid Loss

Effective fluid velocity gradient distributions show higher rates of fluid loss for REP-TI without a normal STZ as compared to NORM-TI and REPwSTZ-TI with a normal STZ (Figure 3.3-6). The lack of a protective STZ in REP-TI showed not only the highest rates of fluid loss but with a profile that exhibited a drastic drop at the interface between normal and repair regions. A smooth transition in flow appeared at the same interface in REPwSTZ-TI.

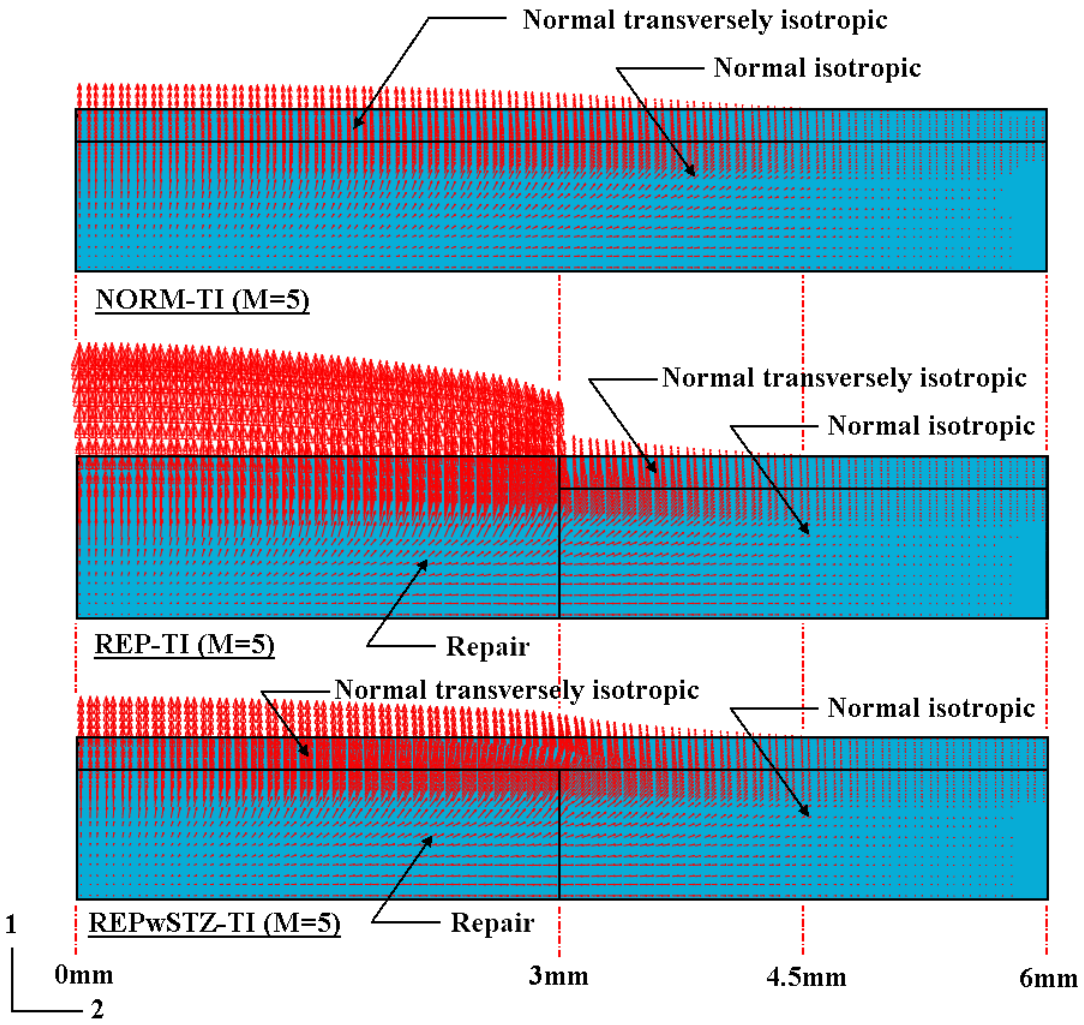

Figure 3.2-6: Effective fluid velocity gradient distributions for a strain-dependent permeability value of M=5 in NORM-TI, REP-TI, and REPwSTZ-TI after 30 sec of loading, superimposed on an undeformed model with areas of different material behavior outlined. Only results for the mid-range value of M=5 are shown, but are representative of patterns seen for all values. Also, only a 6mm radius is shown as very little flow occurred in regions outside of the 4.5mm radius of loading.

The full thickness repair in REP-TI, without STZ, had an effective fluid velocity normal to the center of the articular surface of 3.20 μm/s and was unaffected by changing M in the surrounding normal STZ (Figure 3.2-7). This rate of fluid loss for REP-TI was 2.9 to 7.8 times greater than that of NORM-TI (Table 3.2-5). The rate of fluid loss normal to the articular

surface at the center of REPwSTZ-TI was 45% to 82% less than REP-TI, for M increasing from 0 to 10. REPwSTZ-TI's rate of fluid loss was 59% to 41% greater than NORM-TI, for M increasing from 0 to 10, but was markedly less than the roughly three to eightfold increase of REP-TI compared to NORM-TI.

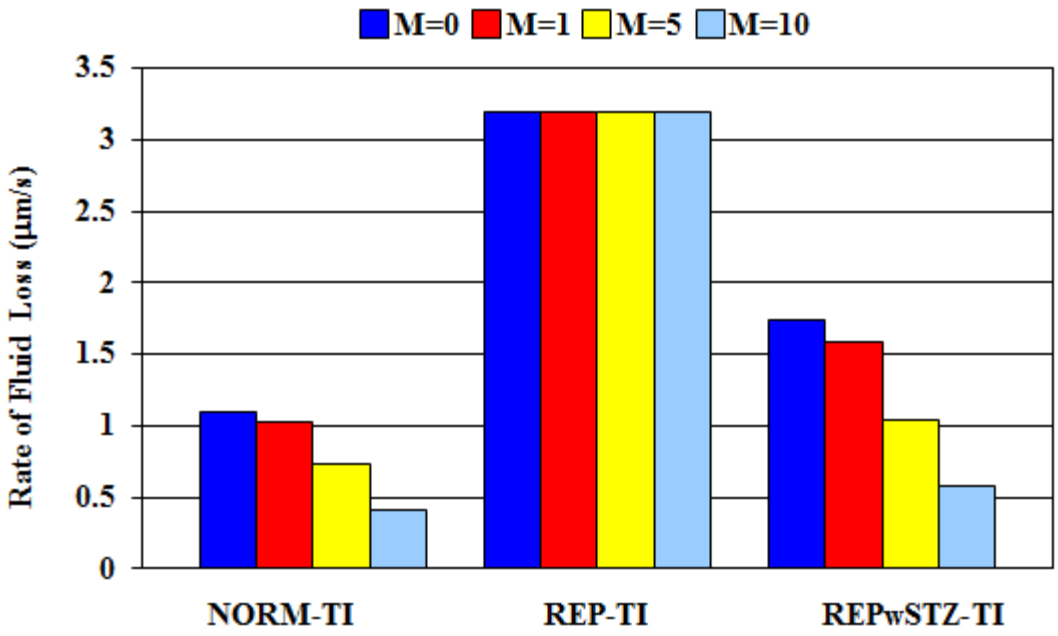

Figure 3.2-7: Rate of fluid loss from the center of the articular surface after 30 sec of loading for increasing levels of strain-dependent permeability in the normal STZ.

Table 3.2-5: Relative changes in effective fluid velocity from the articular surface at center after 30 sec of loading between the three models investigated (NORM-TI, REP-TI, and REPwSTZ-TI) at each level of strain-dependent permeability modeled in the normal STZ.

	Fluid loss rate from surface at center		
RATIOS →	REP-TI / NORM-TI	REPwSTZ-TI / REP-TI	REPwSTZ-TI / NORM-TI
M=0	2.91	0.55	1.59
M=1	3.11	0.49	1.54
M=5	4.37	0.33	1.42
M=10	7.78	0.18	1.41

3.3. SUMMARY

The finite element analyses reported in this chapter represent initial efforts to predict the behavior of articular cartilage layers with a region of repair tissue and the impact that a quality superficial tangential zone has on cartilage behavior. Directional stiffness was modeled in the STZ via transverse isotropy and a range of strain-dependent permeability values were investigated. All other tissues, normal and repaired, were modeled as isotropic linearly elastic materials having constant permeability. Model surfaces were loaded by a nonlinear pressure distribution applied over a constant area and held constant over time. These analyses predict that having a transversely isotropic STZ over a construct would protect it from the severe mechanical stresses/strains that would be present otherwise. Results demonstrate a reduction in the axial compression of the entire cartilage thickness and the STZ under load and a reduction in the rate of fluid loss from the articular surface. Further, it predicts that these reductions would increase as the STZ's permeability becomes more dependent on strain, enabling the repair region to behave more like a normal articular surface. The lower rate of fluid loss resulted in higher fluid pressure for the repair tissue under the normal STZ covering as compared to the repair without STZ. Paired with the higher fluid pressure was a reduction in von Mises stress and axial strain for the repair tissue's under the STZ. Thus, more of the load was being supported by the fluid within the repair tissue when it was covered by a normal STZ that when without it. These improvements in stress and axial strain increased as the STZ's permeability became more dependent on strain. This suggests that cells within the protected underlying repair tissue would have a better chance of surviving the healing process and taking on normal functional characteristics, and that this protection would improve with increasing strain-dependent permeability.

3.4. LIMITATIONS

While the results reported here were informative, assumptions were implemented which limit the applicability of these models. Diarthrodial joint surfaces normally experience pressure distributions that vary in magnitude and area of contact during loading. The models reported here did not reflect this since a constant parabolic pressure distribution was applied over a constant area. Further, fluid flow out of articular surfaces is normally modulated by opposing articular surfaces. These models allowed fluid to freely drain from the entire articular surface throughout loading. The effect of restricting fluid flow in the region of contact needs to be modeled to better understand the benefit afforded by the STZ in more in vivo like conditions. Additionally, a normal STZ provides greater stiffness parallel to the articular surface only when resisting tensile loads; not compressive. Modeling the STZ as transversely isotropic allows higher radial stiffness in compression as well as tension. In the current study, the effect of this tension/compression nonlinearity was negligible as only minor compressive radial strain (<1%) was experienced at the outer diameter of loading. All other regions of the STZ remained in tension. Finally, finite deformation was not considered here but should be to more accurately predict responses under higher loads. Adding levels of complexity to these models will enhance their predictive capabilities. Subsequent chapters will describe improvements that were developed for these initial models.

4. STRAIN-DEPENDENT PERMEABILITY – RIGID CONTACT

4.1. OVERVIEW

Results presented in this section pertain to contact loading of transversely isotropic (TI) models (Figure 2.4-1). The models presented here differ from the previous chapter only in the mode of loading; contact loading here, parabolic pressure loading in the previous chapter. All material parameters were unchanged with directional stiffness still modeled as transversely isotropic in the normal STZ only and all other tissues modeled as isotropic linearly elastic materials. The impermeable and permeable loading surfaces used in this chapter were of sufficient stiffness so as to be effectively rigid relative to the cartilage layers loaded (Figure 2.5-2 and Figure 2.5-3). The intent was to cover the range of expected loading responses by the two extremes of either totally restricting fluid flow from the surface in the contact region (impermeable), or allowing it to freely flow (permeable). Both loading conditions allowed a changing contact area during loading resulting in a variable redistribution of load. The range of strain-dependent permeability coefficients investigated in the previous chapter was maintained here to investigate its effect during contact loading. Results reported here were presented in part at SBC 2006 [123].

4.2. RESULTS

4.2.1. Contact Area

After 30sec of loading, contact areas for models loaded by the permeable disks were 6% to 33% greater than for corresponding models loaded by the impermeable disk (Figure 4.2-1, Table 4.2-1). Strain-dependent permeability had no effect on contact areas for permeable or impermeable loading of the full thickness repair without an STZ (i.e. REP-TI). For models including a normal STZ (i.e. NORM-TI and REPwSTZ-TI), increasing strain-dependent permeability in the STZ had the effect of reducing contact area for permeably loaded models but had no effect impermeably loading one. REP-TI experienced greater contact areas than NORM-TI by 2.3 times for impermeable loading and 1.8 to 2.0 times for permeable loading. Addition of a normal STZ over the repair region in REPwSTZ-TI reduced the contact area, as compared to REP-TI, by 29% for impermeable loading and in increasing measure with strain-dependent permeability for permeable loading by 26% to 28%.

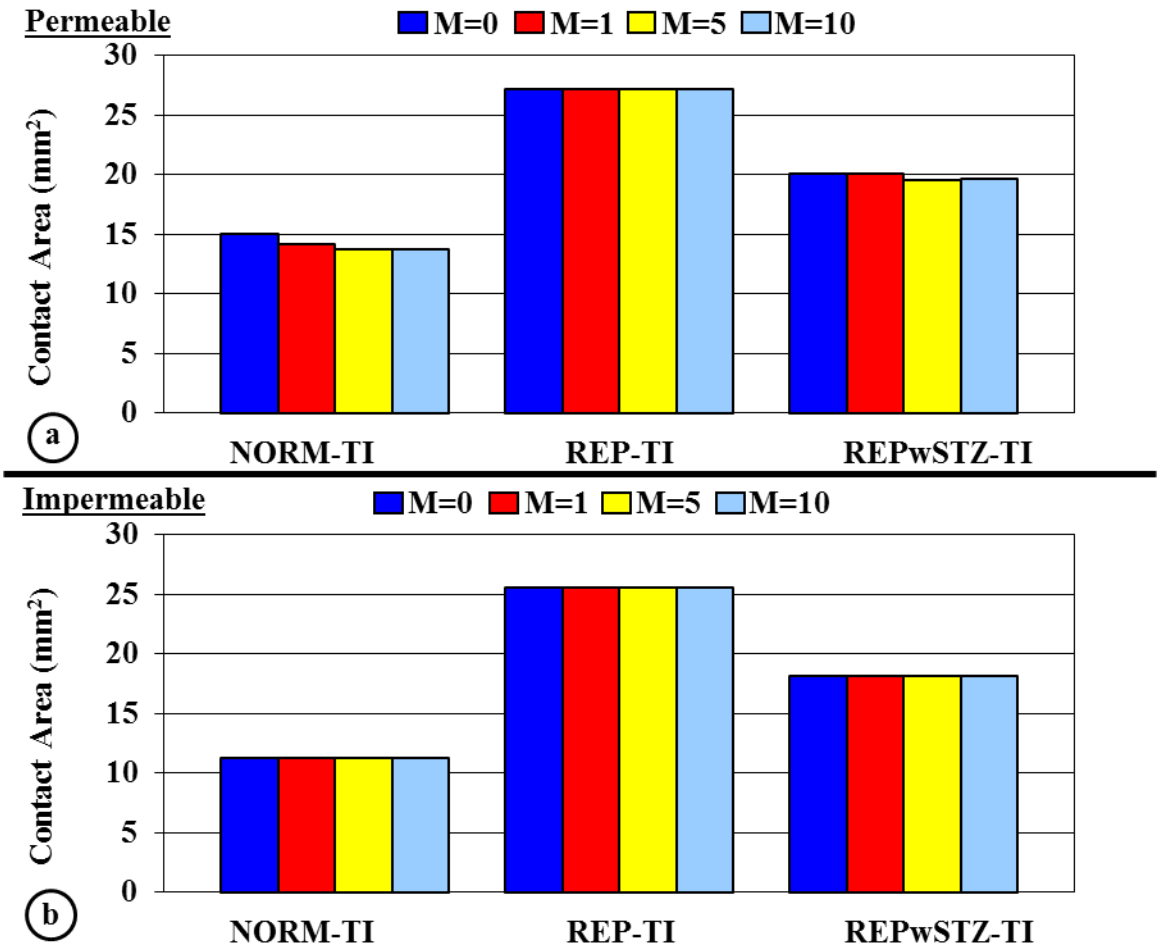

Figure 4.2-1: Area of contact generated for the three models, with increasing levels of strain-dependent permeability in the normal STZ, after 30 sec of loading by a) permeable and b) impermeable rigid loading surfaces.

Table 4.2-1: Relative changes in contact area after 30 sec are shown between permeable (PER) and impermeable (IMP) loading for each model investigated (NORM-TI, REP-TI, and REPwSTZ-TI) and between each model for both loading conditions at each level of strain-dependent permeability modeled in the normal STZ. Impermeable ratios are shown in *italics* and permeable ratios are shown in **bold** for ease of comparison.

RATIOS →	PERMEABLE / IMPERMEABLE			Contact Area REP-TI / NORM-TI		REPwSTZ-TI / REP-TI		REPwSTZ-TI / NORM-TI	
	NORM-TI	REP-TI	REPwSTZ-TI	*IMP*	**PER**	*IMP*	**PER**	*IMP*	**PER**
M=0	1.33	1.06	1.11	*2.26*	**1.81**	*0.71*	**0.74**	*1.60*	**1.33**
M=1	1.25	1.06	1.11	*2.26*	**1.92**	*0.71*	**0.74**	*1.60*	**1.42**
M=5	1.21	1.06	1.08	*2.26*	**1.98**	*0.71*	**0.72**	*1.60*	**1.43**
M=10	1.22	1.06	1.08	*2.26*	**1.97**	*0.71*	**0.72**	*1.60*	**1.42**

4.2.2. Full Thickness Axial Compression

Patterns of differences were seen in compression across the entire thickness at centerline, after 30sec of loading that were similar to those for contact areas. Models loaded by the permeable disks experienced 18% to 41% more compression than the same models loaded by the impermeable disk (Figure 4.2-2, Table 4.2-2). Strain-dependent permeability had no effect on full thickness compression of REP-TI for permeable or impermeable loading. Increasing strain-dependent permeability had the effect of reducing the compression for permeably loaded models that included a normal STZ (i.e. NORM-TI and REPwSTZ-TI), but no effect on those loaded by the impermeable surface. REP-TI experienced greater full thickness compression than NORM-TI by 1.8 times for impermeable loading and by 1.7 to 2.0 times for permeable loading. Addition of a normal STZ over the repair region in REPwSTZ-TI reduced the full thickness compression, as compared to REP-TI, by 20% for impermeable loading and in increasing measure with strain-dependent permeability for permeable loading by 28% to 33%.

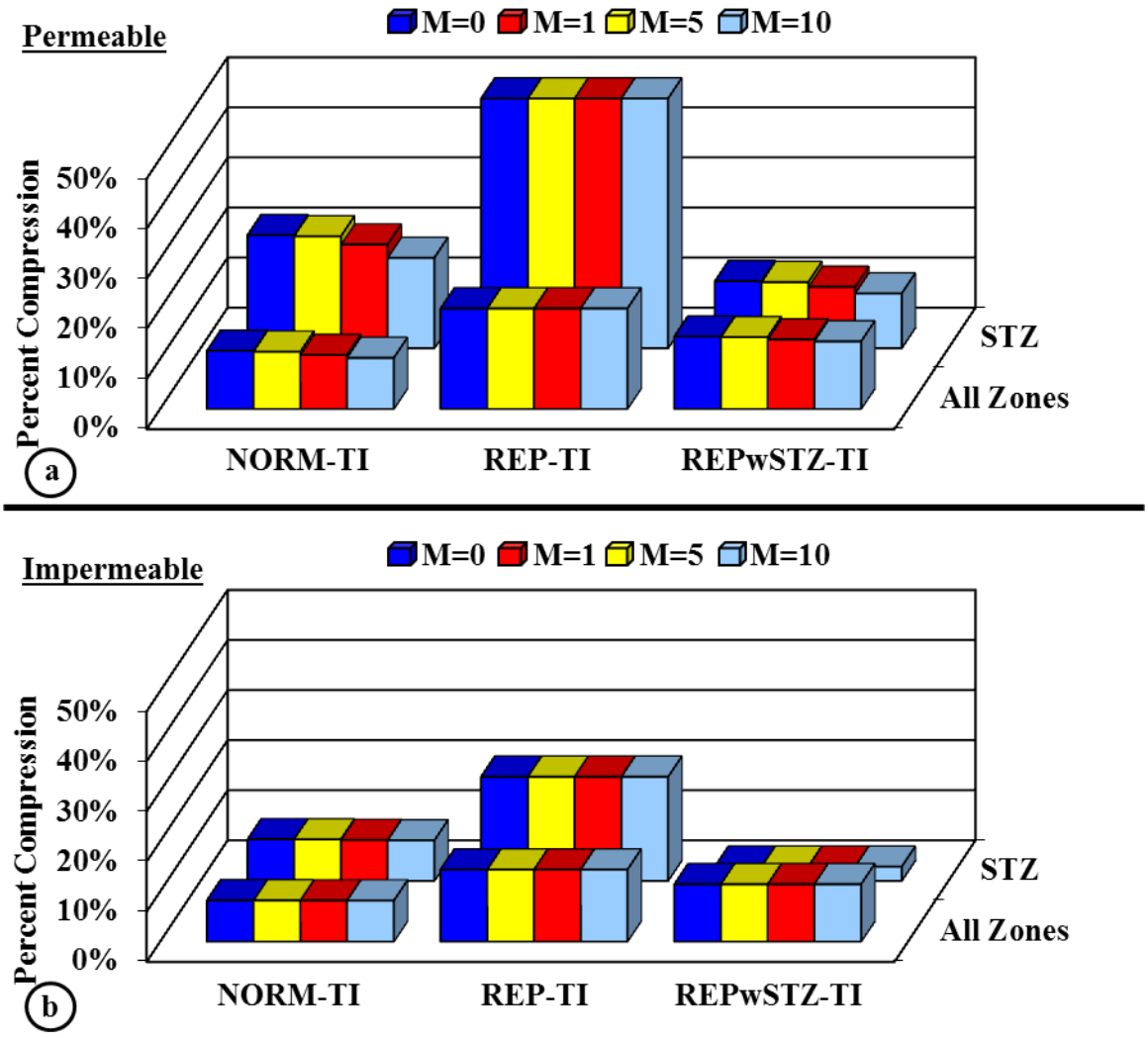

Figure 4.2-2: Compression at centerline of the full thickness (All Zones) and STZ of the three models, with increasing levels of strain-dependent permeability in the normal STZ, after 30sec of loading by permeable (a) and impermeable (b) rigid loading surfaces.

Table 4.2-2: Relative changes in full thickness compression of the full cartilage thickness and of the STZ only after 30 sec of loading are shown between permeable (PER) and impermeable (IMP) loading for each model investigated (NORM-TI, REP-TI, and REPwSTZ-TI) and between each model for both loading conditions at each level of strain-dependent permeability modeled in the normal STZ. Impermeable ratios are shown in *italics* and permeable ratios are shown in **bold** for ease of comparison.

	Full thickness compression at center								
RATIOS →	PERMEABLE / IMPERMEABLE			REP-TI / NORM-TI		REPwSTZ-TI / REP-TI		REPwSTZ-TI / NORM-TI	
	NORM-TI	REP-TI	REPwSTZ-TI	*IMP*	**PER**	*IMP*	**PER**	*IMP*	**PER**
M=0	1.41	1.39	1.26	*1.75*	**1.73**	*0.80*	**0.72**	*1.39*	**1.25**
M=1	1.39	1.39	1.25	*1.75*	**1.76**	*0.80*	**0.71**	*1.39*	**1.25**
M=5	1.31	1.39	1.21	*1.75*	**1.86**	*0.80*	**0.69**	*1.40*	**1.29**
M=10	1.24	1.39	1.18	*1.75*	**1.97**	*0.80*	**0.67**	*1.40*	**1.32**

	STZ compression at center								
RATIOS →	PERMEABLE / IMPERMEABLE			REP-TI / NORM-TI		REPwSTZ-TI / REP-TI		REPwSTZ-TI / NORM-TI	
	NORM-TI	REP-TI	REPwSTZ-TI	*IMP*	**PER**	*IMP*	**PER**	*IMP*	**PER**
M=0	2.72	2.40	4.72	*2.51*	**2.21**	*0.14*	**0.27**	*0.34*	**0.59**
M=1	2.70	2.40	4.65	*2.51*	**2.23**	*0.14*	**0.26**	*0.34*	**0.59**
M=5	2.54	2.40	4.31	*2.55*	**2.41**	*0.14*	**0.25**	*0.35*	**0.59**
M=10	2.23	2.40	3.86	*2.57*	**2.77**	*0.14*	**0.22**	*0.35*	**0.61**

4.2.3. STZ Compression

Compression of the STZ's thickness at center, after 30sec of loading, varied similar to full thickness compression but with the differences magnified. The STZ's in models loaded by the permeable disks experienced 2.2 to 4.7 times as much compression as the same models loaded by the impermeable disk (Figure 4.2-2, Table 4.2-2). Strain-dependent permeability in the surrounding normal STZ had no effect on compression of the uppermost 20% of REP-TI, corresponding to the same region as the STZ in other models but here filled by a full thickness isotropic repair. Increasing strain-dependent permeability had the effect of reducing the STZ's compression for permeably loaded models that included a normal STZ (i.e. NORM-TI and REPwSTZ-TI). Also, in contrast to contact area and full thickness compression, increasing

strain-dependent permeability caused a slight decrease in NORM-TI's STZ for impermeably loaded models, but still did not affect the STZ in REPwSTZ-TI. REP-TI experienced greater compression of the STZ than did NORM-TI by 2.5 to 2.6 times for impermeable loading and 2.2 to 2.8 times for permeable loading. Addition of a normal STZ over the repair region in REPwSTZ-TI reduced the full thickness compression, as compared to REP-TI, by 86% for impermeable loading and in increasing measure with strain-dependent permeability for permeable loading by 73% to 78%.

4.2.4. Axial Strain Beneath the STZ

Changes seen in other parameters were generally reflected in axial strains observed in tissue at center beneath the STZ region. Compressive axial strain under the STZ region was higher in models loaded by the permeable disks by 1.2 to 1.9 times as much compression as the same models loaded by the impermeable disk (Figure 4.2-3, Table 4.2-3). Strain-dependent permeability had no effect on axial strain in REP-TI at the same point corresponding to that just beneath the STZ in other models for permeable or impermeable loading. Increasing strain-dependent permeability had the effect of reducing the axial compressive strain beneath the STZ for permeably loaded models that included a normal STZ (i.e. NORM-TI and REPwSTZ-TI), but no effect on those loaded by the impermeable surface. REP-TI experienced greater compressive axial strain beneath the STZ region than did NORM-TI by 2.1 times for impermeable loading and 1.7 to 2.4 times for permeable loading. Addition of a normal STZ over the repair region in REPwSTZ-TI reduced the axial strain in the repair tissue, as compared to REP-TI, by 21% for impermeable loading. With permeable loading, it actually increased the axial compressive strain by 7% when strain-dependent permeability was absent (M=0) and by

3% when it was very low (M=1); but it decreased the axial strain by 9% when strain-dependent permeability was at normal levels (M=5), and by 18% when at high levels (M=10).

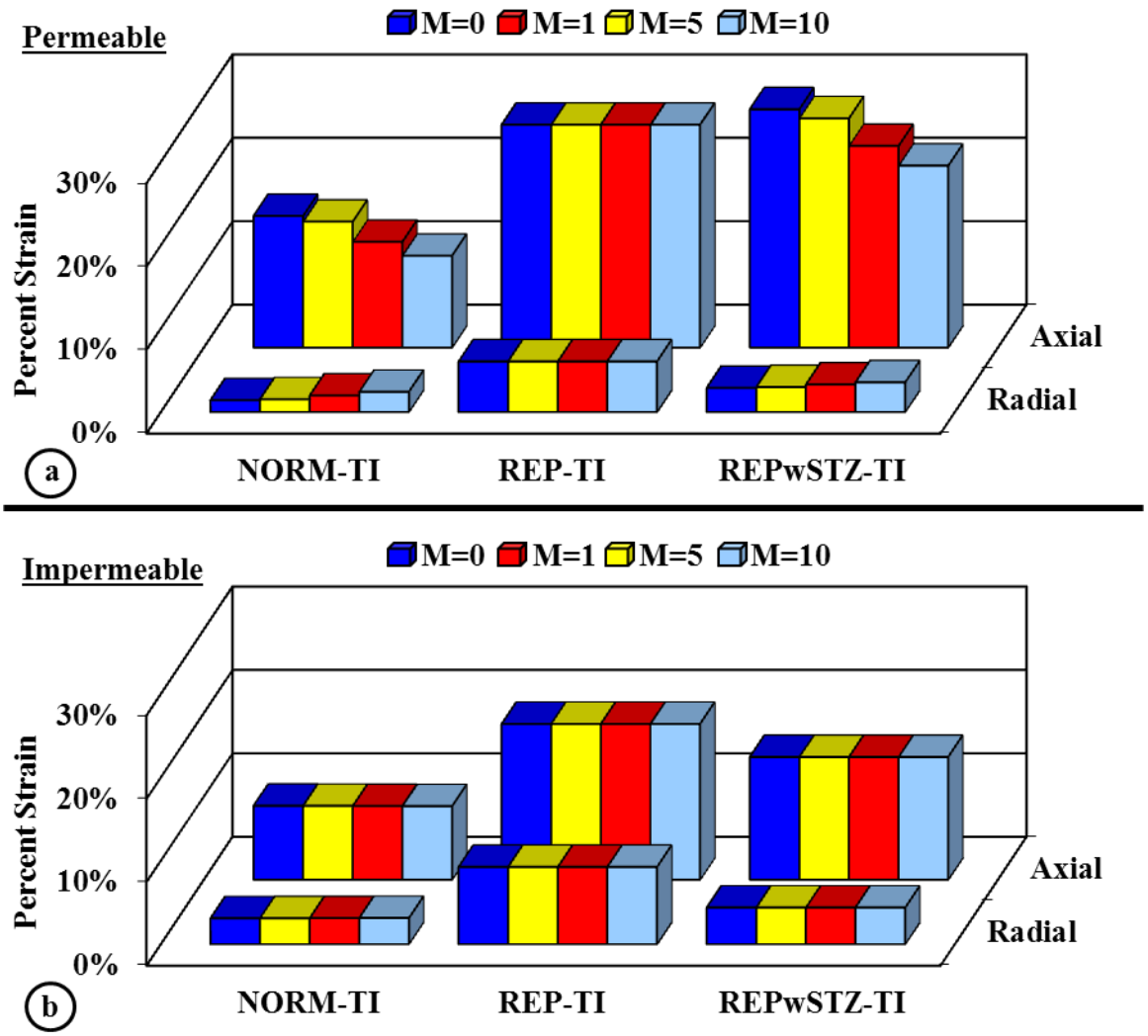

Figure 4.2-3: Percent radial (e11) tensile and axial (e22) compressive strains at centerline of the three models at a point just beneath the STZ region, with increasing levels of strain-dependent permeability in the normal STZ, after 30sec of loading by permeable (a) and impermeable (b) rigid loading surfaces.

Table 4.2-3: Relative changes in percent axial (e_{22}) compressive and radial (e_{11}) tensile strains at a point just beneath the STZ region after 30 sec of loading are shown between permeable (PER) and impermeable (IMP) loading for each model investigated (NORM-TI, REP-TI, and REPwSTZ-TI) and between each model for both loading conditions at each level of strain-dependent permeability modeled in the normal STZ. Impermeable ratios are shown in *italics* and permeable ratios are shown in bold for ease of comparison.

RATIOS →	Axial strain under STZ at center								
	PERMEABLE / IMPERMEABLE			REP-TI / NORM-TI		REPwSTZ-TI / REP-TI		REPwSTZ-TI / NORM-TI	
	NORM-TI	REP-TI	REPwSTZ-TI	*IMP*	**PER**	*IMP*	**PER**	*IMP*	**PER**
M=0	1.78	1.43	1.94	*2.11*	**1.69**	*0.79*	**1.07**	*1.66*	**1.81**
M=1	1.70	1.43	1.87	*2.11*	**1.77**	*0.79*	**1.03**	*1.66*	**1.82**
M=5	1.43	1.43	1.64	*2.12*	**2.11**	*0.79*	**0.91**	*1.67*	**1.91**
M=10	1.25	1.43	1.48	*2.12*	**2.43**	*0.79*	**0.82**	*1.67*	**1.98**

RATIOS →	Radial strain under STZ at center								
	PERMEABLE / IMPERMEABLE			REP-TI / NORM-TI		REPwSTZ-TI / REP-TI		REPwSTZ-TI / NORM-TI	
	NORM-TI	REP-TI	REPwSTZ-TI	*IMP*	**PER**	*IMP*	**PER**	*IMP*	**PER**
M=0	0.46	0.66	0.66	*2.98*	**4.27**	*0.47*	**0.48**	*1.42*	**2.04**
M=1	0.49	0.66	0.68	*2.98*	**3.95**	*0.47*	**0.49**	*1.41*	**1.95**
M=5	0.64	0.66	0.75	*2.96*	**3.05**	*0.47*	**0.54**	*1.41*	**1.66**
M=10	0.77	0.66	0.81	*2.95*	**2.51**	*0.47*	**0.59**	*1.40*	**1.47**

4.2.5. Radial Strain Beneath the STZ

Patterns of changes in radial tensile strains under the STZ region differed from those for axia compressive strains. Radial tensile strains were lower in models loaded by the permeable disks by 19% to 54% as compared to the same models loaded by the impermeable disk (Figure 4.2-3, Table 4.2-3). Strain-dependent permeability had no effect on radial tensile strain in REP-TI at the same point corresponding to that just beneath the STZ in other models for permeable or impermeable loading. Increasing strain-dependent permeability had the effect of increasing the radial tensile strain beneath the STZ for permeably loaded models that included a normal STZ (i.e. NORM-TI and REPwSTZ-TI), but no effect on those loaded by the impermeable surface. REP-TI experienced greater radial tensile strain beneath the STZ region than did NORM-TI by

3.0 times for impermeable loading and 2.5 to 4.3 times for permeable loading. Addition of a normal STZ over the repair region in REPwSTZ-TI reduced the radial tensile strain in the repair tissue, as compared to REP-TI, by 53% for impermeable loading. With permeable loading, it decreased the radial tensile strain but to lesser degrees as strain-dependent permeability was increased: by 52% for M=0 to 41% when at high levels (M=10).

4.2.6. von Mises Stress

Comparable to the last chapter, but here for both impermeable and permeable loading, von Mises stresses for the normal model (NORM-TI) were highest at the center of the articular surface and dispersed through the thickness and radially outward through the cartilage layer (Figure 4.2-4). The contour plot for impermeable loading of NORM-TI reveals higher von Mises toward the under-side of the STZ; whereas, the permeable contour plot suggests a shift of von Mises stresses to the surface. Whether loaded by the impermeable or permeable sphere, von Mises stresses in REP-TI were very low in the repair tissue central to the cartilage layer and stresses spread radially into more of the surrounding tissues. An obvious stress gradient can be seen in REP-TI's contour plot through the entire cartilage thickness at the interface between the central repair and the surrounding normal tissue, for loading by either sphere. In REPwSTZ-TI, the normal STZ over the repair region resulted in some restoration of von Mises stress at the center of the articular surface and some reduction in stresses experienced by the surrounding normal tissues for impermeable and permeable loading. Further, the von Mises stress gradient at the repair to normal interface in REPwSTZ-TI was attenuated.

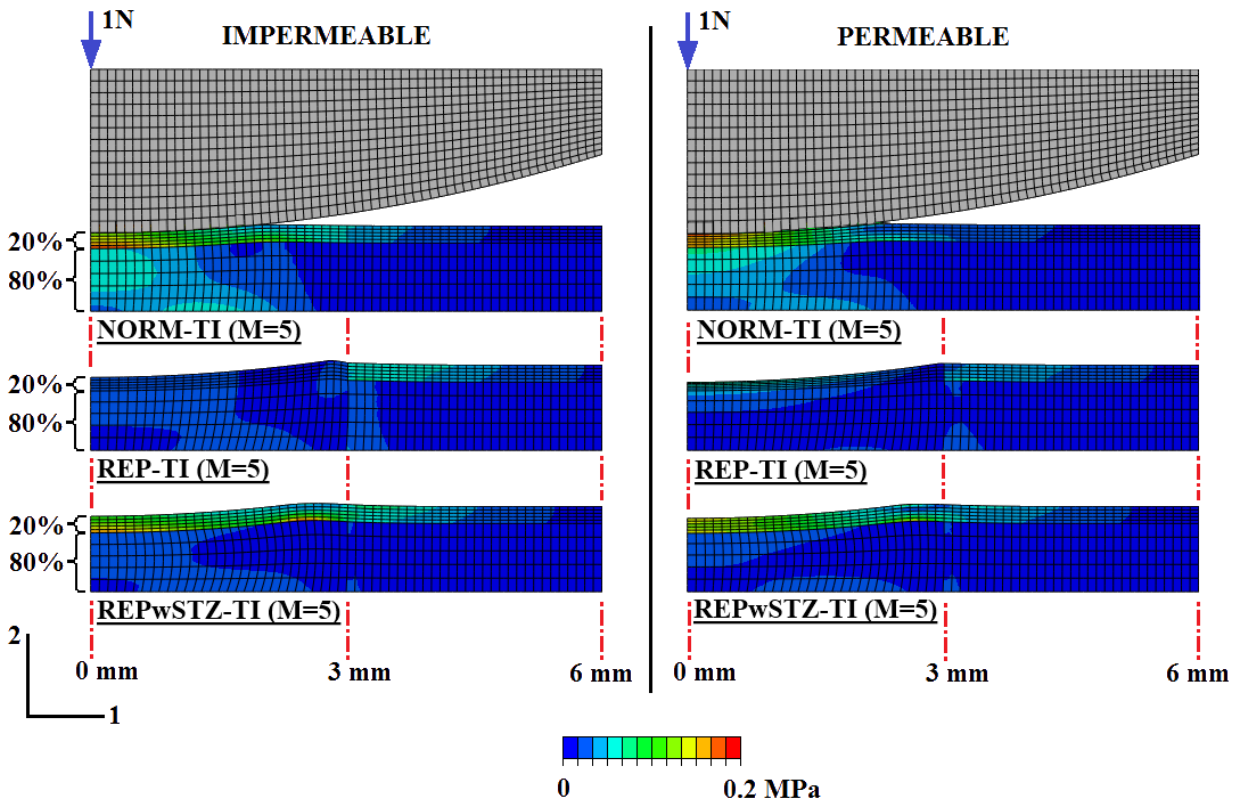

Figure 4.2-4: Contour plots of von Mises stress in the cartilage layers of the three models after 30 sec of loading by relatively rigid impermeable and permeable loading surfaces. Models shown are based on a mid-range strain-dependent coefficient (M=5), but are representative of patterns seen for all values. The loading surfaces are shown on NORM-TI only for illustrative purposes.

On the surface, von Mises stresses were higher for permeably loaded models by 1.1 to 2.2 times that of the same models loaded by the impermeable disk (Figure 4.2-5, Table 4.2-4). Strain-dependent permeability had no effect on von Mises stress on the surface of REP-TI for permeable or impermeable loading. Increasing strain-dependent permeability had the effect of increasing the surface von Mises stress for permeably loaded models that included a normal STZ (i.e. NORM-TI and REPwSTZ-TI), but no effect on those loaded by the impermeable surface. REP-TI's surface experienced less von Mises stress than NORM-TI by 76% to 75% for impermeable loading and by 51% to 62% for permeable loading as strain-dependent permeability was increased. Addition of a normal STZ over the repair region in REPwSTZ-TI increased the

surface von Mises stress, as compared to REP-TI, by a factor of 3.2 for impermeable loading and in increasing measure with strain-dependent permeability for permeable loading by 1.9 to 2.1 times.

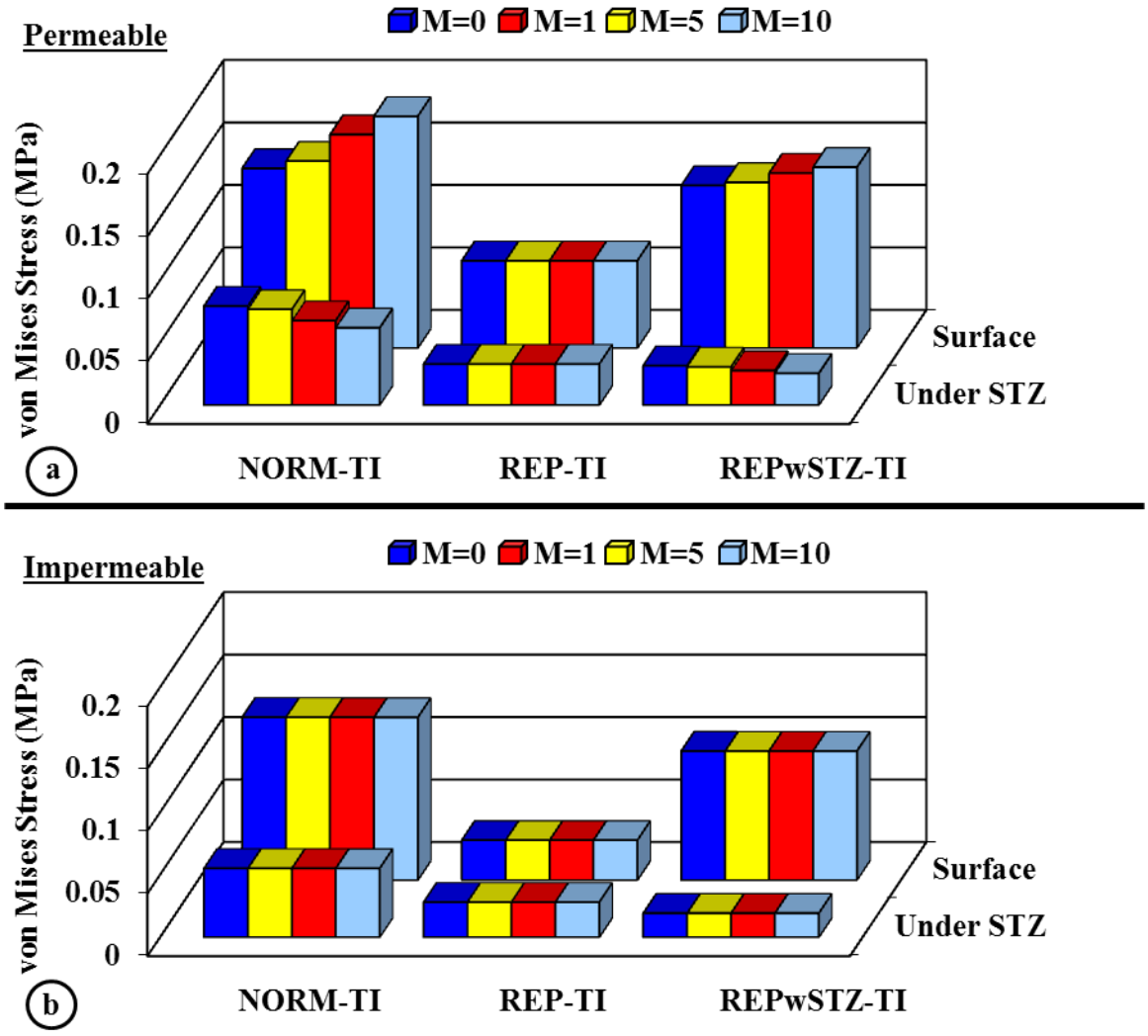

Figure 4.2-5: von Mises stress at centerline of the three models on the articular surface and at a point just beneath the STZ region, with increasing levels of strain-dependent permeability in the normal STZ, after 30sec of loading by permeable (a) and impermeable (b) rigid loading surfaces.

Table 4.2-4: Relative changes in von Mises stress on the articular surface and at a point just beneath the STZ region after 30 sec of loading are shown between permeable (PER) and impermeable (IMP) loading for each model investigated (NORM-TI, REP-TI, and REPwSTZ-TI) and between each model for both loading conditions at each level of strain-dependent permeability modeled in the normal STZ. Impermeable ratios are shown in *italics* and permeable ratios are shown in bold for ease of comparison.

RATIOS →	von Mises stress on surface at center								
	PERMEABLE / IMPERMEABLE			REP-TI / NORM-TI		REPwSTZ-TI / REP-TI		REPwSTZ-TI / NORM-TI	
	NORM-TI	REP-TI	REPwSTZ-TI	*IMP*	**PER**	*IMP*	**PER**	*IMP*	**PER**
M=0	1.10	2.18	1.26	*0.24*	**0.49**	*3.24*	**1.86**	*0.79*	**0.90**
M=1	1.15	2.18	1.28	*0.24*	**0.47**	*3.24*	**1.90**	*0.79*	**0.89**
M=5	1.31	2.18	1.36	*0.24*	**0.41**	*3.24*	**2.01**	*0.79*	**0.82**
M=10	1.42	2.18	1.40	*0.25*	**0.38**	*3.23*	**2.07**	*0.79*	**0.78**

RATIOS →	von Mises stress under STZ at center								
	PERMEABLE / IMPERMEABLE			REP-TI / NORM-TI		REPwSTZ-TI / REP-TI		REPwSTZ-TI / NORM-TI	
	NORM-TI	REP-TI	REPwSTZ-TI	*IMP*	**PER**	*IMP*	**PER**	*IMP*	**PER**
M=0	1.44	1.17	1.65	*0.51*	**0.41**	*0.68*	**0.96**	*0.35*	**0.40**
M=1	1.39	1.17	1.59	*0.51*	**0.43**	*0.68*	**0.93**	*0.35*	**0.40**
M=5	1.23	1.17	1.44	*0.51*	**0.49**	*0.68*	**0.84**	*0.35*	**0.41**
M=10	1.12	1.17	1.33	*0.51*	**0.53**	*0.68*	**0.77**	*0.35*	**0.41**

Just under the STZ, at the model centers, von Mises stresses were also higher for permeably loaded models by 1.1 to 1.7 times that of the same models loaded by the impermeable disk (Figure 4.2-5, Table 4.2-4). Strain-dependent permeability had no effect on von Mises stress under the STZ of REP-TI for permeable or impermeable loading. Increasing strain-dependent permeability had the effect of decreasing the von Mises stress under the STZ for permeably loaded models that included a normal STZ (i.e. NORM-TI and REPwSTZ-TI), but no effect on those loaded by the impermeable surface. REP-TI experienced less von Mises stress than NORM-TI under the STZ region by 49% for impermeable loading and by 59% to 47% for permeable loading as strain-dependent permeability was increased. Addition of a normal STZ over the repair region in REPwSTZ-TI decreased the von Mises stress under the STZ, as

compared to REP-TI, by 32% for impermeable loading and in increasing measure with strain-dependent permeability for permeable loading by 4% to 23%.

4.2.7. Fluid Pressure

Pore fluid pressure was highest in the center of the models and decreased radially, for both impermeable and permeable loading (Figure 4.2-6). For impermeable loading, fluid flow out of the surface in the contact region was restricted; thus, fluid pressure varied little through the thickness of the cartilage layers at any point. For permeable loading, pressure varied through the thickness since by definition the pressure was zero everywhere on the surface and fluid was allowed to freely flow from the entire surface.

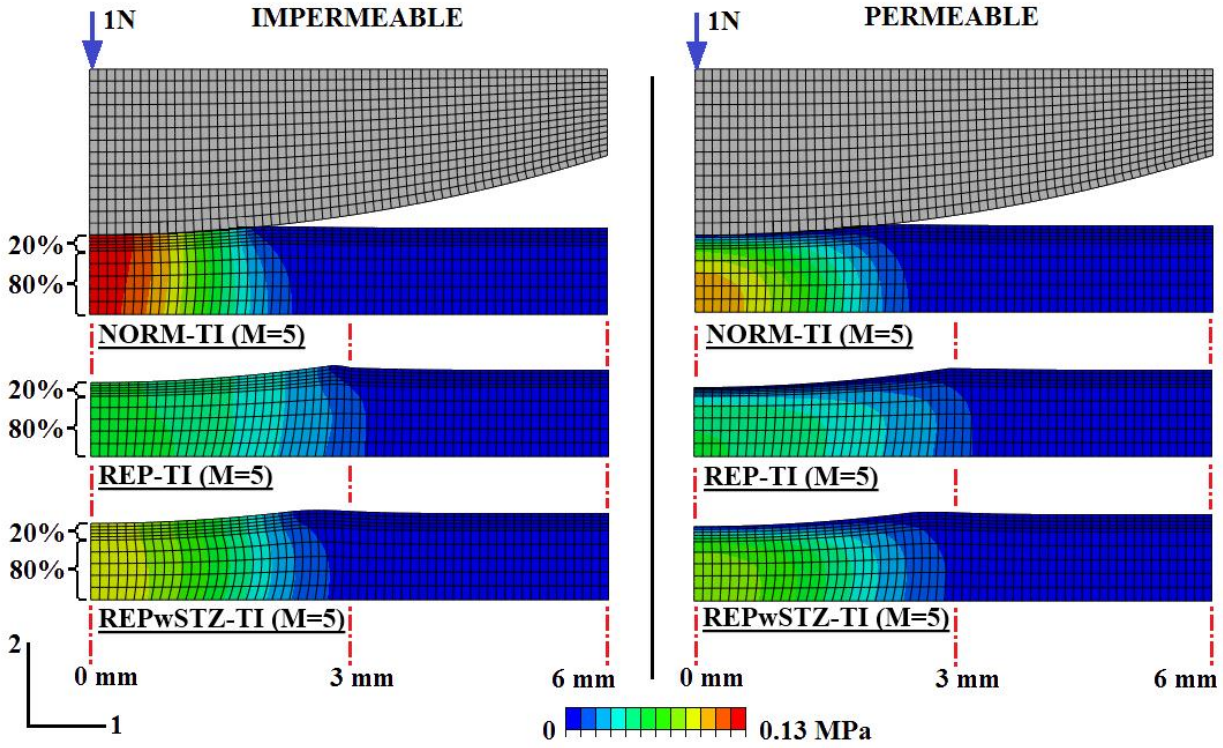

Figure 4.2-6: Contour plots of pore fluid pressure in the cartilage layers of the three models after 30 sec of loading by relatively rigid impermeable and permeable loading surfaces. Models shown are based on a mid-range strain-dependent coefficient (M=5), but are representative of patterns seen for all values. The loading surfaces are shown on NORM-TI only for illustrative purposes.

Immediately beneath the STZ, at the model centers, fluid pressure was lower for permeably loaded models by 23% to 71% compared to the same models loaded by the impermeable disk (Figure 4.2-7, Table 4.2-5). Strain-dependent permeability had no effect on fluid pressure in REP-TI at the same point corresponding to that just beneath the STZ in other models for permeable or impermeable loading. Increasing strain-dependent permeability had the effect of increasing the fluid pressure under the STZ for permeably loaded models that included a normal STZ (i.e. NORM-TI and REPwSTZ-TI), but no significant effect on those loaded by the impermeable surface. REP-TI experienced lower fluid pressure under the STZ than did NORM-TI by 56% for impermeable loading and by 16% to 68% for permeable loading as strain-dependent permeability was increased. Addition of a normal STZ over the repair region in REPwSTZ-TI increased the fluid pressure under the STZ, as compared to REP-TI, by a factor of 1.7 for impermeable loading and in increasing measure with strain-dependent permeability for permeable loading by 1.7 to 2.3 times.

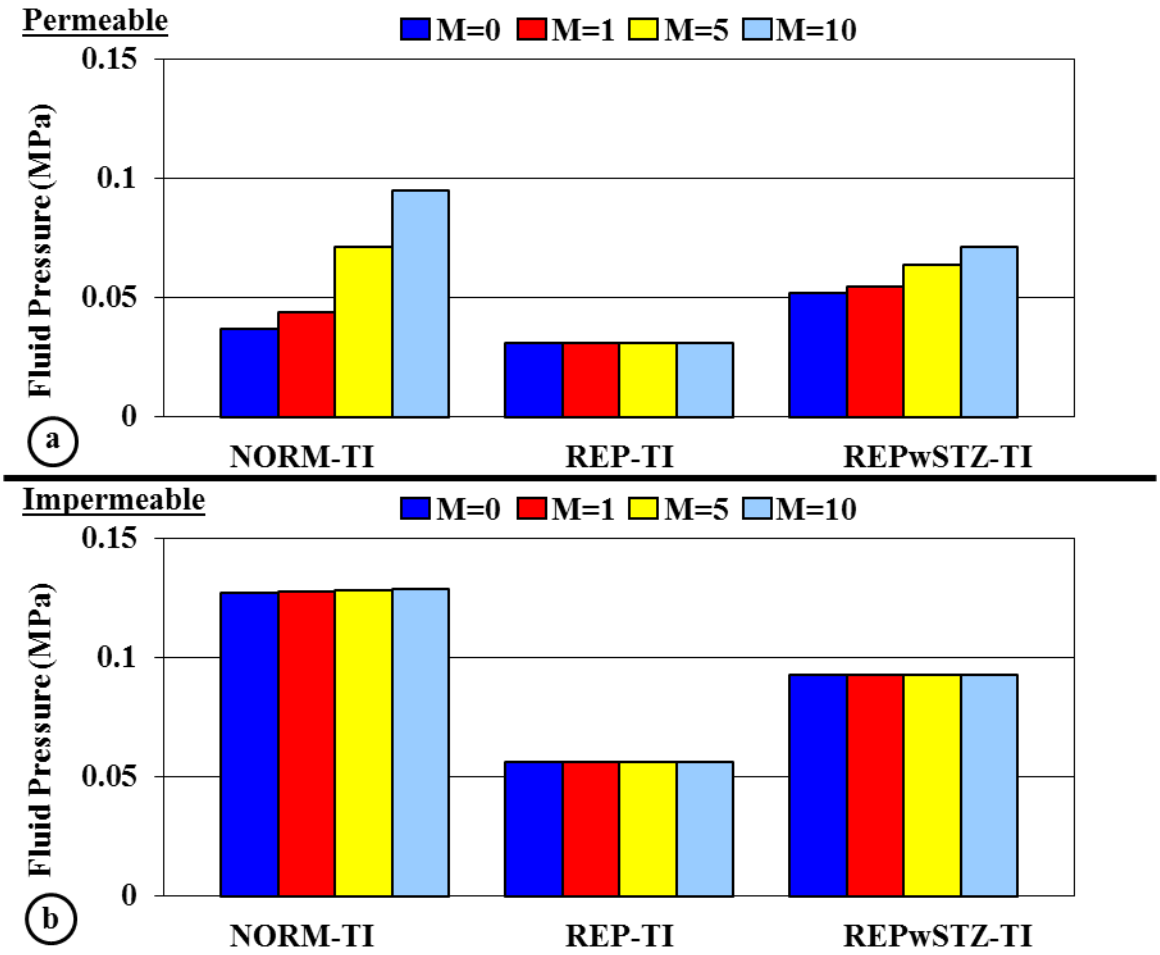

Figure 4.2-7: Fluid pressure at centerline of the three models at a point just beneath the STZ region, with increasing levels of strain-dependent permeability in the normal STZ, after 30sec of loading by permeable (a) and impermeable (b) rigid loading surfaces.

Table 4.2-5: Relative changes in fluid pressure a point just beneath the STZ region after 30 sec of loading are shown between permeable (PER) and impermeable (IMP) loading for each model investigated (NORM-TI, REP-TI, and REPwSTZ-TI) and between each model for both loading conditions at each level of strain-dependent permeability modeled in the normal STZ. Impermeable ratios are shown in *italics* and permeable ratios are shown in **bold** for ease of comparison.

RATIOS →	Fluid pressure under STZ at center								
	PERMEABLE / IMPERMEABLE			REP-TI / NORM-TI		REPwSTZ-TI / REP-TI		REPwSTZ-TI / NORM-TI	
	NORM-TI	REP-TI	REPwSTZ-TI	*IMP*	**PER**	*IMP*	**PER**	*IMP*	**PER**
M=0	0.29	0.55	0.56	*0.44*	**0.84**	*1.65*	**1.69**	*0.73*	**1.41**
M=1	0.34	0.55	0.59	*0.44*	**0.70**	*1.65*	**1.78**	*0.73*	**1.25**
M=5	0.56	0.55	0.69	*0.44*	**0.43**	*1.65*	**2.08**	*0.72*	**0.90**
M=10	0.74	0.55	0.77	*0.44*	**0.32**	*1.65*	**2.31**	*0.72*	**0.75**

4.2.8. Rate of Fluid Loss

After 30sec of loading, fluid flow for permeable loaded models was axially directed and highest at the surface (Figure 4.2-8). Fluid flow for impermeably loaded models was more radially directed and of greater magnitude deeper into the tissue as compared to permeable loading. For both impermeable and permeable loading, fluid flow patterns and magnitudes in REP deviated greatly from NORM-TI. Restoration of the normal patterns and magnitudes were approached in REPwSTZ-TI (Figure 4.2-9).

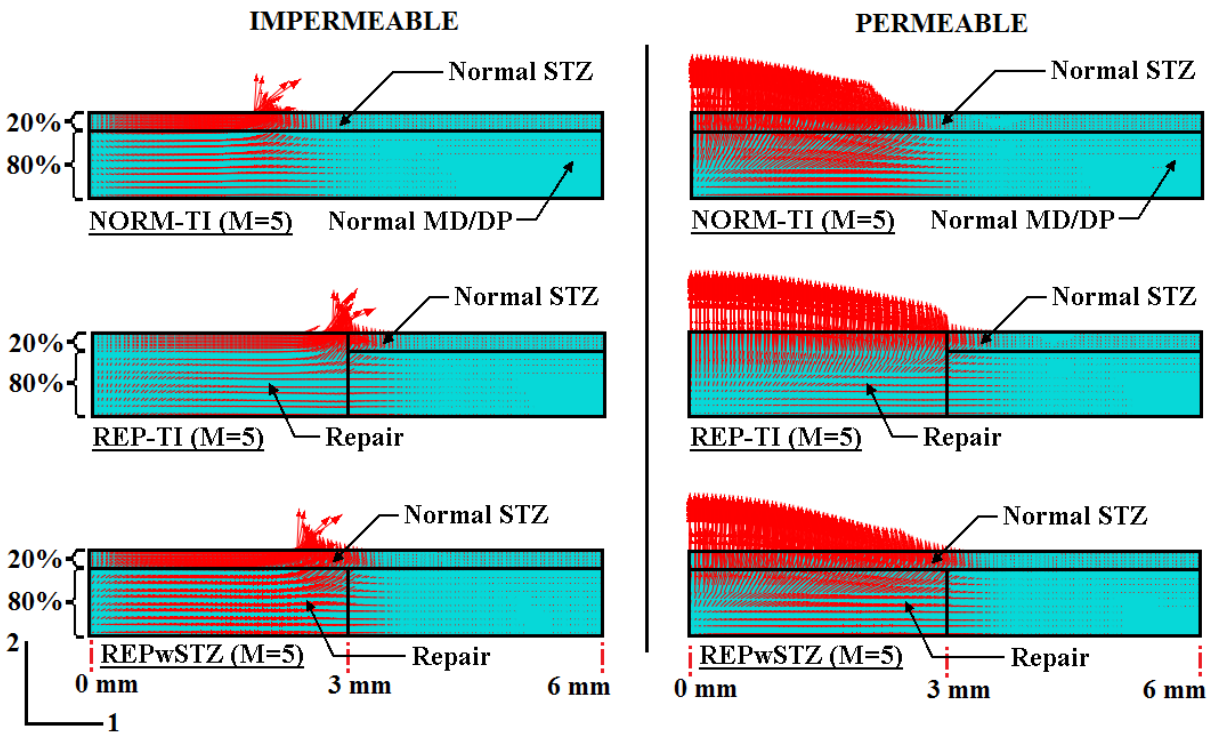

Figure 4.2-8: Effective fluid velocity gradient distributions after 30 sec of loading by relatively rigid impermeable and permeable loading surfaces superimposed on undeformed representations of cartilage layers for the three models. Only the central 6mm is shown in order to magnify the flow patterns; flow beyond 6mm was minimal. Areas of different material behavior are outlined. Models shown are based on a mid-range strain-dependent coefficient (M=5), but are representative of patterns seen for all values. The loading surfaces are not shown.

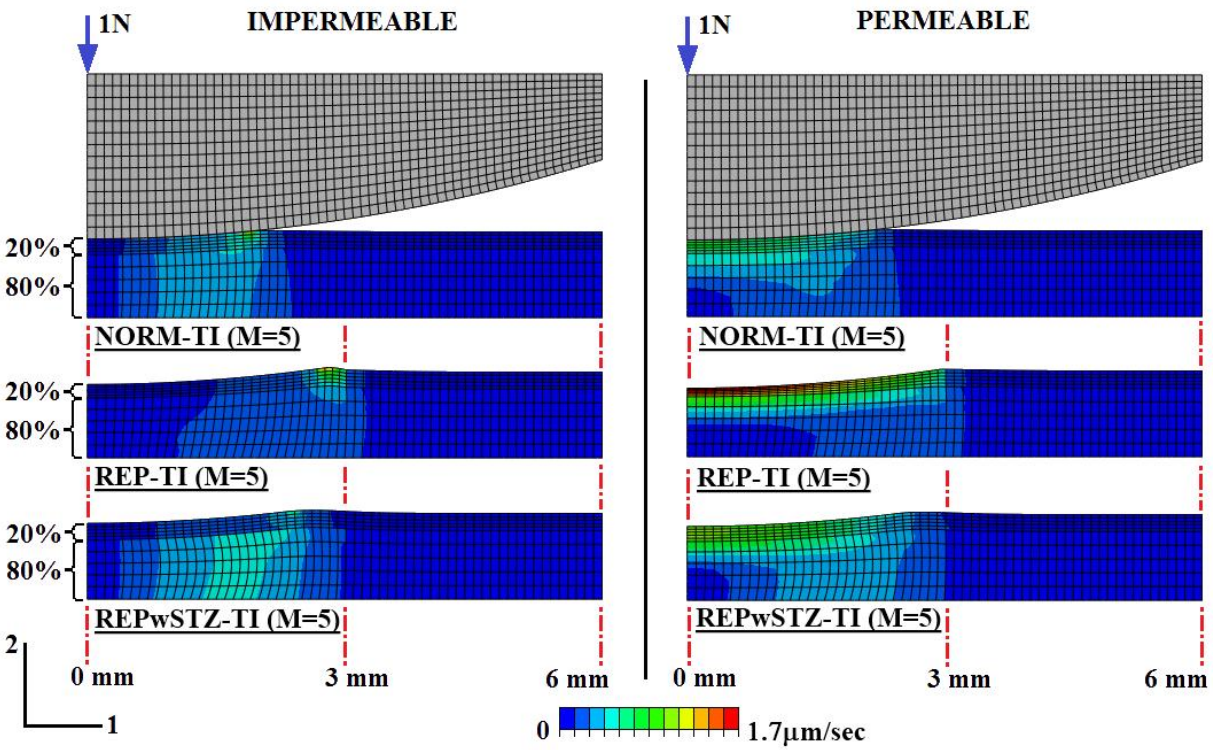

Figure 4.2-9: Contour plots of effective fluid velocity magnitudes in the cartilage layers of the three models after 30 sec of loading by relatively rigid impermeable and permeable loading surfaces. Models shown are based on a mid-range strain-dependent coefficient (M=5), but are representative of patterns seen for all values. The loading surfaces are shown on NORM-TI only for illustrative purposes.

4.2.9. Parabolic Pressure versus Permeable Contact Loading

A comparison between results reported in this chapter for permeable loading and those reported in the last chapter for parabolic pressure loading are in order given the common features of the two approaches. Both allowed free flow of fluids from the articular surface throughout loading, and material properties of the models loading by the two approaches were identical. They primarily differed in that contact loading allowed the area over which the load was applied to vary as needed, whereas loading by the pressure distribution was constant. A side-by-side compilation of relative differences between models reported in tables of the preceding chapter and in this chapter contrasts the two approaches (Table 4.2-6). In general, the parabolic pressure

approach tended to overestimate relative differences between repair models (REP-TI and REPwSTZ-TI) and the normal model (NORM-TI) and to underestimate relative improvements seen in REPwSTZ-TI as compared to REP-TI.

Table 4.2-6: Comparison of relative differences between models (NORM-TI, REP-TI, and REPwSTZ-TI) after 30 sec of loading as predicted by parabolic (PAR) pressure loading (chapter 3) and permeable (PER) contact loading at each level of strain-dependent permeability modeled in the normal STZ. Parabolic ratios are shown in *italics* and permeable ratios are shown in **bold** for ease of comparison.

	Full thickness compression at center						STZ compression at center					
RATIOS →	REP-TI / NORM-TI		REPwSTZ-TI / REP-TI		REPwSTZ-TI / NORM-TI		REP-TI / NORM-TI		REPwSTZ-TI / REP-TI		REPwSTZ-TI / NORM-TI	
	PAR	**PER**	*PAR*	**PER**	*PAR*	**PER**	*PAR*	**PER**	*PAR*	**PER**	*PAR*	**PER**
M=0	*3.31*	**1.73**	*0.45*	**0.72**	*1.48*	**1.25**	*4.07*	**2.21**	*0.21*	**0.27**	*0.84*	**0.59**
M=1	*3.46*	**1.76**	*0.43*	**0.71**	*1.48*	**1.25**	*4.20*	**2.23**	*0.20*	**0.26**	*0.84*	**0.59**
M=5	*4.10*	**1.86**	*0.37*	**0.69**	*1.50*	**1.29**	*4.80*	**2.41**	*0.17*	**0.25**	*0.84*	**0.59**
M=10	*4.85*	**1.97**	*0.32*	**0.67**	*1.56*	**1.32**	*5.64*	**2.77**	*0.15*	**0.22**	*0.84*	**0.61**

	Axial strain under STZ at center						Radial strain under STZ at center					
RATIOS →	REP-TI / NORM-TI		REPwSTZ-TI / REP-TI		REPwSTZ-TI / NORM-TI		REP-TI / NORM-TI		REPwSTZ-TI / REP-TI		REPwSTZ-TI / NORM-TI	
	PAR	**PER**	*PAR*	**PER**	*PAR*	**PER**	*PAR*	**PER**	*PAR*	**PER**	*PAR*	**PER**
M=0	*3.37*	**1.69**	*0.78*	**1.07**	*2.63*	**1.81**	*6.75*	**4.27**	*0.27*	**0.48**	*1.84*	**2.04**
M=1	*3.62*	**1.77**	*0.72*	**1.03**	*2.61*	**1.82**	*6.41*	**3.95**	*0.28*	**0.49**	*1.78*	**1.95**
M=5	*4.73*	**2.11**	*0.55*	**0.91**	*2.61*	**1.91**	*5.51*	**3.05**	*0.30*	**0.54**	*1.63*	**1.66**
M=10	*6.09*	**2.43**	*0.44*	**0.82**	*2.68*	**1.98**	*4.93*	**2.51**	*0.31*	**0.59**	*1.55*	**1.47**

	von Mises stress on surface at center						von Mises stress under STZ at center					
RATIOS →	REP-TI / NORM-TI		REPwSTZ-TI / REP-TI		REPwSTZ-TI / NORM-TI		REP-TI / NORM-TI		REPwSTZ-TI / REP-TI		REPwSTZ-TI / NORM-TI	
	PAR	**PER**	*PAR*	**PER**	*PAR*	**PER**	*PAR*	**PER**	*PAR*	**PER**	*PAR*	**PER**
M=0	*0.83*	**0.49**	*1.41*	**1.86**	*1.17*	**0.90**	*0.76*	**0.41**	*0.74*	**0.96**	*0.56*	**0.40**
M=1	*0.82*	**0.47**	*1.43*	**1.90**	*1.17*	**0.89**	*0.81*	**0.43**	*0.69*	**0.93**	*0.56*	**0.40**
M=5	*0.78*	**0.41**	*1.48*	**2.01**	*1.15*	**0.82**	*1.04*	**0.49**	*0.53*	**0.84**	*0.55*	**0.41**
M=10	*0.74*	**0.38**	*1.52*	**2.07**	*1.13*	**0.78**	*1.30*	**0.53**	*0.43*	**0.77**	*0.56*	**0.41**

	Fluid pressure under STZ at center						Fluid loss rate from surface at center					
RATIOS →	REP-TI / NORM-TI		REPwSTZ-TI / REP-TI		REPwSTZ-TI / NORM-TI		REP-TI / NORM-TI		REPwSTZ-TI / REP-TI		REPwSTZ-TI / NORM-TI	
	PAR	**PER**	*PAR*	**PER**	*PAR*	**PER**	*PAR*	**PER**	*PAR*	**PER**	*PAR*	**PER**
M=0	*1.39*	**0.84**	*1.19*	**1.69**	*1.65*	**1.41**	*2.91*	**1.85**	*0.55*	**0.78**	*1.59*	**1.44**
M=1	*1.26*	**0.70**	*1.23*	**1.78**	*1.56*	**1.25**	*3.11*	**1.88**	*0.49*	**0.74**	*1.54*	**1.40**
M=5	*0.97*	**0.43**	*1.36*	**2.08**	*1.33*	**0.90**	*4.37*	**2.28**	*0.33*	**0.61**	*1.42*	**1.39**
M=10	*0.84*	**0.32**	*1.45*	**2.31**	*1.21*	**0.75**	*7.78*	**3.19**	*0.18*	**0.49**	*1.41*	**1.56**

4.3. SUMMARY

The models presented here differed only in the mode of loading from those reported in the previous chapter. In the last chapter, models were loaded by an unchanging parabolic pressure distribution applied over a constant area. Fluid was allowed to freely drain from the entire articular surface throughout the duration of loading. In this chapter, the same models were loaded but by contact from relatively rigid impermeable and permeable surfaces. The use of contact allowed the load to be distributed over an area that changed with time as the loaded layers deformed. Fluid was again allowed to freely flow from the entire articular surface when loaded by the permeable disk, but was prevented from flowing out of the surface in the region of contact when loaded by the impermeable disk.

In many ways, the results for contact loading were comparable to those of the previous chapter. The full thickness repair (REP-TI) did not perform as well as the normal model (NORM-TI) under load. REP-TI's solid matrix developed lower stresses while suffering greater strains and overall deformations reflecting the reduced ability of its' solid matrix to support loads. Lower fluid pressures in REP-TI indicated greater fluid loss and highlighted its' reduced ability to retain fluids. The placement of a normal STZ over the repair region in REPwSTZ-TI improved these outcomes, though not totally to the level of the normal model. Also, permeable contact loading similarly revealed that benefits of a normal STZ covering over the repair region improved as permeability with the STZ became more dependent on volumetric strain.

In contrast, strain-dependent permeability afforded no added benefit for models loaded by the impermeable surface. When the impermeable disk blocked fluid flow from the region of contact, higher tensile stiffness in the STZ was the sole cause for observed improvements. Also because of the restricted fluid flow, impermeably loaded models in general performed better than

permeably loaded ones. Finally, the more realistic approximation of the contact models to normally redistribute load as the underlying cartilage layer deformed revealed that the previously used constant pressure distribution overestimated the negative effects of an unprotected repair and underestimated the benefits of adding a normal STZ covering.

Normal diarthrodial joints likely experience fluid flow conditions that fall in between those modeled in this chapter. A normal cartilage layer loading a repair surface would likely allow some fluid to exude from the repair in the region of contact though not in a totally uninhibited fashion. Thus, the impermeable and permeable surfaces modeled here provide a range of loading responses that may be interpreted as bracketing that which would be expected in normal diarthrodial joints. Though the contact models predictions are congruent with the findings of the last chapter, their predictions are more focused. The contact models not only imply that a normally loaded repair surface would benefit from a STZ with strain-dependent permeability. They further reveal that the benefit is primarily driven by the higher tensile stiffness of the STZ while being augmented by strain-dependent permeability in the STZ as fluid is exuded from the loaded surface.

4.4. LIMITATIONS

The contact models in this chapter, though more sophisticated that the initial models, still do not address all of the limitations outlined in chapter 3. Though the extreme responses here modeled (i.e. total restriction of fluid flow in the region of contact vs. free-draining) are believed to bracket the response that would be exhibited when loading the models by a normal cartilage layer, this has yet to be proven. Models that simulate contact loading between two deformable articular surfaces such that changes in contact area and flow between those surfaces are allowed, as dictated by loading and the material properties of those surfaces, are still desired. Also, there

is still a need to replace transverse isotropy with a more realistic representation of tension/compression nonlinearity. Lastly, finite deformation needs to be included to allow for more reliable results with large deformations. Efforts to address these remaining features will be addressed in subsequent chapters.

5. TENSION-COMPRESSION NONLINEARITY – RIGID CONTACT

5.1. OVERVIEW

Results presented in this section include the effect of changing material property definitions in normal cartilage and of including nonlinear geometric contributions overall. TI models reported in the last chapter (Figure 2.4-1) were replaced by TC models as defined in chapter 2 (Figure 2.4-2). The flat TC models differ from the TI models only in the replacement of transversely isotropic material behavior in the normal STZ, and of the isotropic behavior in the normal MD/DP zones, with bilinearly elastic tension-compression approximations appropriate to those zones. In addition to the changes in material definitions, finite deformation was accounted for via Abaqus' nonlinear geometry feature (NLGEOM) which defines strain as the log of the stretch ratio. Isotropic linearly elastic material definitions for the repair tissues remained as adequately reflecting homogeneous tissues of inferior stiffness relative to normal tissues. The impermeable and permeable loading surfaces used in the previous chapter remained (Figure 2.5-2 and Figure 2.5-3), as did the applied load and boundary conditions. Since the benefits of increasing strain-dependent permeability was established in earlier chapters, only a mid-range value (M=5) was used here to simulate the benefit normally found in cartilage. Results reported here were presented in part at SBC 2008 [124].

5.2. RESULTS

5.2.1. Contact Area

After 30sec of loading, contact areas for models loaded by the permeable disks were 8% to 25% greater than for corresponding models loaded by the impermeable disk (Figure 5.2-1, Table 5.2-1). REP-TC experienced greater contact areas than NORM-TC by 2.1 times for impermeable loading and 1.9 times for permeable loading (Table 5.2-2). Addition of a normal STZ over the repair region in REPwSTZ-TC reduced the contact area, as compared to REP-TC, by 24% for impermeable loading and by 27% for impermeable loading.

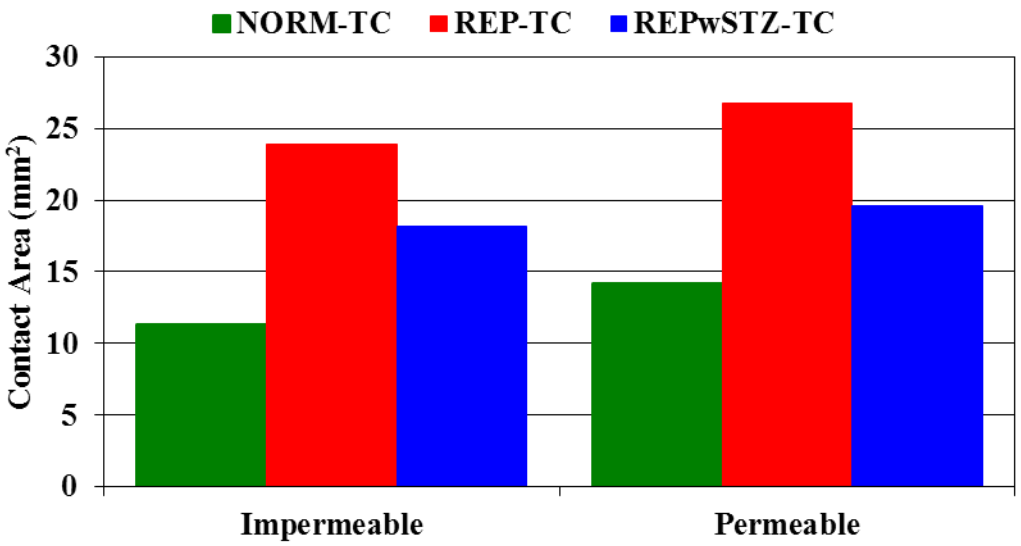

Figure 5.2-1: Area of contact generated for the three models after 30 sec of loading by impermeable and permeable rigid loading surfaces.

Table 5.2-1: Relative changes in parameters of interest after 30 sec are shown between permeable and impermeable loading for each model investigated (NORM-TC, REP-TC, and REPwSTZ-TC)

RATIOS →	PERMEABLE / IMPERMEABLE		
	NORM-TC	REP-TC	REPwSTZ-TC
Contact Area (mm^2)	1.25	1.12	1.08
% Compression - All Zones	1.36	1.40	1.21
% Compression - STZ	3.11	2.32	3.53
% Axial Strain - under STZ	1.86	1.88	1.69
% Radial Strain - under STZ	0.59	0.46	0.70
von Mises Stress - Surface	1.31	2.26	1.28
von Mises Stress - under STZ	0.95	1.40	1.46
Fluid Pressure - under STZ	0.49	0.32	0.67
Fluid Loss Rate - Surface	n/a	n/a	n/a

Table 5.2-2: Relative changes in parameters of interest after 30 sec are shown between each model investigated for both impermeable and permeable loading. Impermeable ratios (IMP) are shown in *italics* and permeable ratios (PER) are shown in **bold** for ease of comparison.

RATIOS →	REP-TC / NORM-TC		REPwSTZ-TC / REP-TC		REPwSTZ-TC / NORM-TC	
	IMP	**PER**	*IMP*	**PER**	*IMP*	**PER**
Contact Area (mm^2)	*2.11*	**1.89**	*0.76*	**0.73**	*1.60*	**1.38**
% Compression - All Zones	*1.63*	**1.68**	*0.82*	**0.71**	*1.34*	**1.20**
% Compression - STZ	*3.25*	**2.42**	*0.19*	**0.29**	*0.62*	**0.71**
% Axial Strain - under STZ	*1.58*	**1.59**	*0.86*	**0.77**	*1.35*	**1.23**
% Radial Strain - under STZ	*3.10*	**2.40**	*0.52*	**0.80**	*1.62*	**1.91**
von Mises Stress - Surface	*0.24*	**0.42**	*4.08*	**2.31**	*0.99*	**0.97**
von Mises Stress - under STZ	*0.33*	**0.49**	*0.75*	**0.78**	*0.25*	**0.38**
Fluid Pressure - under STZ	*0.44*	**0.29**	*1.49*	**3.06**	*0.65*	**0.88**
Fluid Loss Rate - Surface	*n/a*	**1.78**	*n/a*	**0.66**	*n/a*	**1.17**

5.2.2. Full Thickness Axial Compression

Models loaded by the permeable disks experienced 21% to 40% more compression than the same models loaded by the impermeable disk (Figure 5.2-2, Table 5.2-1). REP-TC experienced greater full thickness compression than NORM-TC by 1.6 times for impermeable

loading and by 1.7 times when permeably loaded. Addition of a normal STZ over the repair region in REPwSTZ-TC reduced the full thickness compression, as compared to REP-TC, by 18% for impermeable loading and by 29% for permeable.

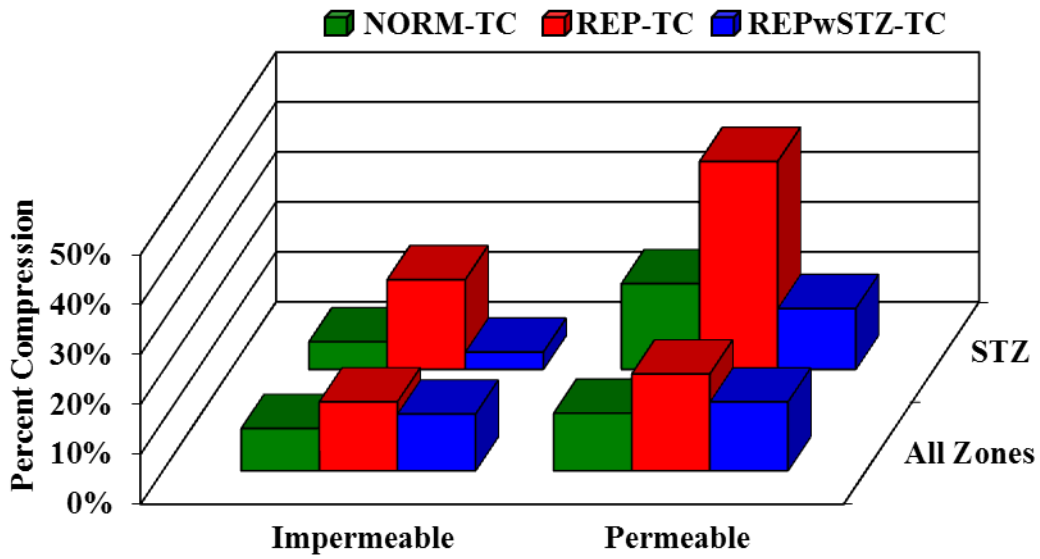

Figure 5.2-2: Compression at centerline of the full thickness (All Zones) and STZ of the three models after 30sec of loading by impermeable and permeable rigid loading surfaces.

5.2.3. STZ Compression

The STZ in models loaded by the permeable disks experienced 2.3 to 3.5 times as much compression as the same models loaded by the impermeable disk (Figure 5.2-2, Table 5.2-1). REP-TC experienced greater compression of the STZ than did NORM-TC by a factor of 3.3 for impermeable loading and 2.4 for permeable loading (Table 5.2-2). Addition of a normal STZ over the repair region in REPwSTZ-TC reduced the full thickness compression, as compared to REP-TC, by 81% for impermeable loading and for permeable loading by 71%.

5.2.4. Axial Strain Beneath the STZ

Compressive axial strain under the STZ region was higher in models loaded by the permeable disks by 1.7 to 1.9 times as much as the same models loaded by the impermeable disk

(Figure 5.2-3, Table 5.2-1). REP-TC experienced greater compressive axial strain beneath the STZ region than did NORM-TC by 1.6 times for impermeable and permeable loading. Addition of a normal STZ over the repair region in REPwSTZ-TC reduced the axial strain in the repair tissue, as compared to REP-TC, by 14% for impermeable loading and by 23% for permeable loading.

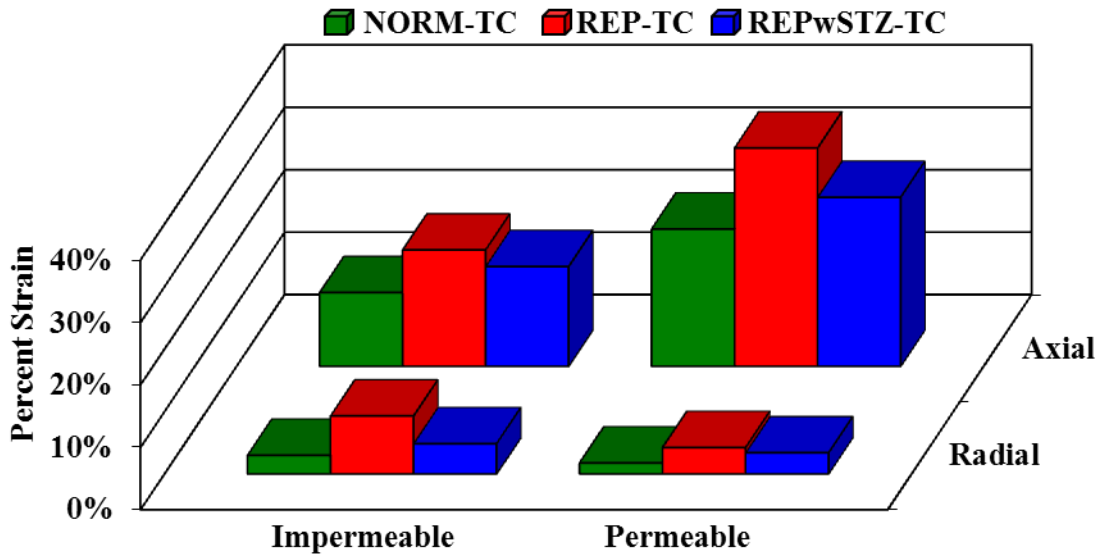

Figure 5.2-3: Percent radial (e11) tensile and axial (e22) compressive strains at centerline of the three models at a point just beneath the STZ region after 30sec of loading by impermeable and permeable rigid loading surfaces.

5.2.5. Radial Strain Beneath the STZ

Radial tensile strains were lower in models loaded by the permeable disks by 30% to 54% as compared to the same models loaded by the impermeable disk (Figure 5.2-3, Table 5.2-1). REP-TC experienced greater radial tensile strain beneath the STZ region than did NORM-TC by a factor of 3.1 for impermeable and 2.4 for permeable loading. Addition of a normal STZ over the repair region in REPwSTZ-TC reduced the radial tensile strain in the repair tissue, as compared to REP-TC, by 48% for impermeable and by 20% for permeable loading.

5.2.6. von Mises Stress

As with the TI models, von Mises stresses for the normal model (NORM-TC) were highest at the center of the articular surface and dispersed through the thickness and radially outward through the cartilage layer for both impermeable and permeable loading (Figure 5.2-4). The contour plot for impermeable loading of NORM-TC shows higher von Mises stress toward the under-side of the STZ; whereas, the permeable contour plot shows a shift of von Mises stresses to the surface. In contrast with TI models, stresses in the central MD/DP region for NORM-TC dispersed more uniformly for both loading surfaces. This is a result of TC properties that are now assigned to this region.

Whether loaded by the impermeable or permeable sphere, von Mises stresses in REP-TC were still very low in the repair tissue central to the cartilage layer and stresses spread radially into more of the surrounding tissues. Still present is an obvious stress gradient in REP-TC's contour plot through the entire cartilage thickness at the interface between the central repair and the surrounding normal tissue, for loading by either sphere. But it is more pronounced and better defined than that seen with the TI models (Figure 4.2-4).

In REPwSTZ-TC, the normal STZ over the repair region resulted in some restoration of von Mises stress at the center of the articular surface and some reduction in stresses experienced by the surrounding normal tissues for impermeable and permeable loading. Further, the von Mises stress gradient at the repair to normal interface in REPwSTZ-TC was attenuated.

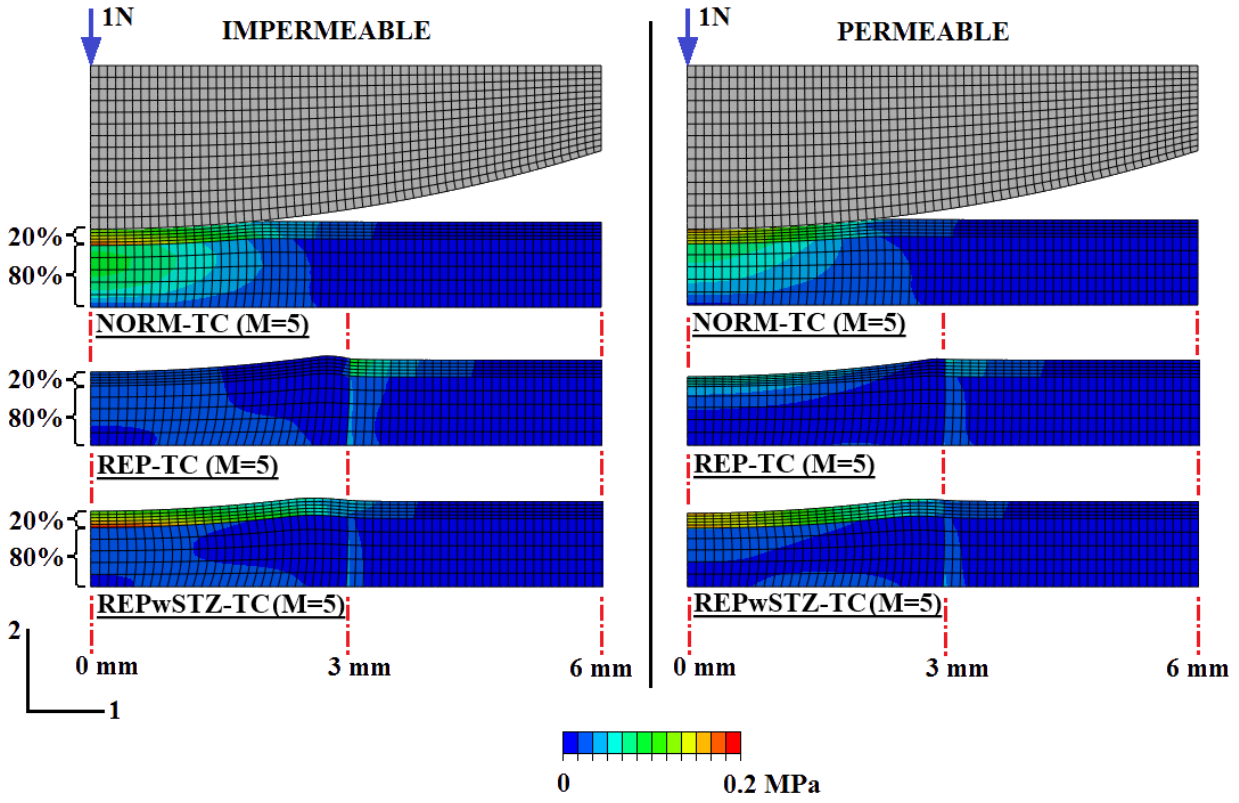

Figure 5.2-4: Contour plots of von Mises stress in the cartilage layers of the three models after 30 sec of loading by relatively rigid impermeable and permeable loading surfaces. The loading surfaces are shown on NORM-TC only for illustrative purposes.

On the surface, von Mises stresses were higher for permeably loaded models by 1.3 to 2.3 times that of the same models loaded by the impermeable disk (Figure 5.2-5, Table 5.2-1). REP-TC's surface experienced less von Mises stress than did NORM-TC by 76% for impermeable and by 58% for permeable loading (Table 5.2-2). Addition of a normal STZ over the repair region in REPwSTZ-TC increased the surface von Mises stress, as compared to REP-TC, by a factor of 4.1 for impermeable and 2.3 for permeable loading.

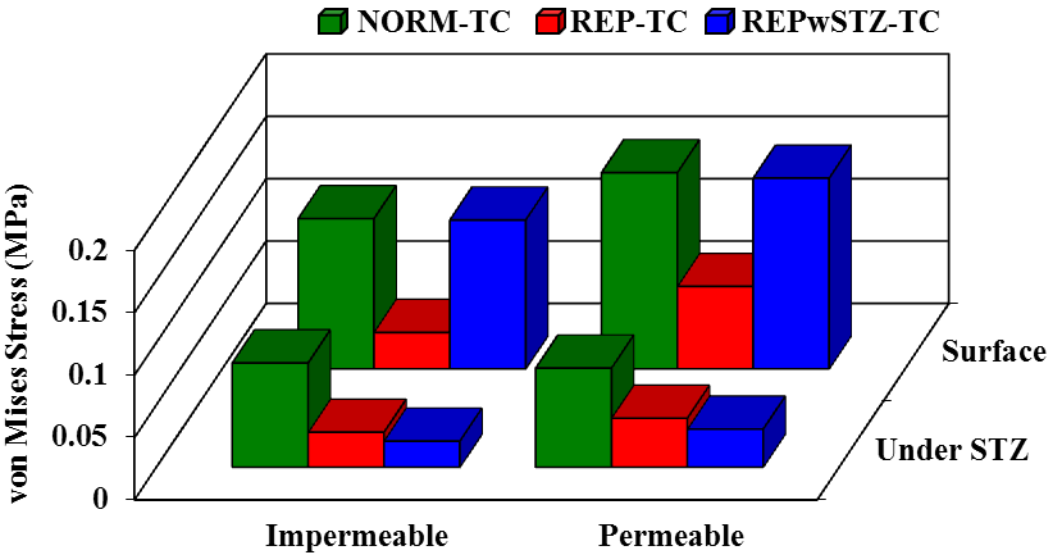

Figure 5.2-5: von Mises stress at centerline of the three models on the articular surface and at a point just beneath the STZ region after 30sec of loading by impermeable and permeable rigid loading surfaces.

Just under the STZ, at the model centers, von Mises stresses for NORM-TC were lower for permeably loaded models by 5% as when loaded by the impermeable disk (Figure 5.2-5, Table 5.2-1). In contrast, the permeable disk resulted in higher von Mises stress under the STZ than when impermeably loaded by 40% for REP-TC and 46% for REPwSTZ-TC. REP-TC experienced less von Mises stress than did NORM-TC under the STZ region by 67% for impermeable loading and by 51% for permeable loading (Table 5.2-2). Addition of a normal STZ over the repair region in REPwSTZ-TC decreased the von Mises stress under the STZ, as compared to REP-TC, by 25% for impermeable loading and by 22% for permeable loading.

5.2.7. Fluid Pressure

Pore fluid pressure contour plots for the TC models are comparable to the TI models (Figure 4.2-6). Pore fluid pressure was highest in the center of the TC models and decreased radially, for both impermeable and permeable loading (Figure 5.2-6). For impermeable loading, fluid flow out of the surface in the contact region was restricted; thus, fluid pressure varied little

through the thickness of the cartilage layers at any point. For permeable loading, pressure varied through the thickness since by definition the pressure was zero everywhere on the surface and fluid was allowed to freely flow from the entire surface.

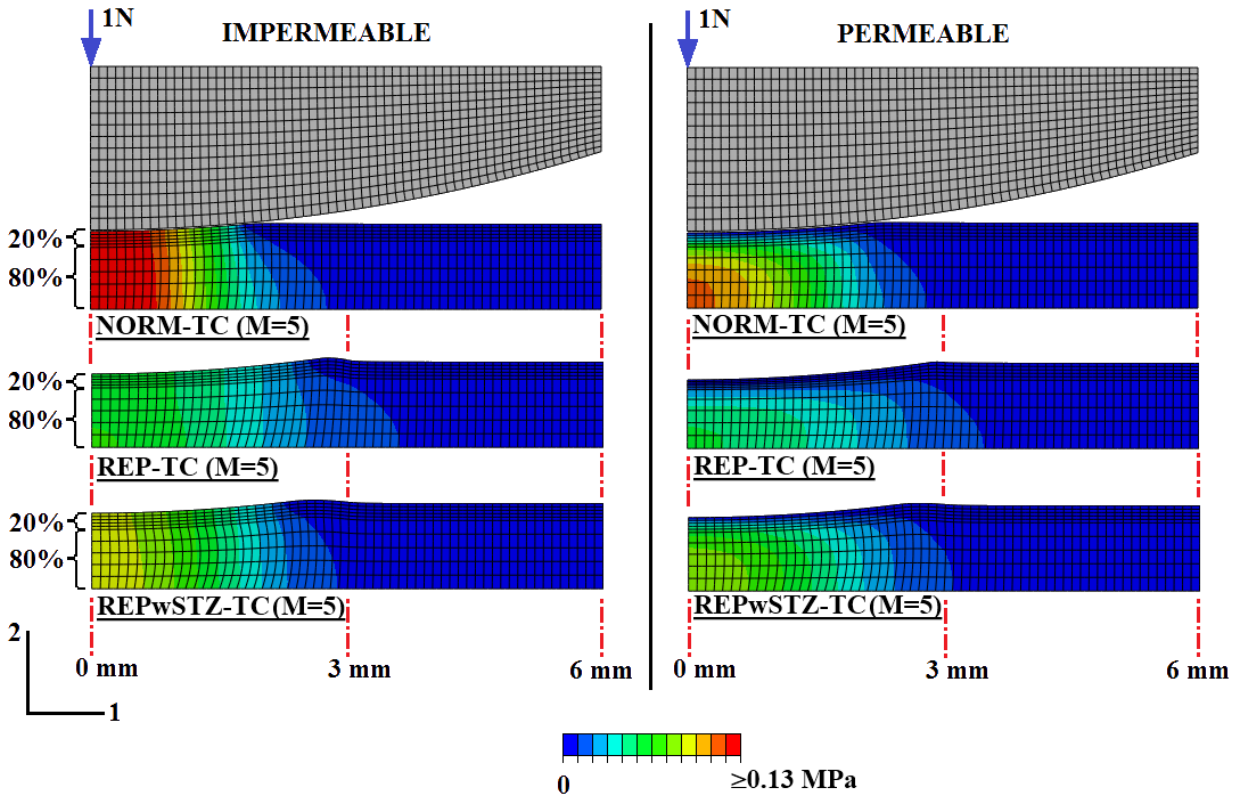

Figure 5.2-6: Contour plots of pore fluid pressure in the cartilage layers of the three models after 30 sec of loading by relatively rigid impermeable and permeable loading surfaces. The loading surfaces are shown on NORM-TC only for illustrative purposes.

Immediately beneath the STZ, at the model centers, fluid pressure was lower for permeably loaded models by 33% to 68% compared to the same models loaded by the impermeable disk (Figure 5.2-7, Table 5.2-1). REP-TC experienced lower fluid pressure under the STZ than did NORM-TC by 56% for impermeable loading and by 71% for permeable loading. Addition of a normal STZ over the repair region in REPwSTZ-TC increased the fluid pressure under the STZ, as compared to REP-TC, by a factor of 1.5 for impermeable loading and by 3.1 for permeable loading.

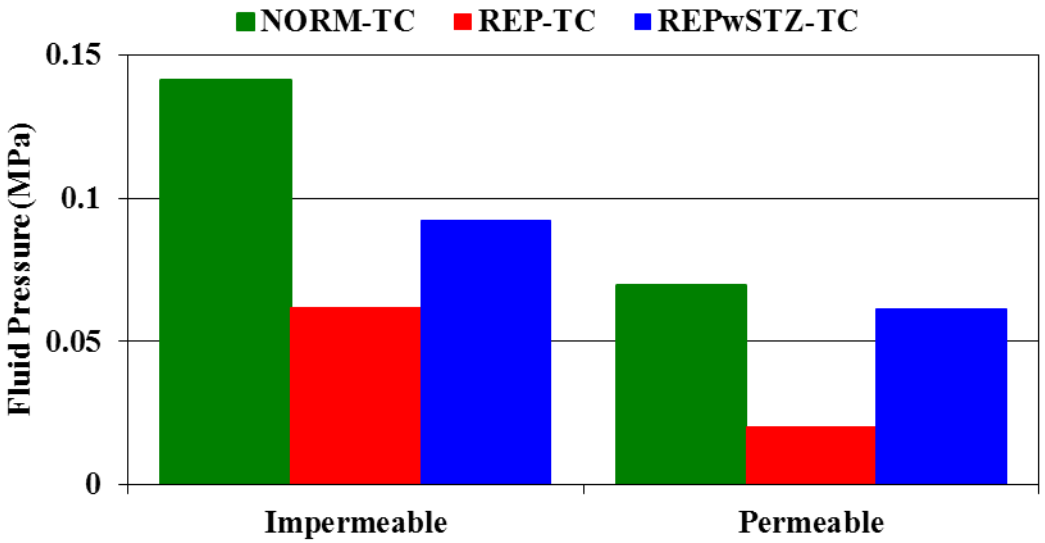

Figure 5.2-7: Fluid pressure at centerline of the three models at a point just beneath the STZ region after 30sec of loading by impermeable and permeable rigid loading surfaces.

5.2.8. Rate of Fluid Loss

After 30sec of loading, fluid flow for permeable loaded models was axially directed and highest at the surface (Figure 5.2-8). Fluid flow for impermeably loaded models was more radially directed and of greater magnitude deeper into the tissue as compared to permeable loading. For both impermeable and permeable loading, fluid flow patterns and magnitudes in REP deviated greatly from NORM-TC. Restoration of the normal patterns and magnitudes were approached in REPwSTZ-TC (Figure 5.2-9).

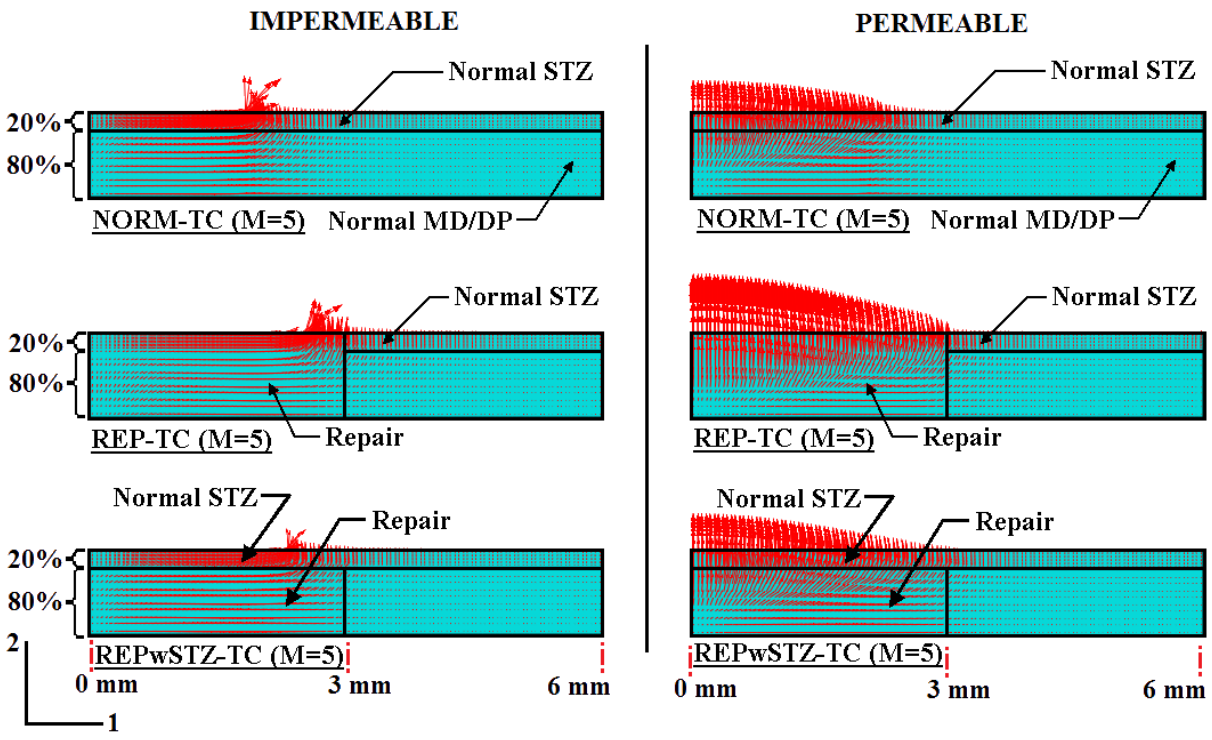

Figure 5.2-8: Effective fluid velocity gradient distributions after 30 sec of loading by relatively rigid impermeable and permeable loading surfaces superimposed on undeformed representations of cartilage layers for the three models. Only the central 6mm is shown in order to magnify the flow patterns; flow beyond 6mm was minimal. Areas of different material behavior are outlined. The loading surfaces are not shown.

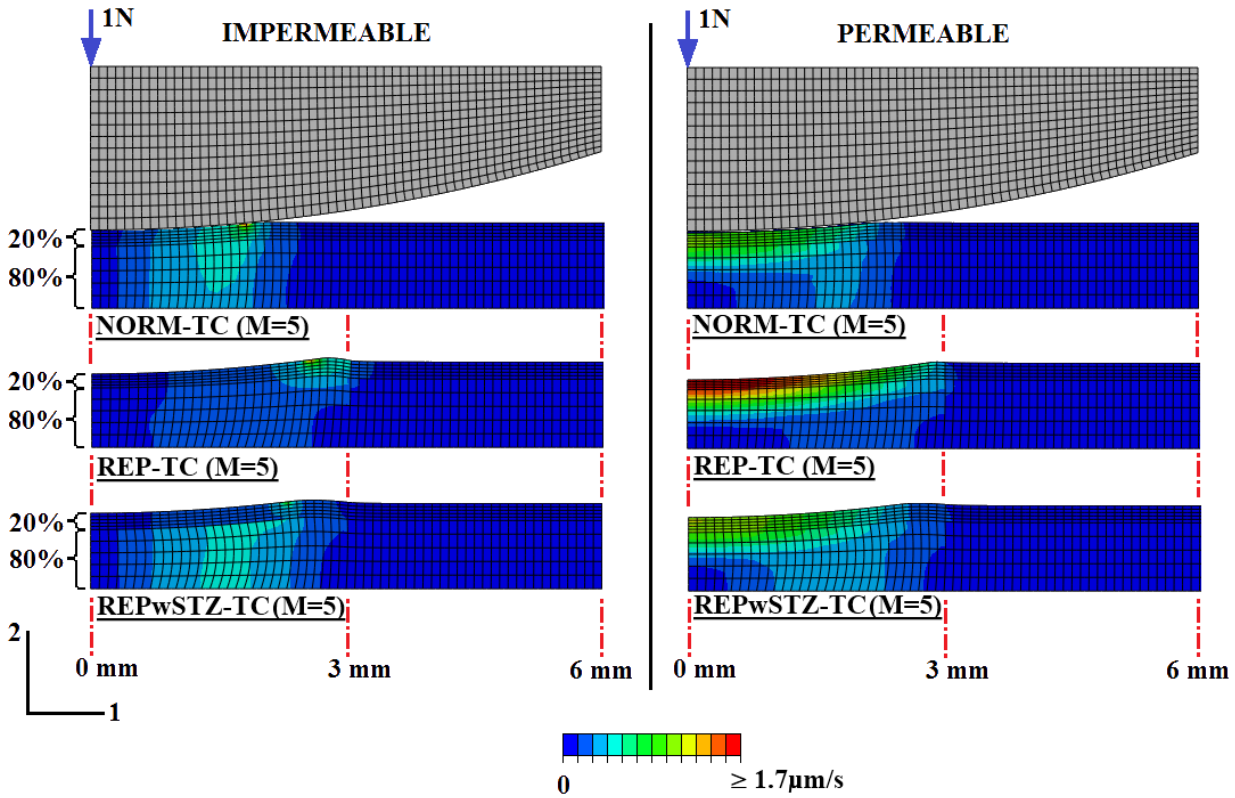

Figure 5.2-9: Contour plots of effective fluid velocity magnitudes in the cartilage layers of the three models after 30 sec of loading by relatively rigid impermeable and permeable loading surfaces. The loading surfaces are shown on NORM-TC only for illustrative purposes.

5.2.9. Tension-Compression Nonlinearity versus Transverse Isotropy

The changes in material definitions for the normal STZ and MD/DP tissues, and the inclusion of nonlinear geometry, generated some appreciable differences between the TC models reported above and the TI models covered in the last chapter. A one-to-one comparison between the TC and TI results highlights those differences (Table 5.2-3). While differences are apparent, consistent patterns are not as clear; likely because of the combined effect of nonlinear geometry and tension-compression nonlinearity. Nonlinear geometry has the effect of causing smaller deformations for a given compressive load and larger deformations for a given tensile load. This can explain, for example, less compression of the STZ occurring for NORM-TC and REP-TC models. However, this pattern did not continue for REPwSTZ-TC perhaps because of the

additional effect of tension-compression nonlinearity in the MD/DP zone which provides greater resistance to radially expanding strains and influences stress states in the rest of the model. Contour plots indicate a higher stress state in the bottom edge of the STZ for REPwSTZ-TC (Figure 5.2-4) than for REPwSTZ-TI (Figure 4.2-4) likely causing the higher deformation in the STZ of REPwSTZ-TC.

Table 5.2-3: Percentage differences in parameters of interest between TI models (NORM-TI, REP-TI, and REPwSTZ-TI) from chapter 4 and TC models (NORM-TC, REP-TC, and REPwSTZ-TC) reported here after 30 sec of loading as predicted for impermeable (IMP) and permeable (PER) contact loading. Differences for impermeably loaded models are shown in *italics* and permeable are shown in **bold** for ease of comparison. A positive number means that TI predicted a value greater than TC.

	NORM		**REP**		**REPwSTZ**	
	IMP	**PER**	*IMP*	**PER**	*IMP*	**PER**
Contact Area (mm^2)	*-0.4%*	**-3.2%**	*6.8%*	**1.6%**	*-0.3%*	**-0.2%**
% Compression - All Zones	*-2.9%*	**-6.4%**	*4.3%*	**3.5%**	*1.1%*	**0.8%**
% Compression - STZ	*47.7%*	**20.6%**	*15.8%*	**19.8%**	*-17.9%*	**0.4%**
% Axial Strain - under STZ	*-25.1%*	**-42.3%**	*0.3%*	**-23.6%**	*-7.9%*	**-10.6%**
% Radial Strain - under STZ	*4.2%*	**12.6%**	*-0.2%*	**43.4%**	*-9.5%*	**-2.3%**
von Mises Stress - Surface	*8.2%*	**8.6%**	*9.1%*	**5.6%**	*-13.5%*	**-8.4%**
von Mises Stress - under STZ	*-34.2%*	**-14.9%**	*0.2%*	**-16.3%**	*-8.2%*	**-9.7%**
Fluid Pressure - under STZ	*-8.9%*	**2.6%**	*-9.4%*	**53.8%**	*0.8%*	**4.5%**
Fluid Loss Rate - Surface	*n/a*	**-23.9%**	*n/a*	**-2.4%**	*n/a*	**-10.0%**

5.3. SUMMARY

Improvements were made to the TI models presented in the previous chapter and reported here. Those improvements involved replacement of transversely isotropic material behavior in the normal STZ with a bilinearly elastic tension-compression definition. Also, the behavior of the normal MD/DP zones, modeled in previous chapters as isotropic, was replaced with a bilinearly elastic tension-compression definition. In addition to the improvements in material definitions, the effect of finite deformation included. All other aspects of the models remained the same.

The results with these changes were comparable to those of the previous chapter in overall conclusions. The full thickness repair (REP-TC) still did not perform as well as the normal model (NORM-TC) under load. As before, REP-TC's solid matrix developed lower stresses while suffering greater strains and overall deformations reflecting the reduced ability of its' solid matrix to support loads. Lower fluid pressures in REP-TC indicated greater fluid loss and highlighted its' reduced ability to retain fluids. The placement of a normal STZ over the repair region in REPwSTZ-TC improved these outcomes, though not totally to the level of the normal model. Appreciable differences were evident between the more realistic models presented in this chapter and those of the previous chapter. Features incorporated in the TC models are more realistic suggesting that more accurate predictions can result from these models. Additionally, contour plots of parameters such as von Mises stress (Figure 5.2-4) showed better definition throughout suggesting that the more realistic approximation may allow better information for future investigations (e.g. repair/normal tissue interface).

5.4. LIMITATIONS

The contact models in this chapter, though advanced in capabilities as compared to those previously reported, still do not address all of the limitations outlined in chapter 3. Models that simulate contact loading between two deformable articular surfaces such that changes in contact area and flow between those surfaces are allowed, still need to be developed. This will be addressed in the next chapter.

6. CURVED LAYERS – RIGID AND NORMAL CONTACT

6.1. OVERVIEW

The flat models that were required with the transversely isotropic approach are not a requirement with the TC material definitions developed in the last chapter. Results presented in this section are thus based on curved models that more closely approximate normal joint geometry (Figure 2.5-4). Material properties are identical to the last chapter using the same bilinearly elastic tension-compression properties for the normal STZ and MD/DP cartilage, and isotropic linearly elastic material definitions for the inferior repair tissue. As before, a strain-dependent permeability mid-range value (M=5) was used to simulate the benefit normally found in cartilage. Abaqus' nonlinear geometry feature (NLGEOM) was again used to account for finite deformation. Curved rigid impermeable and permeable loading surfaces were used with the same boundary conditions as before with the flat models. Loading by a third curved layer was added in this chapter with its geometry identical to the rigid layers but defined as a normal cartilage layer. It's material properties were defined using the same TC properties for its STZ and MD/DP region as used in the normal loaded layer. Given the greater degree of congruency with the curved layers, the applied load was raised to 5N. Loading was maintained until equilibrium to evaluate long-term responses to load, as well as the 30sec short-term point previously used. Results reported here have been published in part [125].

6.2. RESULTS

6.2.1. Contact Area

Throughout the loading time, all models (NORM-TC, REP-TC, and REPwSTZ-TC) loaded by a normal cartilage layer (NORM-TC-TOP) experienced contact areas greater than those loaded by the impermeable (IMP) or permeable (PER) rigid surfaces, with the exception of short-term (after 30sec) loading of REP-TC by PER (Figure 6.2-1, Table 6.2-1). Congruent with previous investigations, REP-TC had the greatest contact area for any loading surface. However, relative changes in contact areas between the models loaded by NORM-TC-TOP were smaller than for those changes when loaded by IMP and PER. For REPwSTZ-TC, as compared to REP-TC, short-term percentage improvements in contact area when loaded with IMP (-7%) and PER (-19%) did not bracket the relative improvement when loaded by NORM-TC-TOP (-2%) (Table 6.2-2).

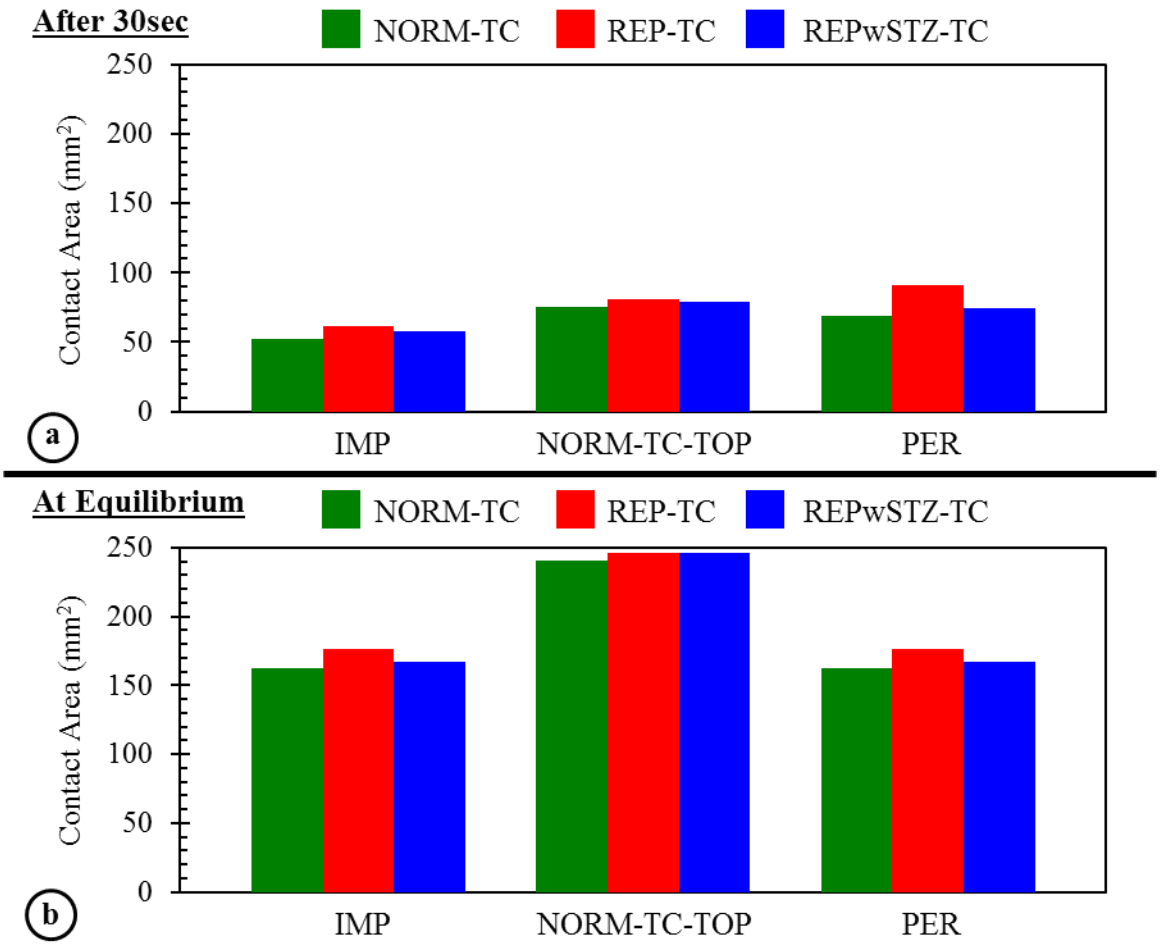

Figure 6.2-1: Areas of contact generated for the three models loaded by rigid impermeable (IMP), normal (NORM-TC-TOP), and rigid permeable (PER) loading surfaces after a) 30sec of loading and b) at equilibrium.

Table 6.2-1: Relative changes between permeable (PER), normal (NORM-TC-TOP here abbreviated as NRM), and impermeable (IMP) loading surfaces after 30 sec for each model investigated (NORM-TC, REP-TC, and REPwSTZ-TC) tabulated by parameters of interest.

RATIOS →	NORM-TC			REP-TC			REPwSTZ-TC		
	PER / *IMP*	NRM / *IMP*	NRM / **PER**	**PER** / *IMP*	NRM / *IMP*	NRM / **PER**	**PER** / *IMP*	NRM / *IMP*	NRM / **PER**
Contact Area (mm^2)	1.34	1.46	1.09	1.47	1.31	0.89	1.29	1.38	1.07
% Compression - All Zones	1.41	0.62	0.44	1.62	0.86	0.53	1.35	0.78	0.58
% Compression - STZ	4.00	0.62	0.16	4.32	0.88	0.20	5.14	0.75	0.15
% Axial Strain - under STZ	2.05	0.63	0.31	2.72	0.86	0.32	2.21	0.77	0.35
% Radial Strain - under STZ	0.59	0.66	1.12	0.08	0.85	10.33	0.67	0.79	1.18
von Mises Stress - Surface	1.33	0.68	0.51	4.69	0.87	0.19	1.37	0.78	0.57
von Mises Stress - under STZ	0.95	0.65	0.69	1.85	0.86	0.46	1.89	0.77	0.41
Fluid Pressure - under STZ	0.60	0.73	1.21	0.29	0.88	3.00	0.74	0.85	1.15
Fluid Loss Rate - Surface	n/a	n/a	~0	n/a	n/a	~0	n/a	n/a	~0

Table 6.2-2: Relative changes between models investigated (NORM-TC, REP-TC, and REPwSTZ-TC) after 30 sec for the permeable (PER), normal (NORM-TC-TOP here abbreviated as NRM), and impermeable (IMP) loading surfaces tabulated by parameters of interest. Impermeable ratios (*IMP*) are shown in *italics* and permeable ratios (PER) are shown in **bold** for ease of comparison.

RATIOS →	REP-TC / NORM-TC			REPwSTZ-TC / REP-TC			REPwSTZ-TC / NORM-TC		
	IMP	NRM	**PER**	*IMP*	NRM	**PER**	*IMP*	NRM	**PER**
Contact Area (mm^2)	*1.19*	1.07	**1.31**	*0.93*	0.98	**0.81**	*1.11*	1.04	**1.07**
% Compression - All Zones	*1.18*	1.65	**1.35**	*0.93*	0.84	**0.78**	*1.10*	1.39	**1.05**
% Compression - STZ	*1.93*	2.74	**2.09**	*0.30*	0.26	**0.36**	*0.58*	0.70	**0.75**
% Axial Strain - under STZ	*0.98*	1.36	**1.31**	*1.04*	0.93	**0.85**	*1.03*	1.26	**1.11**
% Radial Strain - under STZ	*1.60*	2.04	**0.22**	*0.55*	0.51	**4.48**	*0.88*	1.05	**0.99**
von Mises Stress - Surface	*0.07*	0.09	**0.26**	*11.07*	9.94	**3.23**	*0.82*	0.93	**0.84**
von Mises Stress - under STZ	*0.18*	0.24	**0.35**	*0.88*	0.79	**0.90**	*0.16*	0.19	**0.32**
Fluid Pressure - under STZ	*0.61*	0.74	**0.30**	*1.17*	1.12	**2.92**	*0.71*	0.82	**0.86**
Fluid Loss Rate - Surface	*n/a*	1.09	**1.40**	*n/a*	n/a	**0.72**	*n/a*	n/a	**1.01**

6.2.2. Full Thickness Axial Compression

Throughout the loading period, full thickness deformation (All Zones) at the axis of symmetry for models loaded via NORM-TC-TOP was less than when loaded by IMP and PER (Figure 6.2-2, Table 6.2-1). PER loading generated the largest short-term deformations of all

models and achieved equilibrium the fastest. As would be expected, equilibrium compression was identical for IMP and PER loading because fluid contributions had ceased at that point and the equilibrium state depended solely on material interaction between the rigid surfaces and the models. NORM-TC-TOP loaded models took longer to achieve equilibrium than corresponding models loaded by IMP (11% to 32% greater than) or PER (9.9 to 14.3 greater than). For each loading surface, REP-TC models consistently suffered larger full thickness deformation than NORM-TC models while the full thickness deformation was reduced for REPwSTZ-TC, as compared to REP-TC (Table 6.2-2). Short-term percentage improvements in full thickness axial compression for REPwSTZ-TC, as compared to REP-TC, when loaded with IMP (-7%) and PER (-22%) bracketed the relative improvement when loaded by NORM-TC-TOP (-16%).

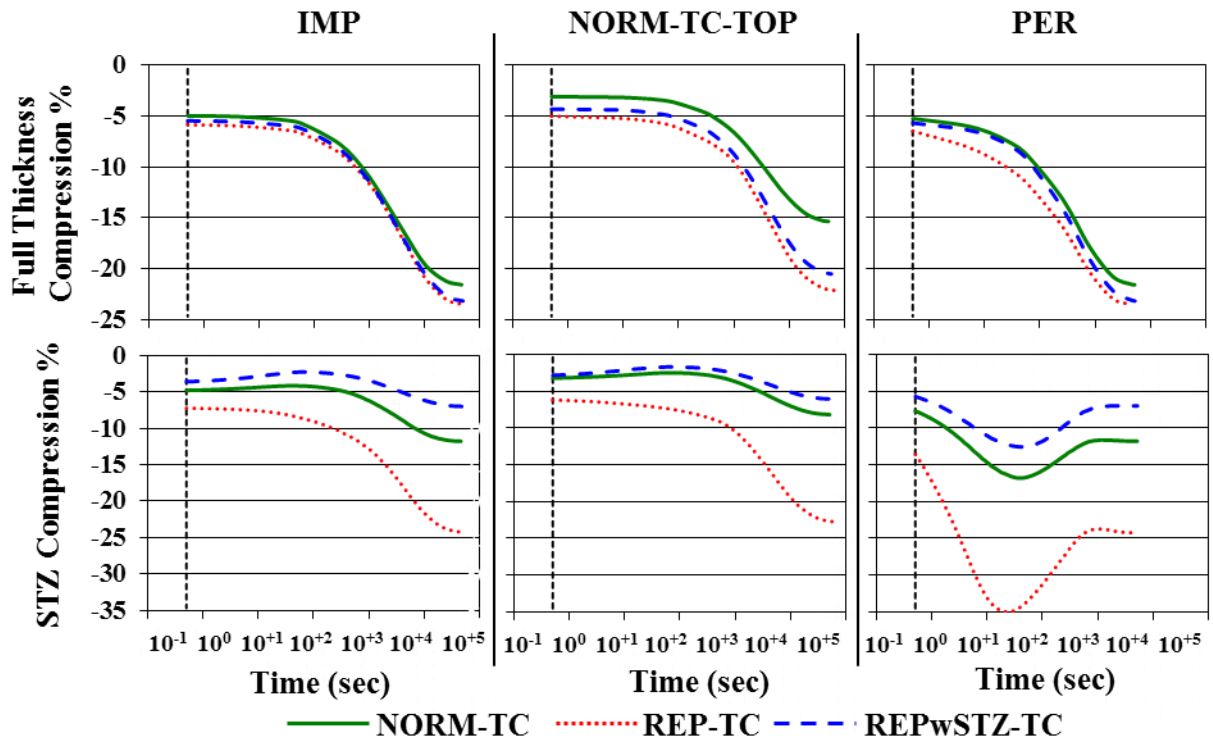

Figure 6.2-2: Compression at centerline of the full thickness (All Zones) and STZ of the three models during loading by rigid impermeable (IMP), normal (NORM-TC-TOP), and rigid permeable (PER) loading surfaces plotted until equilibrium. The dashed vertical lines indicate 0.5 sec of loading at which point 5N of load was fully applied.

6.2.3. STZ Compression

Throughout the loading period, compression of the STZ region (i.e. a normal STZ in NORM-TC and REPwSTZ-TC, while an equivalent region for REP-TC) at the axis of symmetry for models loaded via NORM-TC-TOP was less than when loaded by IMP and PER (Figure 6.2-2, Table 6.2-1). As with full thickness compression, PER loading generated the largest short-term STZ compression of all models and achieved equilibrium the fastest. Interestingly, the STZ for all models loaded by PER experienced short-term compression that was greater than the eventual equilibrium levels; then rebounded and ended at equilibrium values equivalent to IMP loading. For each loading surface, at all times, REP-TC models consistently suffered larger compression of the STZ region than NORM-TC models (Table 6.2-2). Contrary to relative changes seen with full thickness compression, compression of the STZ was reduced for REPwSTZ-TC, as compared to REP-TC and NORM-TC. Short-term percentage improvements in STZ compression for REPwSTZ-TC, as compared to REP-TC, when loaded with IMP (-70%) and PER (-64%) did not bracket the relative improvement when loaded by NORM-TC-TOP (-74%).

6.2.4. von Mises Stress

For loading via IMP, NORM-TC-TOP, and PER, von Mises stresses were higher in the STZ than in the underlying middle/deep tissue when loading the normal layer (NORM-TC) (Figure 6.2-3). An appreciable decrease in stress occurred in the central repair region of REP-TC, as compared to the same area within NORM-TC, throughout its thickness for all loading conditions. Stresses increased in the surrounding normal tissues of the REP-TC model and high stress gradients occurred at the interface between the repair and surrounding normal STZ. For the repair model covered with a normal STZ (REPwSTZ-TC), as compared to REP-TC, stresses

in the surrounding normal tissues overall decreased as a result of higher stresses developed in the central surface region.

Loading by NORM-TC-TOP, as compared to loading by IMP and PER, resulted in lower von Mises stresses on the surface and immediately beneath the STZ at the center of all models (Table 6.2-1). For REPwSTZ-TC as compared to the same location in REP-TC under all loading conditions, increases were seen in von Mises stresses at the center on the surface and reductions were seen in von Mises stress for the repair tissue immediately beneath the STZ. The short-term improvement on the surface for loading by NORM-TC-TOP (9.9 times) fell within the range experienced when loaded by IMP (11.1 times) and PER (3.2 times) rigid surfaces (Table 6.2-2). In contrast, the improvements seen in von Mises stress beneath the STZ when loaded by NORM-TC-TOP (-21%) were greater than the range experienced when loaded by IMP (-12%) and PER (-10%).

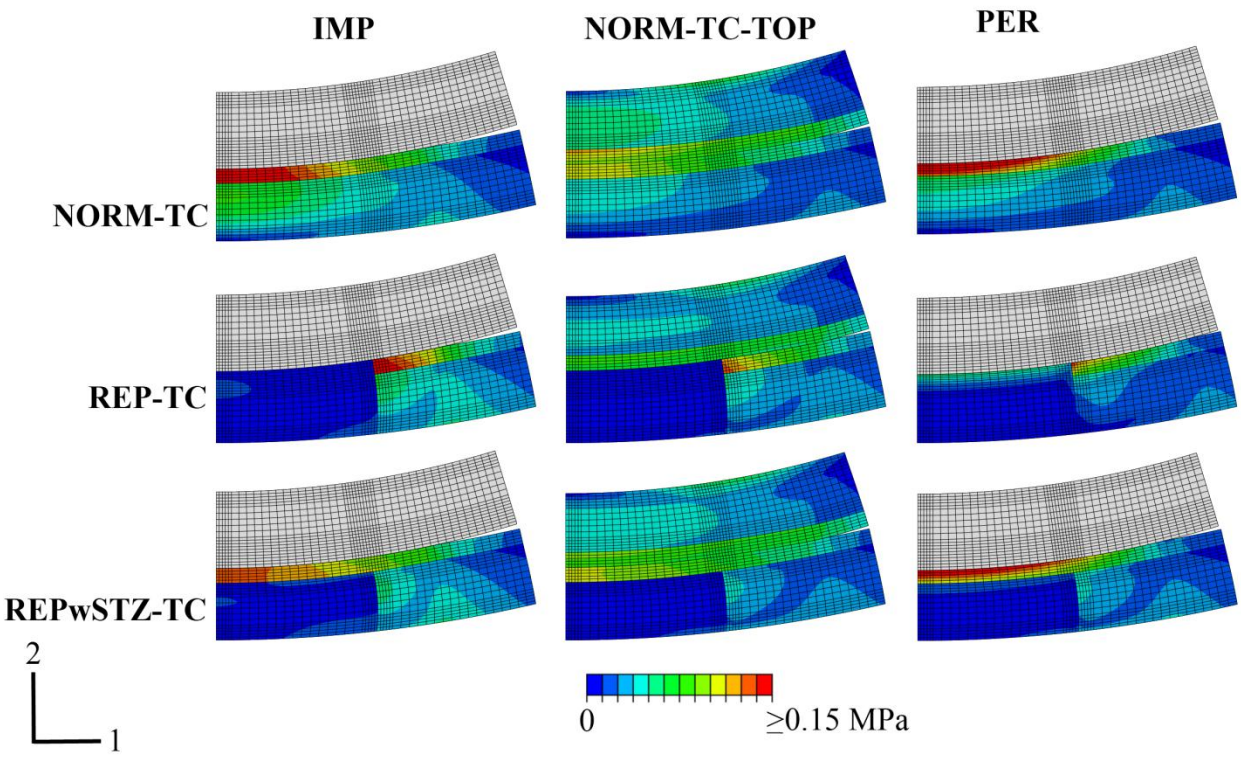

Figure 6.2-3: Contour plots of von Mises stress in the cartilage layers of the three models after 30 sec of loading by rigid impermeable (IMP), normal (NORM-TC-TOP), and rigid permeable (PER) loading surfaces. For magnification, only a central portion of about one-half of each model is shown.

6.2.5. Axial and Radial Stress and Strain

Inferior repair tissues along the centerline of REP-TC and REPwSTZ-TC were unable to develop appreciable radial stresses for any of the loading surfaces (Figure 6.2-4). Accordingly, short-term radial strain levels for REP-TC were elevated relative to NORM-TC for loading via IMP and NORM-TC-TOP, but were significantly lower for loading via PER as a result of faster fluid loss for PER loading (Figure 6.2-5). The normal STZ in REPwSTZ-TC enabled development of higher radial stresses in the STZ. This reduced radial strains under the STZ of REPwSTZ-TC, as compared to REP-TC, for loading via IMP (-45%) and NORM-TC-TOP (-49%) but appreciably raised the radial tensile strains for loading via PER (4.5 times) (Table

6.2-2). As a result of the normal STZ, the radial strain profile along the centerline of REPwSTZ-TC was comparable to those of NORM-TC for all loading surfaces.

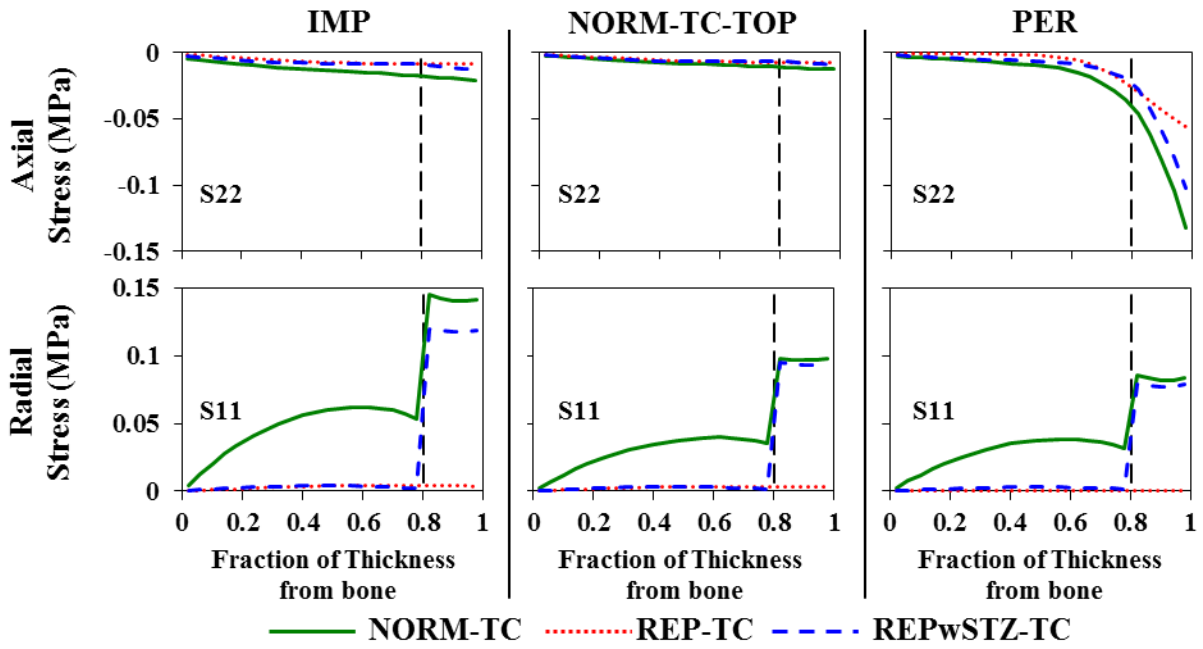

Figure 6.2-4: Axial (S22) and radial (S11) stress along the centerline of the three models after 30 sec of loading by rigid impermeable (IMP), normal (NORM-TC-TOP), and rigid permeable (PER) loading surfaces. The dashed vertical lines demarcate the border between the middle/deep zones and the STZ.

As expected for the extreme condition represented by PER, the top 40% of the centerline of models loaded by PER experienced levels of axial stress and strain that greatly exceeded levels achieved in models loaded by IMP and NORM-TC-TOP. Whereas, axial stress and strain levels for loading via IMP and NORM-TC-TOP were comparable to each other for any loaded surface. Loading of REPwSTZ-TC resulted in axial strain profiles comparable to NORM-TC when loaded via IMP and NORM-TC-TOP. (Figure 6.2-4 and Figure 6.2-5)

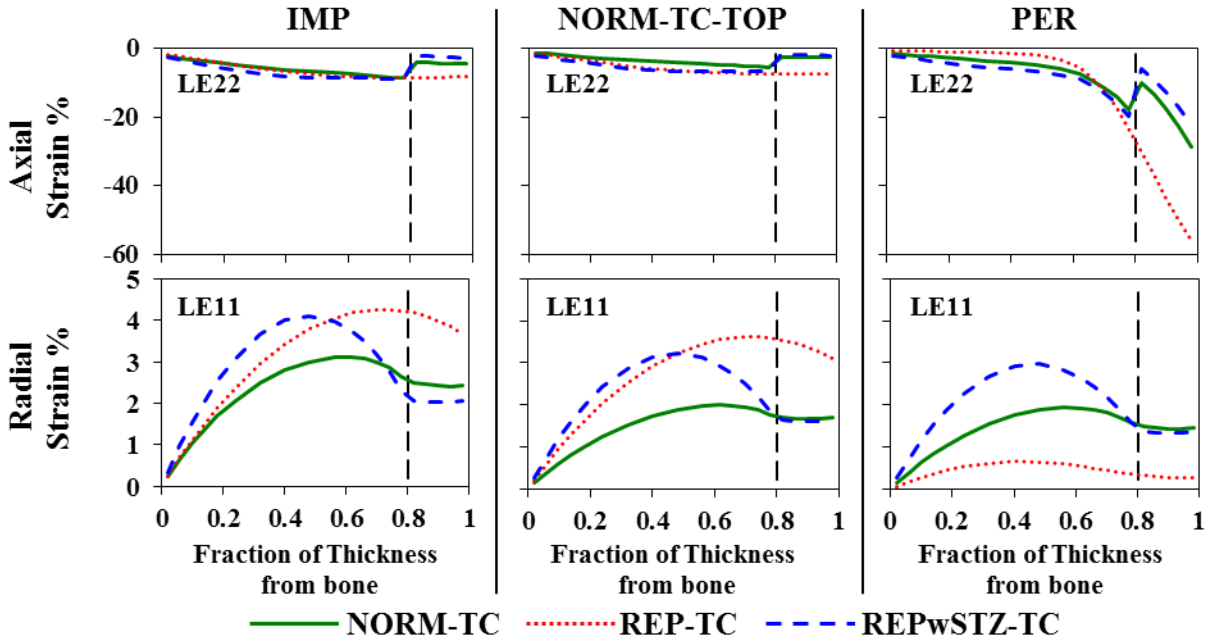

Figure 6.2-5: Percent radial (LE11) tensile and axial (LE22) compressive strains along the centerline of the three models after 30 sec of loading by rigid impermeable (IMP), normal (NORM-TC-TOP), and rigid permeable (PER) loading surfaces. The dashed vertical lines demarcate the border between the middle/deep zones and the STZ.

6.2.6. Shear Stresses

For loading via IMP, NORM-TC-TOP, and PER, shear stresses were highest at the cartilage/bone interface (Figure 6.2-6). Shear stresses were also observed to increase on the surface of models loaded via PER. However, maximum shear stresses were very low, on the order of 20 kPa, throughout all models.

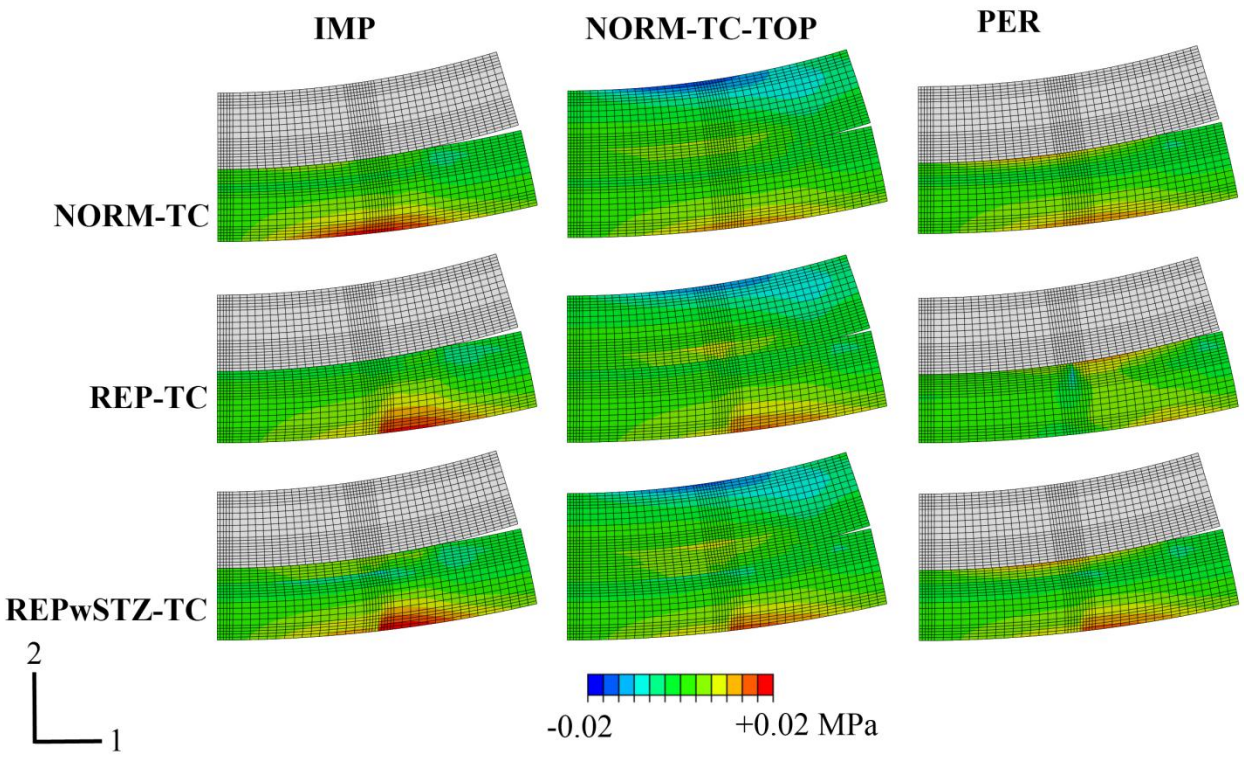

Figure 6.2-6: Contour plots of shear stress (S12) in the cartilage layers of the three models after 30 sec of loading by rigid impermeable (IMP), normal (NORM-TC-TOP), and rigid permeable (PER) loading surfaces. For magnification, only a central portion of about one-half of each model is shown.

6.2.7. Fluid Pressure

For loading via IMP, NORM-TC-TOP, and PER, pore fluid pressure was reduced for REP-TC, as compared to NORM-TC. This is reflective of a fluid loss from REP-TC that is greater than NORM-TC. For REPwSTZ-TC as compared to REP-TC, there was improvement in fluid pressurization and thus some reduction in fluid loss for all loading surfaces (Figure 6.2-7). After 30sec of loading, increases were seen in pore fluid pressure of repair tissue immediately beneath the STZ for REPwSTZ-TC, as compared to the same location in REP-TC, for all loading surfaces as follows: IMP (17%), NORM-TC-TOP (12%), and PER (2.9 times) (Figure 6.2-8, Table 6.2-2). Thus, the improvements in pore fluid pressure for NORM-TC-TOP were less than the range predicted by rigid surface loading.

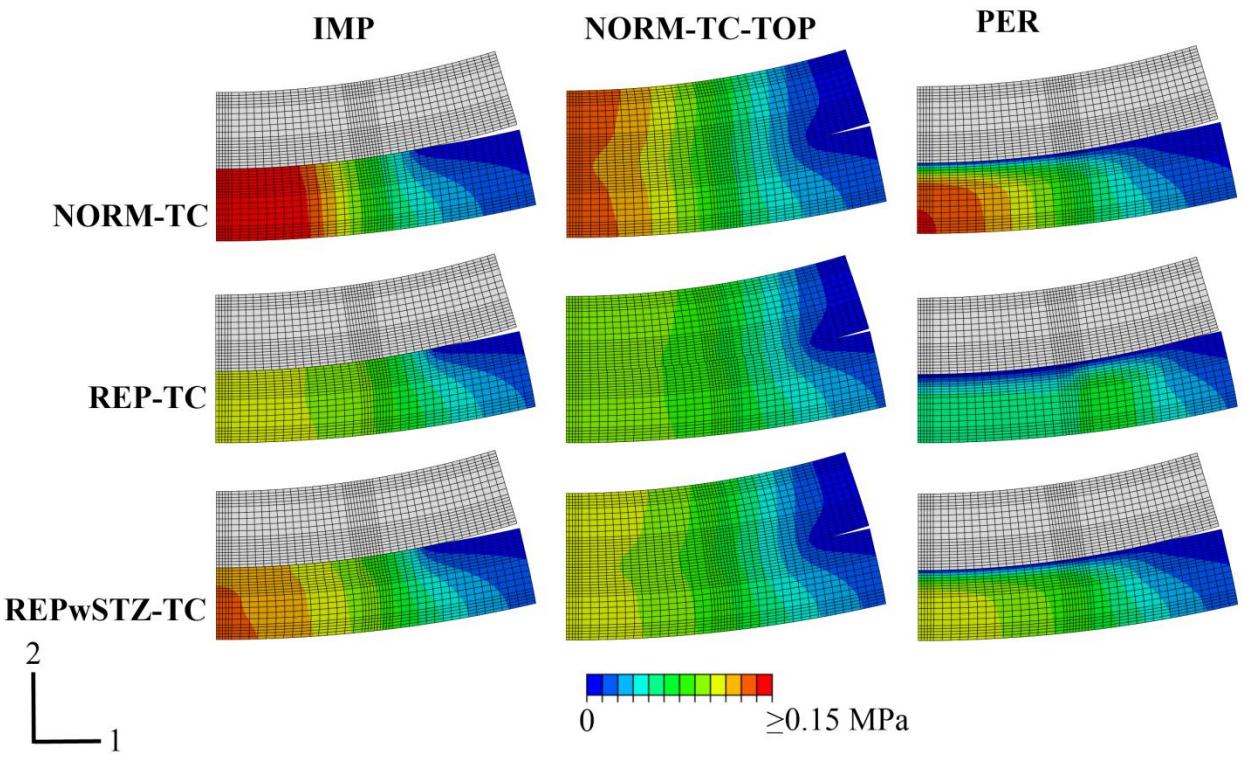

Figure 6.2-7: Contour plots of pore fluid pressure in the cartilage layers of the three models after 30 sec of loading by rigid impermeable (IMP), normal (NORM-TC-TOP), and rigid permeable (PER) loading surfaces. For magnification, only a central portion of about one-half of each model is shown.

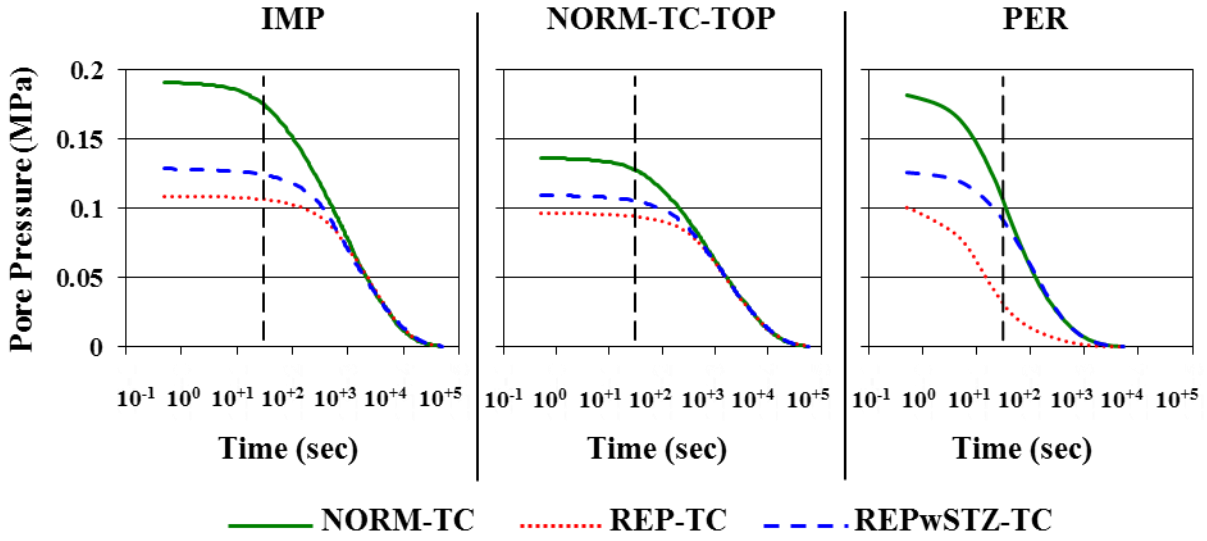

Figure 6.2-8: Fluid pressure at the centerline of the three models at a point just beneath the STZ region when loaded over time by rigid impermeable (IMP), normal (NORM-TC-TOP), and rigid permeable (PER) loading surfaces. The dashed vertical lines indicate 30 sec of loading.

6.2.8. Rate of Fluid Loss

For loading via IMP and NORM-TC-TOP, effective fluid flow within REP-TC was appreciably altered as compared to NORM-TC (Figure 6.2-9). Covering the repair with a normal STZ in REPwSTZ-TC shifted the flow pattern back toward that of NORM-TC. By definition, no flow was allowed from the contact region of models loaded by IMP. For models loaded by NORM-TC-TOP, flow from the contact region was three orders of magnitude smaller than for loading by PER and thus negligible. When loading via PER, effective fluid flow reveals a dramatic exit of fluid from the loaded surfaces (Figure 6.2-10).

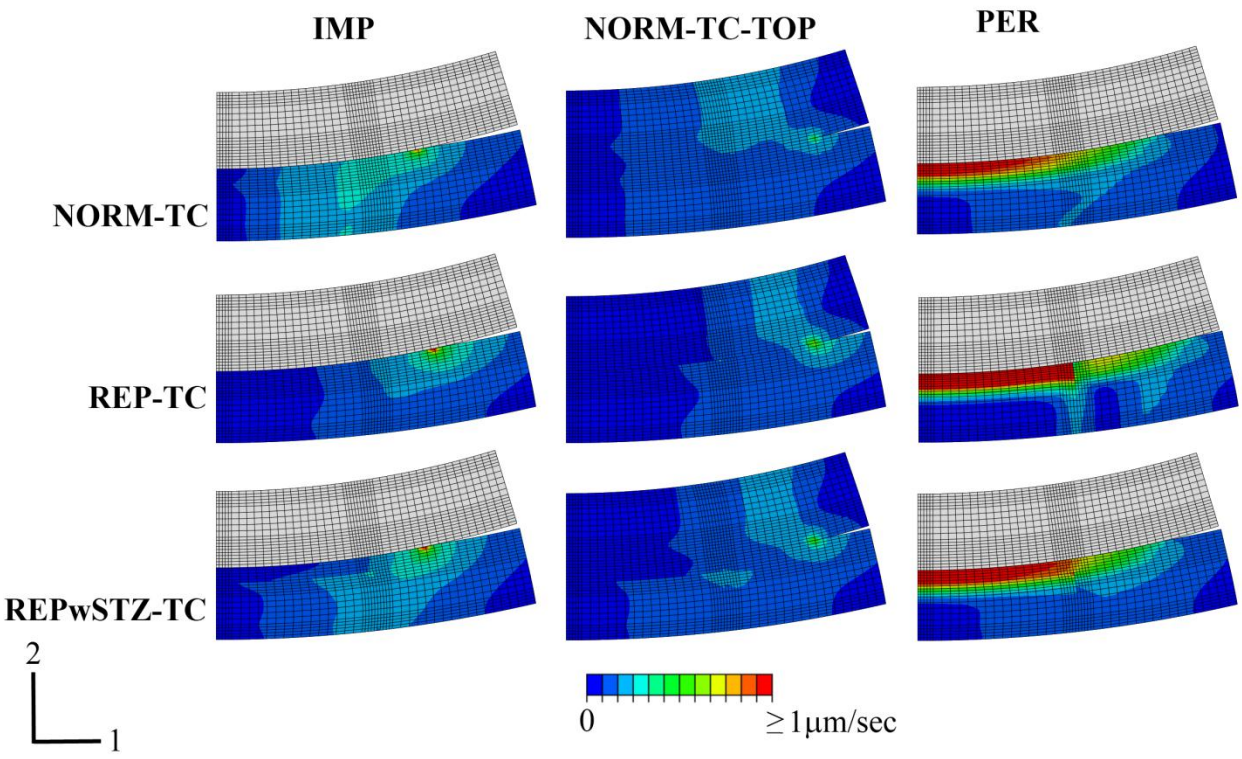

Figure 6.2-9: Contour plots of effective fluid velocity magnitudes in the cartilage layers of the three models after 30 sec of loading by rigid impermeable (IMP), normal (NORM-TC-TOP), and rigid permeable (PER) loading surfaces. For magnification, only a central portion of about one-half of each model is shown.

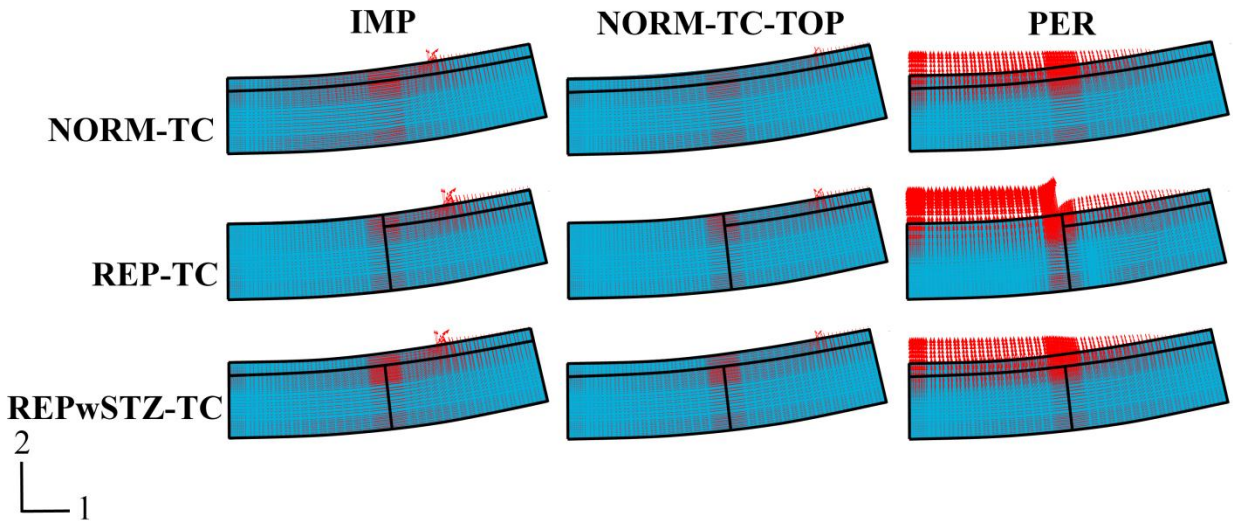

Figure 6.2-10: Effective fluid velocity gradient distributions after 30 sec of loading in the cartilage layers of the three models after 30 sec of loading by rigid impermeable (IMP), normal (NORM-TC-TOP), and rigid permeable (PER) loading surfaces. For magnification, only a central portion of about one-half of each model is shown. To facilitate display of fluid flow out of the models the loading surfaces are not shown and the plots are undeformed.

6.3. SUMMARY

This chapter took advantage of flexibility afforded by the previously developed TC material definition to investigate curved models that more closely approximated normal joint geometry. Additionally, the ability to load the models by another cartilage layer was added. In general, directional changes between models were comparable to findings in previous chapters. That is to simply say that the full thickness repair (REP-TC) still did not perform as well as the normal model (NORM-TC) under load, while adding a normal STZ over the repair (REPwSTZ-TC) improved performance though not to the level of the normal model. However, the ability to load the models with a normal cartilage layer revealed that the magnitude of these differences fell outside of the range predicted by the simpler rigidly loaded models for several parameters. The suggestion is that the more sophisticated models presented in this chapter can provide more realistic predictions concerning the response of repair scenarios in actual joints.

6.4. LIMITATIONS

While this chapter continues to suggest that transplanted material with a quality STZ may be critical in achieving the long-term survival of repairing cartilage, it also highlights the need for models that more closely mimic in vivo conditions. While significant improvements have been incorporated in this work, additional features can be added to make the models more precise in their predictions. Greater levels of model sophistication can provide needed guidance in identifying features critical to engineered tissues surviving the healing process and achieving normal functional characteristics of articular cartilage. Future models can be enhanced to add further levels of material anisotropy. Simulation of incomplete integration between implanted and surrounding tissues can be useful. Also, the addition of other joint soft tissue components can be helpful.

7. DISCUSSION AND CONCLUSIONS

The response of articular cartilage to load is affected by numerous factors. Its compositional makeup (e.g. proteoglycans, collagen types, water, etc.), integrity of connections between the physical components, and the electrochemical interaction of those components work together to enable articular cartilage to support the significant loads to which it is regularly subjected. Its' ability to do this in a nearly frictionless manner for decades is astounding. However, the avascular, aneural, and anerobic environment in which chondrocytic cells exist make it difficult for cartilage to successfully survive injury or disease. Various repair approaches have been developed over the years in an effort to foster healing, but with limited success. While efforts to create repair tissues have become more sophisticated, resulting in better outcomes, the goal of achieving normal zonal properties in vitro or in vivo has not yet been achieved [31,41-44].

Functional tissue engineering seeks to replicate critical features of normal cartilage in tissue engineered constructs with the hopes of improving the chances of those replacement tissues functioning adequately in their intended applications [38-40]. Factors important in achieving normal function are complex and interactive [126,127], with mechanical features being one subset. Various mechanical behaviors are involved in normal cartilage function such as compressive resistance, permeability, dynamic response, low friction resistance, degree of anisotropy, etc. Much discussion still exists as to which physical features are most critical for inclusion in tissue constructs, and consequently, the quality of these physical characteristics that is necessary to be functional. Certainly, chemical composition of engineered cartilage constructs both in

proteoglycan and collagen contents, as well as type, is important in achieving mechanical behavior critical to survival. Also, the manner in which these elements are assembled in constructs can affect behavior, such as anisotropic collagen organization for directional tensile stiffness. Intuition suggests that the best replacement tissue would be that which exactly replicates all normal properties. Thus researchers are trying to develop scaffolds which contain material anisotropies similar to normal cartilage from the outset [42,128-130]. However, it is very unlikely that an exact replication would ever be achieved prior to implantation and maturation. In reality, it appears that the best one can hope for is to achieve some of the normal properties. Some have even suggested that properties other than normal may be needed initially for replacement tissues to survive the healing process, integrate with surrounding tissues, and to become functionally normal [48,49]. Guidance is needed as to which properties, if incorporated, would best improve performance of engineered tissues.

Inclusion of STZ-like properties is one feature that should provide significant benefits. A normal STZ is distinguished from other cartilage zones by its closely packed, tangentially oriented collagen fibrils and reduced proteoglycan content. These combined qualities of the STZ have been shown to result in a high resistance to fluid flow, at both the outset of loading because of tight fibril spacing and over time as the zone compresses. This causes permeability within the STZ to reduce exponentially with increasing volumetric strain [19,131]. Previous experimental studies have shown the importance of the STZ in normal cartilage function [45-47]. Removal of the STZ caused increased deformations in tissue samples subjected to axial compressive loads and fluid loss from these surfaces increased.

Finite element methods have tremendous potential for identifying features that tissue engineers may want to incorporate in their scaffold designs. Regarding the STZ, finite element

methods have mirrored conclusions of in vitro studies by predicting excessive axial deformation of repair cartilage without the STZ [106,116]. However, prior to the work presented here, no study had investigated potential benefits of including STZ-like properties in engineered tissues. Thus, the finite element models developed in this thesis focused on the effect that a normal STZ can have as a protective covering over repair tissue.

Repair models with and without a protective STZ, as well as normal models, were developed in a manner that incrementally added levels of improvements beginning with simple 2D axi-symmetric representations of a flat articular surface loaded by a constant parabolic pressure distribution, proceeding to flat models loaded by permeable and impermeable rigid surfaces, and culminating in contact loading of curved models by permeable and impermeable rigid surfaces and by another normal cartilage layer. In the initial flat models, the STZ was modeled as transversely isotropic to approximate higher tensile stiffness afforded by collagen organization. Normal middle and deep zones, as well as repair tissues, were modeled as linearly elastic isotropic. In later flat and curved models normal tissues were defined as bilinearly elastic to better reflect higher tensile stiffness in the STZ and to add a lesser contribution of this tension-compression nonlinearity in the middle and deep zones. Repair tissue definitions remained as isotropic.

Permeability in the STZ was defined as exponentially dependent on volumetric strain defined by a linear expression versus a logarithmic relationship used by others [132,133]. The resulting permeability is comparable at small strains but its reduction is underestimated for large strains. Thus, the logarithmic relationship would have predicted similar or even less fluid loss for the model configurations investigated here, and therefore the overall conclusions of this work would remain the same. In all models, constant permeability was defined for repair tissues and

for normal middle and deep zones while strain-dependent permeability was defined in the normal STZ only. While normal middle and deep zone tissues may also exhibit strain dependent permeability [23,24], this would have had little effect here as the small strain occurring in the normal middle/deep zones surrounding repair tissues would not have substantially altered the permeability. Further, permeability has been found to either decrease [23] or remain relatively unchanged [19,24] with depth from the articular surface. For our models, all normal tissues were assigned the same initial permeability; while repair tissue permeability was nearly double that of normal tissues to simulate mechanically inferior repair tissues. Lastly, a range of strain-dependent permeability values was investigated in the early flat models loaded by the parabolic pressure distribution and by rigid contact to determine the effect of increasing dependency of permeability on volumetric strain. Once this effect was established, the normal STZ in subsequent flat and curved models was defined at one level of strain-dependency representing the mid-range of that found in nature.

The repair region used in this work can represent implantation of tissue engineered constructs which typically have inferior mechanical properties in comparison to normal articular cartilage, for example with lower modulus and higher permeability [134-136]. The STZ has here been modeled as continuously attached to the adjacent normal cartilage, as might be achieved with sutures and fibrin glue. The reduction in von Mises stress gradients across the interface predicted here suggests that a quality STZ might improve the chances that such an initial attachment would be maintained during the healing process.

A two week non-weightbearing phase is recommended following ACI procedures to preserve the graft [137] as high loads early on would likely destroy transplanted materials. The literature does not offer experimental data representing normal resting loads, though one

computational study applied 37.5N for a knee [138]. Convergence may be an issue at higher loads without soft tissue contributions, particularly for models loaded by the rigid permeable surface.

A Poisson's ratio (ν) of zero was assigned to all tissues in this study as found experimentally and used in other finite element models [88,133,139]. This would have had little effect in compression as the normal compressive ν is already small in practice. In tension, this likely caused an underestimation of the positive effect of the STZ in protecting underlying tissues as this zone experienced the highest tensile stress in our study. A higher tensile ν for the STZ would have resulted in greater contraction and thus a greater decrease in strain-dependent permeability to better restrict fluid flow from that region and better protect the underlying tissue.

Contacting surfaces were all modeled as frictionless; a condition that would typically exist with pressurization of interstitial fluids as seen with loading by a rigid impermeable surface or by a normal cartilage layer. Low pressurization of surface fluids, as with loading via a rigid permeable surface, would greatly increase frictional forces at the articular surface and negatively impact tissue function throughout the tissue depth [25,54]. Inclusion of frictional forces for rigid permeable loading would likely have magnified the negative effects of this loading surface and its differences as compared to rigid impermeable and normal cartilage loading. Thus conclusions would not have differed and simplification of frictionless contact for all models was sufficient for this work.

For all models, a loading time of 30s was chosen as a point of evaluation to show how quickly the repair tissue would suffer under a small load. Also for the curved models, response to load was evaluated over time until equilibrium. The potential benefit of a protective STZ covering was evident for all levels of modeling but predictions were fine-tuned as model improvements were incorporated. Parabolic pressure loading showed that this protection

increased with increasing dependency of permeability on volumetric strain. Contact loading by rigid surfaces showed this same effect for permeable loading but revealed that increasing strain-dependent permeability had virtually no effect when loading with a totally impermeable surface. Also, contact loading showed that allowing load to redistribute over an increasing area of contact gave better estimates of changes between models. The unchanging load conditions existing with the parabolic pressure approach tended to overestimate relative differences between repair and normal conditions and to underestimate relative improvements from adding the protective covering. Replacing transverse isotropy with a bilinearly elastic material definition allowed departure from flat models to curved surfaces that more closely approximated normal diarthrodial joint geometry. It also allowed modeling some tension-compression nonlinearity in the normal middle and deep zones. A direct comparison of transversely isotropic versus bilinearly elastic definitions for flat models showed the latter approach provided more realistic predictions overall. Inclusion of finite deformation also contributed to these improvements. Finally, the ability to load curved models by a deformable layer representing normal cartilage provided the most realistic conditions of all and provided parameter predictions that often fell outside of the ranges predicted by the simpler rigidly loaded models. Two factors were mainly to cause for these improvements. First, the ability of the normal loading surface to deform resulted in greater contact areas than those that occurred with the rigid layers. Secondly, as would occur in normal joints, fluid exchange between the normal loading surface and the underlying models occurred as required to maintain fluid pressure continuity at the contact interface. Thus, conclusions from this work are best represented in predictions from the curved models.

The curved model findings predict that, compared to an isotropic repair, a STZ with normal nonlinear tension-compression properties and strain-dependent permeability in place over a repair tends to improve function in terms fluid pressure, stress, strain, and fluid flow patterns. Also, full thickness compression of the repaired cartilage layer with normal STZ will be reduced for all time points. Further, appreciably less deformation is predicted for loading by normal cartilage than with rigid layers, mainly because the deformable top layer distributes load over larger contact areas thereby involving more of the surrounding tissues. The effect of this can be seen in lower full thickness compression and lower fluid pressures for models loaded by normal cartilage overall, as compared to rigid surfaces. This also attenuated differences seen in fluid pressure between models when loaded normally, as compared to those that were rigidly loaded. This resulted in relative changes in fluid pressures that were less for normal loading than the range suggested by the two rigid surface loading extremes. Thus simulating loading via rigid surfaces at the permeable and impermeable extremes does not provide predictions which consistently bracket that which might be expected in vivo.

Improvements in engineered tissues are being achieved incrementally. While it is desirable to generate replacement tissues that mechanically perform as normal full thickness cartilage, it may be more achievable in the short-term to develop an STZ with normal mechanical properties. Procedures such as autologous chondrocyte transplantation (ACT) likely could benefit from a quality STZ. Efforts have already been made in recent years to find alternatives to periosteum coverings for ACT [140-144]. The development of a quality STZ could benefit scaffolding techniques as well.

Another benefit to incorporating normal STZ-like properties in a transplanted construct is suggested by the impact of loading on development of collagen organization. Computational

models have shown that tensile stress patterns due to various loading protocols correlate well with development of normal collagen fibril organization [138]. Stress shielding of the central region of repair models investigated here by surrounding normal tissue suggests that normal STZ-like collagen structure would not begin to develop in a homogenous implant during the normal non-weight bearing phase of healing. The random organization initiated in a homogenous implant during this phase may be hard to overcome during subsequent phases of gradually increasing loads. Thus, normal properties for the STZ may not only be critical to surviving the initial phase of healing but to eventual development of functional characteristics for the entire repair region.

Some have suggested that initial properties of engineered tissues may actually need properties other than normal to survive the healing process [48]. Finite element analyses can be helpful in defining these properties. A range of suitable finite element approaches exist for such analyses from models which incorporate a separate component for collagen to those, such as in this work, which simulate the effect of the collagen structure via property definitions [138,145].

While this work suggests that transplanted material with a quality STZ may be critical in achieving the long-term survival of repairing cartilage, it also highlights the need for models that more closely mimic in vivo conditions. Models developed here approximate those conditions by the use of nonlinear contact allowing fluid interaction between contacting surfaces, tension-compression nonlinearity in appropriate regions, and by accounting for finite deformation via nonlinear geometry. As they exist, these models can be helpful in studying the affect that varying existing model parameters (e.g. stiffnesses, Poisson's ratio, permeability, etc.) may have on transplanted materials. Additionally, future enhancements could involve added levels of anisotropy, variation in surface boundary conditions, simulation of incomplete integration

between implanted and surrounding tissues, inclusion of electro-chemical contributions, and the addition of other joint components (e.g. menisci, etc.). Thus, models developed in this work have the potential to provide needed guidance in identifying features critical to engineered tissues surviving the healing process and achieving normal functional characteristics of articular cartilage.

LITERATURE CITED

1. Bergmann G, Graichen F, Rohlmann A. Hip joint loading during walking and running, measured in two patients. *J Biomech*. 1993;26(8):969-990.

2. Bergmann G, Deuretzbacher G, Heller M, et al. Hip contact forces and gait patterns from routine activities. *J Biomech*. 2001;34(7):859-871.

3. Taylor WR, Heller MO, Bergmann G, Duda GN. Tibio-femoral loading during human gait and stair climbing. *J. Orthop. Res*. 2004;22(3):625-632.

4. Mow VC, Ratcliffe A, Poole AR. Cartilage and diarthrodial joints as paradigms for hierarchical materials and structures. *Biomaterials*. 1992;13(2):67-97.

5. Eyre D. Collagen of articular cartilage. *Arthritis Res*. 2002;4(1):30-35.

6. Wu JJ, Woods PE, Eyre DR. Identification of cross-linking sites in bovine cartilage type IX collagen reveals an antiparallel type II-type IX molecular relationship and type IX to type IX bonding. *J. Biol. Chem*. 1992;267(32):23007-23014.

7. Responte DJ, Natoli RM, Athanasiou KA. Collagens of articular cartilage: structure, function, and importance in tissue engineering. *Crit Rev Biomed Eng*. 2007;35(5):363-411.

8. Maroudas A, Bullough P. Permeability of articular cartilage. *Nature*. 1968;219(5160):1260-1261.

9. Weiss C, Rosenberg L, Helfet AJ. An ultrastructural study of normal young adult human articular cartilage. *J Bone Joint Surg Am*. 1968;50(4):663-674.

10. Mow VC, Proctor C, Kelly M. Biomechanics of articular cartilage. In: Nordin M, Frankel V, eds. *Basic biomechanics of the musculoskeletal system*. 2nd ed. Philadelphia: Lea & Febiger; 1989.

11. Baker JR, Caterson B. The isolation of "link proteins" from bovine nasal cartilage. *Biochim. Biophys. Acta*. 1978;532(2):249-258.

12. Hardingham TE. The role of link-protein in the structure of cartilage proteoglycan aggregates. *Biochem. J*. 1979;177(1):237-247.

13. Mow VC, Zhu W, Lai WM, et al. The influence of link protein stabilization on the viscometric properties of proteoglycan aggregate solutions. *Biochim. Biophys. Acta*. 1989;992(2):201-208.

14. Mankin HJ, Mow VC, Buckwalter JA, Iannotti J, Ratcliffe A. Form and Function of Articular Cartilage. In: Simon SR, ed. *Orthopaedic basic science*. [Rosemont Ill.]: American Academy of Orthopaedic Surgeons; 1994:1-44.

15. Buckwalter JA, Kuettner KE, Thonar EJ. Age-related changes in articular cartilage proteoglycans: electron microscopic studies. *J. Orthop. Res*. 1985;3(3):251-257.

16. Eisenberg S. Physical properties of articular cartilage from uniaxial confined compression. In: Maroudas A, Kuettner KE, eds. *Methods in cartilage research*. London ; San Diego: Academic Press; 1990.

17. Maroudas AI. Balance between swelling pressure and collagen tension in normal and degenerate cartilage. *Nature*. 1976;260(5554):808-809.

18. Lai WM, Hou JS, Mow VC. A triphasic theory for the swelling and deformation behaviors of articular cartilage. *J Biomech Eng*. 1991;113(3):245-258.

19. Muir H, Bullough P, Maroudas A. The distribution of collagen in human articular cartilage with some of its physiological implications. *J Bone Joint Surg Br*. 1970;52(3):554-563.

20. Lai WM, Mow VC. Drag-induced compression of articular cartilage during a permeation experiment. *Biorheology*. 1980;17(1-2):111-123.

21. Mansour JM, Mow VC. The permeability of articular cartilage under compressive strain and at high pressures. *J Bone Joint Surg Am*. 1976;58(4):509-516.

22. Mow V, Lai W, Holmes M. Advanced theoretical and experimental techniques in cartilage research. In: Huiskes R, VanCampen D, DeWijn J, eds. *Biomechanics: principle and applications*.Vol I.; 1982.

23. Chen AC, Bae WC, Schinagl RM, Sah RL. Depth- and strain-dependent mechanical and electromechanical properties of full-thickness bovine articular cartilage in confined compression. *J Biomech*. 2001;34(1):1-12.

24. Huang C-Y, Stankiewicz A, Ateshian GA, Mow VC. Anisotropy, inhomogeneity, and tension-compression nonlinearity of human glenohumeral cartilage in finite deformation. *J Biomech*. 2005;38(4):799-809.

25. Wayne JS. Load partitioning influences the mechanical response of articular cartilage. *Ann Biomed Eng*. 1995;23(1):40-47.

26. Mukherjee N, Wayne JS. Load sharing between solid and fluid phases in articular cartilage: I--Experimental determination of in situ mechanical conditions in a porcine knee. *J Biomech Eng*. 1998;120(5):614-619.

27. Mukherjee N, Wayne JS. Load sharing between solid and fluid phases in articular cartilage: II--Comparison of experimental results and u-p finite element predictions. *J Biomech Eng*. 1998;120(5):620-624.

28. Morales T, Kouri W, Nicolai M. New Horizon WORKSHOP 5 Chondrocyte Motility in Development and Disease. In: *Transactions of the 56th Annual Meeting of the Orthopaedic Research Society*.; 2010.

29. Mankin HJ. The response of articular cartilage to mechanical injury. *J Bone Joint Surg Am*. 1982;64(3):460-466.

30. Springfield D, Bolander M, Friedlaender G, Lane N. Molecular and Cellular Biology of Inflammation and Neoplasia. In: Simon SR, ed. *Orthopaedic basic science*. 1st ed. [Rosemont Ill.]: American Academy of Orthopaedic Surgeons; 1994:255.

31. Chiang H, Jiang C-C. Repair of articular cartilage defects: review and perspectives. *J. Formos. Med. Assoc*. 2009;108(2):87-101.

32. Jakob RP, Franz T, Gautier E, Mainil-Varlet P. Autologous osteochondral grafting in the knee: indication, results, and reflections. *Clin. Orthop. Relat. Res*. 2002;(401):170-184.

33. O'Driscoll SW, Fitzsimmons JS. The role of periosteum in cartilage repair. *Clin. Orthop. Relat. Res*. 2001;(391 Suppl):S190-207.

34. O'Driscoll SW, Keeley FW, Salter RB. Durability of regenerated articular cartilage produced by free autogenous periosteal grafts in major full-thickness defects in joint surfaces under the influence of continuous passive motion. A follow-up report at one year. *J Bone Joint Surg Am*. 1988;70(4):595-606.

35. Brittberg M, Lindahl A, Nilsson A, et al. Treatment of deep cartilage defects in the knee with autologous chondrocyte transplantation. *N. Engl. J. Med*. 1994;331(14):889-895.

36. Marlovits S, Zeller P, Singer P, Resinger C, Vécsei V. Cartilage repair: generations of autologous chondrocyte transplantation. *Eur J Radiol*. 2006;57(1):24-31.

37. Peterson L, Minas T, Brittberg M, et al. Two- to 9-year outcome after autologous chondrocyte transplantation of the knee. *Clin. Orthop. Relat. Res*. 2000;(374):212-234.

38. Butler DL, Goldstein SA, Guilak F. Functional tissue engineering: the role of biomechanics. *J Biomech Eng*. 2000;122(6):570-575.

39. Guilak F. Biomechanical factors in tissue engineering of articular cartilage. In: Goldberg V, Ebooks Corporation., ed. *Orthopedic Tissue Engineering*. Hoboken :: Informa Healthcare,; 2004.

40. Hung CT, Mauck RL, Wang CCB, Lima EG, Ateshian GA. A paradigm for functional tissue engineering of articular cartilage via applied physiologic deformational loading. *Ann Biomed Eng*. 2004;32(1):35-49.

41. Iwasa J, Engebretsen L, Shima Y, Ochi M. Clinical application of scaffolds for cartilage tissue engineering. *Knee Surg Sports Traumatol Arthrosc*. 2009;17(6):561-577.

42. Klein TJ, Malda J, Sah RL, Hutmacher DW. Tissue engineering of articular cartilage with biomimetic zones. *Tissue Eng Part B Rev*. 2009;15(2):143-157.

43. Ng KW, Ateshian GA, Hung CT. Zonal chondrocytes seeded in a layered agarose hydrogel create engineered cartilage with depth-dependent cellular and mechanical inhomogeneity. *Tissue Eng Part A*. 2009;15(9):2315-2324.

44. Revell CM, Athanasiou KA. Success rates and immunologic responses of autogenic, allogenic, and xenogenic treatments to repair articular cartilage defects. *Tissue Eng Part B Rev*. 2009;15(1):1-15.

45. Torzilli PA, Dethmers DA, Rose DE, Schryuer HF. Movement of interstitial water through loaded articular cartilage. *J Biomech*. 1983;16(3):169-179.

46. Torzilli PA. Effects of temperature, concentration and articular surface removal on transient solute diffusion in articular cartilage. *Med Biol Eng Comput*. 1993;31 Suppl:S93-98.

47. Glaser C, Putz R. Functional anatomy of articular cartilage under compressive loading Quantitative aspects of global, local and zonal reactions of the collagenous network with respect to the surface integrity. *Osteoarthr. Cartil*. 2002;10(2):83-99.

48. Frank CB, Shrive NG, Boorman RS, Lo IKY, Hart DA. New perspectives on bioengineering of joint tissues: joint adaptation creates a moving target for engineering replacement tissues. *Ann Biomed Eng*. 2004;32(3):458-465.

49. Ionescu L, Garcia G, Zachary T, et al. In vitro meniscus integration potential is inversely correlatedwith tissue maturation state. In: *Proceedings of the ASME 2010 Summer Bioengineering Conference*.; 2010.

50. Mizrahi J, Maroudas A, Lanir Y, Ziv I, Webber TJ. The "instantaneous" deformation of cartilage: effects of collagen fiber orientation and osmotic stress. *Biorheology*. 1986;23(4):311-330.

51. Roth V, Mow VC. The intrinsic tensile behavior of the matrix of bovine articular cartilage and its variation with age. *J Bone Joint Surg Am*. 1980;62(7):1102-1117.

52. Jeffery AK, Blunn GW, Archer CW, Bentley G. Three-dimensional collagen architecture in bovine articular cartilage. *J Bone Joint Surg Br*. 1991;73(5):795-801.

53. Below S, Arnoczky SP, Dodds J, Kooima C, Walter N. The split-line pattern of the distal femur: A consideration in the orientation of autologous cartilage grafts. *Arthroscopy*. 2002;18(6):613-617.

54. Krishnan R, Park S, Eckstein F, Ateshian GA. Inhomogeneous cartilage properties enhance superficial interstitial fluid support and frictional properties, but do not provide a homogeneous state of stress. *J Biomech Eng*. 2003;125(5):569-577.

55. Armstrong CG, Lai WM, Mow VC. An analysis of the unconfined compression of articular cartilage. *J Biomech Eng*. 1984;106(2):165-173.

56. Mak AF, Lai WM, Mow VC. Biphasic indentation of articular cartilage--I. Theoretical analysis. *J Biomech*. 1987;20(7):703-714.

57. Mow VC, Guo XE. Mechano-electrochemical properties of articular cartilage: their inhomogeneities and anisotropies. *Annu Rev Biomed Eng*. 2002;4:175-209.

58. Mow VC, Kuei SC, Lai WM, Armstrong CG. Biphasic creep and stress relaxation of articular cartilage in compression? Theory and experiments. *J Biomech Eng*. 1980;102(1):73-84.

59. Armstrong CG, Mow VC. Variations in the intrinsic mechanical properties of human articular cartilage with age, degeneration, and water content. *J Bone Joint Surg Am*. 1982;64(1):88-94.

60. Lyyra T, Kiviranta I, Väätäinen U, Helminen HJ, Jurvelin JS. In vivo characterization of indentation stiffness of articular cartilage in the normal human knee. *J. Biomed. Mater. Res*. 1999;48(4):482-487.

61. Woo SL, Akeson WH, Jemmott GF. Measurements of nonhomogeneous, directional mechanical properties of articular cartilage in tension. *J Biomech*. 1976;9(12):785-791.

62. Jurvelin JS, Buschmann MD, Hunziker EB. Optical and mechanical determination of Poisson's ratio of adult bovine humeral articular cartilage. *J Biomech*. 1997;30(3):235-241.

63. Wang CC-B, Chahine NO, Hung CT, Ateshian GA. Optical determination of anisotropic material properties of bovine articular cartilage in compression. *J Biomech*. 2003;36(3):339-353.

64. Arokoski JP, Hyttinen MM, Helminen HJ, Jurvelin JS. Biomechanical and structural characteristics of canine femoral and tibial cartilage. *J. Biomed. Mater. Res*. 1999;48(2):99-107.

65. LeRoux MA, Arokoski J, Vail TP, et al. Simultaneous changes in the mechanical properties, quantitative collagen organization, and proteoglycan concentration of articular cartilage following canine meniscectomy. *J. Orthop. Res*. 2000;18(3):383-392.

66. Korhonen RK, Wong M, Arokoski J, et al. Importance of the superficial tissue layer for the indentation stiffness of articular cartilage. *Med Eng Phys*. 2002;24(2):99-108.

67. Kiviranta P, Rieppo J, Korhonen RK, et al. Collagen network primarily controls Poisson's ratio of bovine articular cartilage in compression. *J. Orthop. Res*. 2006;24(4):690-699.

68. Töyräs J, Nieminen HJ, Laasanen MS, et al. Ultrasonic characterization of articular cartilage. *Biorheology*. 2002;39(1-2):161-169.

69. Saarakkala S, Korhonen RK, Laasanen MS, et al. Mechano-acoustic determination of Young's modulus of articular cartilage. *Biorheology*. 2004;41(3-4):167-179.

70. Nieminen HJ, Töyräs J, Laasanen MS, Jurvelin JS. Acoustic properties of articular cartilage under mechanical stress. *Biorheology*. 2006;43(3-4):523-535.

71. Gründer W, Kanowski M, Wagner M, Werner A. Visualization of pressure distribution within loaded joint cartilage by application of angle-sensitive NMR microscopy. *Magn Reson Med*. 2000;43(6):884-891.

72. Wayne JS, Kraft KA, Shields KJ, et al. MR imaging of normal and matrix-depleted cartilage: correlation with biomechanical function and biochemical composition. *Radiology*. 2003;228(2):493-499.

73. Gründer W. MRI assessment of cartilage ultrastructure. *NMR Biomed*. 2006;19(7):855-876.

74. Julkunen P, Korhonen RK, Nissi MJ, Jurvelin JS. Mechanical characterization of articular cartilage by combining magnetic resonance imaging and finite-element analysis—a potential functional imaging technique. *Phys. Med. Biol.* 2008;53(9):2425-2438.

75. Little RB, Wevers HW, Siu D, Cooke TD. A three-dimensional finite element analysis of the upper tibia. *J Biomech Eng*. 1986;108(2):111-119.

76. Carter DR, Wong M. Modelling cartilage mechanobiology. *Philos. Trans. R. Soc. Lond., B, Biol. Sci*. 2003;358(1437):1461-1471.

77. Julkunen P, Harjula T, Marjanen J, Helminen HJ, Jurvelin JS. Comparison of single-phase isotropic elastic and fibril-reinforced poroelastic models for indentation of rabbit articular cartilage. *J Biomech*. 2009;42(5):652-656.

78. Ateshian GA, Ellis BJ, Weiss JA. Equivalence between short-time biphasic and incompressible elastic material responses. *J Biomech Eng*. 2007;129(3):405-412.

79. Terzaghi K. *Erdbau Mechanik auf Bodenphysikalischer Grundlage*. Deuticke, Vienna; 1925.

80. Biot MA. General Theory of Three-Dimensional Consolidation. *J. Appl. Phys.* 1941;12(2):155.

81. Levenston M, Frank E, Grodzinsky AJ. Variationally derived 3-field finite element formulations for quasistatic poroelastic analysis of hydrated biological tissues. *Computer Methods in Applied Mechanics and Engineering*. 1998;156(1-4):231-246.

82. Cohen B, Gardner T, Ateshian GA. The influence of transverse isotropy on cartilage indentation behavior: a study of the human humeral head. In: *Transactions of the 39th Annual Meeting of the Orthopaedic Research Society*.; 1993.

83. Donzelli PS, Spilker RL, Ateshian GA, Mow VC. Contact analysis of biphasic transversely isotropic cartilage layers and correlations with tissue failure. *J Biomech*. 1999;32(10):1037-1047.

84. Garcia JJ, Altiero NJ, Haut RC. Estimation of in situ elastic properties of biphasic cartilage based on a transversely isotropic hypo-elastic model. *J Biomech Eng*. 2000;122(1):1-8.

85. Mow V, Good P, Gardner T. A new method to determine the tensile properties of articular cartilage using the indentation test. In: *Transactions of the 46th Annual Meeting of the Orthopaedic Research Society*.; 2000.

86. Gardner T, Xin L, Mow V. Validation of articular cartilage tensile moduli from transversely isotropic biphasic indentation FEM analysis. In: *Proceedings of the ASME 2003 Summer Bioengineering Conference*.; 2003.

87. Curnier A, He Q-C, Zysset P. Conewise linear elastic materials. *J Elasticity*. 1995;37(1):1-38.

88. Soltz MA, Ateshian GA. A Conewise Linear Elasticity mixture model for the analysis of tension-compression nonlinearity in articular cartilage. *J Biomech Eng*. 2000;122(6):576-586.

89. Li LP, Soulhat J, Buschmann MD, Shirazi-Adl A. Nonlinear analysis of cartilage in unconfined ramp compression using a fibril reinforced poroelastic model. *Clin Biomech (Bristol, Avon)*. 1999;14(9):673-682.

90. Korhonen RK, Laasanen MS, Töyräs J, et al. Fibril reinforced poroelastic model predicts specifically mechanical behavior of normal, proteoglycan depleted and collagen degraded articular cartilage. *J Biomech*. 2003;36(9):1373-1379.

91. Wilson W, van Donkelaar CC, van Rietbergen B, Ito K, Huiskes R. Stresses in the local collagen network of articular cartilage: a poroviscoelastic fibril-reinforced finite element study. *J Biomech*. 2004;37(3):357-366.

92. Mak AF. Unconfined compression of hydrated viscoelastic tissues: a biphasic poroviscoelastic analysis. *Biorheology*. 1986;23(4):371-383.

93. Suh JK, Bai S. Finite element formulation of biphasic poroviscoelastic model for articular cartilage. *J Biomech Eng*. 1998;120(2):195-201.

94. Huang CY, Mow VC, Ateshian GA. The role of flow-independent viscoelasticity in the biphasic tensile and compressive responses of articular cartilage. *J Biomech Eng*. 2001;123(5):410-417.

95. Holmes MH, Mow VC. The nonlinear characteristics of soft gels and hydrated connective tissues in ultrafiltration. *J Biomech*. 1990;23(11):1145-1156.

96. Garcia J, Cortes D. A nonlinear biphasic viscohyperelastic model for articular cartilage. *Journal of Biomechanics*. 2006;39(16):2991-2998.

97. Lai WM, Mow VC, Roth V. Effects of nonlinear strain-dependent permeability and rate of compression on the stress behavior of articular cartilage. *J Biomech Eng*. 1981;103(2):61-66.

98. Holmes MH, Lai WM, Mow VC. Singular perturbation analysis of the nonlinear, flow-dependent compressive stress relaxation behavior of articular cartilage. *J Biomech Eng*. 1985;107(3):206-218.

99. Almeida ES, Spilker RL. Mixed and Penalty Finite Element Models for the Nonlinear Behavior of Biphasic Soft Tissues in Finite Deformation: Part I - Alternate Formulations. *Comput Methods Biomech Biomed Engin*. 1997;1(1):25-46.

100. Almeida ES, Spilker RL. Mixed and Penalty Finite Element Models for the Nonlinear Behavior of Biphasic Soft Tissues in Finite Deformation: Part II - Nonlinear Examples. *Comput Methods Biomech Biomed Engin*. 1998;1(2):151-170.

101. Olsen S, Oloyede A, Adam C. A finite element formulation and program to study transient swelling and load-carriage in healthy and degenerate articular cartilage. *Comput Methods Biomech Biomed Engin*. 2004;7(2):111-120.

102. Li LP, Buschmann MD, Shirazi-Adl A. A fibril reinforced nonhomogeneous poroelastic model for articular cartilage: inhomogeneous response in unconfined compression. *J Biomech*. 2000;33(12):1533-1541.

103. Adeeb SM, Sayed Ahmed EY, Matyas J, et al. Congruency effects on load bearing in diarthrodial joints. *Comput Methods Biomech Biomed Engin*. 2004;7(3):147-157.

104. Warner M, Taylor W, Clift S. A method for determining contact between a non-porous surface and articular cartilage in a biphasic FE model. In: Middleton J, Jones M, Shrive N, Pande N, eds. *Computer methods in biomechanics & biomedical engineering 3*. Amsterdam: Gordon & Breach; 2001:208-212.

105. Warner MD, Taylor WR, Clift SE. Cyclic loading moves the peak stress to the cartilage surface in a biphasic model with isotropic solid phase properties. *Med Eng Phys*. 2004;26(3):247-249.

106. Wayne JS, Woo SL, Kwan MK. Finite element analyses of repaired articular surfaces. *Proc Inst Mech Eng H*. 1991;205(3):155-162.

107. Wayne JS, Woo SL, Kwan MK. Application of the u-p finite element method to the study of articular cartilage. *J Biomech Eng*. 1991;113(4):397-403.

108. Hunter CJ, Levenston ME. The influence of repair tissue maturation on the response to oscillatory compression in a cartilage defect repair model. *Biorheology*. 2002;39(1-2):79-88.

109. Hale JE, Rudert MJ, Brown TD. Indentation assessment of biphasic mechanical property deficits in size-dependent osteochondral defect repair. *J Biomech*. 1993;26(11):1319-1325.

110. Smith CL, Mansour JM. Indentation of an osteochondral repair: sensitivity to experimental variables and boundary conditions. *J Biomech*. 2000;33(11):1507-1511.

111. Spoon CE, Wayne JS. Influence of aspect ratios on the creep behaviour of articular cartilage in indentation. *Comput Methods Biomech Biomed Engin*. 2004;7(1):17-23.

112. Wu JZ, Herzog W, Hasler EM. Inadequate placement of osteochondral plugs may induce abnormal stress-strain distributions in articular cartilage --finite element simulations. *Med Eng Phys*. 2002;24(2):85-97.

113. Papaioannou G, Demetropoulos CK, King YH. Predicting the effects of knee focal articular surface injury with a patient-specific finite element model. *Knee*. 2010;17(1):61-68.

114. Kelly DJ, Prendergast PJ. Mechano-regulation of stem cell differentiation and tissue regeneration in osteochondral defects. *J Biomech*. 2005;38(7):1413-1422.

115. Mononen ME, Julkunen P, Töyräs J, et al. Alterations in structure and properties of collagen network of osteoarthritic and repaired cartilage modify knee joint stresses. *Biomech Model Mechanobiol*. 2010. Available at: http://www.ncbi.nlm.nih.gov/pubmed/20628782.

116. Smith C, Goldberg V, Mansour J. Analysis of the mechanical environment in a repairing osteochondral defect. In: *Transactions of the 47th Annual Meeting of the Orthopaedic Research Society*.; 2001.

117. Wu JZ, Herzog W, Epstein M. Evaluation of the finite element software ABAQUS for biomechanical modelling of biphasic tissues. *J Biomech*. 1998;31(2):165-169.

118. Soslowsky LJ, Flatow EL, Bigliani LU, Mow VC. Articular geometry of the glenohumeral joint. *Clin. Orthop. Relat. Res*. 1992;(285):181-190.

119. Dowson D, Unsworth A, Cooke A, Gvozdanovic D. Lubrication of Joints. In: Dowson D, Wright V, eds. *An Introduction to the bio-mechanics of joints and joint replacement*. London: Mechanical Engineering Publications; 1981.

120. Benjamin J Ellis and Ateshian GA, Anderson AE, Canal C, Maas SA, Jeffrey A Weiss. Effects of joint congruency on the response of a tension-compression nonlinear constitutive model for cartilage. In: *Proceedings of the ASME 2008 Summer Bioengineering Conference*.; 2008.

121. Li LP, Buschmann MD, Shirazi-Adl A. Strain-rate dependent stiffness of articular cartilage in unconfined compression. *J Biomech Eng*. 2003;125(2):161-168.

122. Owen JR, Wayne JS. Influence of a superficial tangential zone over repairing cartilage defects: implications for tissue engineering. *Biomech Model Mechanobiol*. 2006;5(2-3):102-110.

123. Owen JR, Wayne JS. Influence of the superficial tangential zone cartilage under contact loading: implications for tissue engineering efforts. In: *Proceedings of the ASME 2006 Summer Bioengineering Conference*.; 2006.

124. Owen JR, Wayne JS. Influence of the superficial tangential zone for cartilage modeled in finite deformation and with tension/compression nonlinearity. In: *Proceedings of the ASME 2008 Summer Bioengineering Conference*.; 2008.

125. Owen JR, Wayne JS. Contact models of repaired articular surfaces: influence of loading conditions and the superficial tangential zone. *Biomech Model Mechanobiol*. 2010. Available at: http://www.ncbi.nlm.nih.gov/pubmed/20700624.

126. Getgood A, Brooks R, Fortier L, Rushton N. Articular cartilage tissue engineering: today's research, tomorrow's practice? *J Bone Joint Surg Br*. 2009;91(5):565-576.

127. Vinatier C, Mrugala D, Jorgensen C, Guicheux J, Noël D. Cartilage engineering: a crucial combination of cells, biomaterials and biofactors. *Trends Biotechnol*. 2009;27(5):307-314.

128. Ateshian GA. Artificial cartilage: Weaving in three dimensions. *Nat Mater*. 2007;6(2):89-90.

129. Moutos FT, Freed LE, Guilak F. A biomimetic three-dimensional woven composite scaffold for functional tissue engineering of cartilage. *Nat Mater*. 2007;6(2):162-167.

130. Moutos FT, Guilak F. Composite scaffolds for cartilage tissue engineering. *Biorheology*. 2008;45(3-4):501-512.

131. Setton LA, Zhu W, Mow VC. The biphasic poroviscoelastic behavior of articular cartilage: role of the surface zone in governing the compressive behavior. *J Biomech*. 1993;26(4-5):581-592.

132. van der Voet A. A comparison of finite element codes for the solution of biphasic poroelastic problems. *Proc Inst Mech Eng H*. 1997;211(2):209-211.

133. Wilson W, van Rietbergen B, van Donkelaar CC, Huiskes R. Pathways of load-induced cartilage damage causing cartilage degeneration in the knee after meniscectomy. *J Biomech*. 2003;36(6):845-851.

134. Martin I, Obradovic B, Treppo S, et al. Modulation of the mechanical properties of tissue engineered cartilage. *Biorheology*. 2000;37(1-2):141-147.

135. Toolan BC, Frenkel SR, Pachence JM, Yalowitz L, Alexander H. Effects of growth-factor-enhanced culture on a chondrocyte-collagen implant for cartilage repair. *J. Biomed. Mater. Res.* 1996;31(2):273-280.

136. Xu J-W, Zaporojan V, Peretti GM, et al. Injectable tissue-engineered cartilage with different chondrocyte sources. *Plast. Reconstr. Surg.* 2004;113(5):1361-1371.

137. Nho SJ, Pensak MJ, Seigerman DA, Cole BJ. Rehabilitation after autologous chondrocyte implantation in athletes. *Clin Sports Med*. 2010;29(2):267-282, viii.

138. Wilson W, Driessen NJB, van Donkelaar CC, Ito K. Prediction of collagen orientation in articular cartilage by a collagen remodeling algorithm. *Osteoarthr. Cartil*. 2006;14(11):1196-1202.

139. Jurvelin JS, Arokoski JP, Hunziker EB, Helminen HJ. Topographical variation of the elastic properties of articular cartilage in the canine knee. *J Biomech*. 2000;33(6):669-675.

140. Bartlett W, Gooding CR, Carrington RWJ, et al. Autologous chondrocyte implantation at the knee using a bilayer collagen membrane with bone graft. A preliminary report. *J Bone Joint Surg Br*. 2005;87(3):330-332.

141. Cherubino P, Grassi FA, Bulgheroni P, Ronga M. Autologous chondrocyte implantation using a bilayer collagen membrane: a preliminary report. *J Orthop Surg (Hong Kong)*. 2003;11(1):10-15.

142. Ho STB, Hutmacher DW, Ekaputra AK, Hitendra D, Hui JH. The evaluation of a biphasic osteochondral implant coupled with an electrospun membrane in a large animal model. *Tissue Eng Part A*. 2010;16(4):1123-1141.

143. McNickle AG, Provencher MT, Cole BJ. Overview of existing cartilage repair technology. *Sports Med Arthrosc*. 2008;16(4):196-201.

144. Ronga M, Grassi FA, Bulgheroni P. Arthroscopic autologous chondrocyte implantation for the treatment of a chondral defect in the tibial plateau of the knee. *Arthroscopy*. 2004;20(1):79-84.

145. Ateshian GA, Rajan V, Chahine NO, Canal CE, Hung CT. Modeling the matrix of articular cartilage using a continuous fiber angular distribution predicts many observed phenomena. *J Biomech Eng*. 2009;131(6):061003.

APPENDIX A

Parameters required to define linearly elastic materials in Abaqus.

Linear elastic material behavior is defined in Abaqus as $\boldsymbol{\sigma} = \boldsymbol{D^{el}\varepsilon^{el}}$ where $\boldsymbol{\sigma}$ is the total stress, $\boldsymbol{\varepsilon^{el}}$ is the total elastic strain, and $\boldsymbol{D^{el}}$ is the 4th order elasticity tensor, or stiffness matrix (ABAQUS Analysis User's Manual, Section 18.2.1).

Nine material engineering constants are needed to define an orthotropic material:

$$\begin{Bmatrix}\sigma_{11}\\ \sigma_{22}\\ \sigma_{33}\\ \sigma_{12}\\ \sigma_{13}\\ \sigma_{23}\end{Bmatrix} = \begin{bmatrix} D_{1111} & D_{1122} & D_{1133} & 0 & 0 & 0 \\ & D_{2222} & D_{2233} & 0 & 0 & 0 \\ & & D_{3333} & 0 & 0 & 0 \\ & & & D_{1212} & 0 & 0 \\ & sym & & & D_{1313} & 0 \\ & & & & & D_{2323} \end{bmatrix} \begin{Bmatrix}\varepsilon_{11}\\ \varepsilon_{22}\\ \varepsilon_{33}\\ \gamma_{12}\\ \gamma_{13}\\ \gamma_{23}\end{Bmatrix}$$

Those material constants are defined as follows:

$$D_{1111} = E_1(1 - \nu_{23}\nu_{32})\Upsilon$$

$$D_{2222} = E_2(1 - \nu_{13}\nu_{31})\Upsilon$$

$$D_{3333} = E_3(1 - \nu_{12}\nu_{21})\Upsilon$$

$$D_{1122} = E_1(\nu_{21} + \nu_{31}\nu_{23})\Upsilon = E_2(\nu_{12} + \nu_{32}\nu_{13})\Upsilon$$

$$D_{1133} = E_1(\nu_{31} + \nu_{21}\nu_{32})\Upsilon = E_3(\nu_{13} + \nu_{12}\nu_{23})\Upsilon$$

$$D_{2233} = E_2(\nu_{32} + \nu_{12}\nu_{31})\Upsilon = E_3(\nu_{23} + \nu_{21}\nu_{13})\Upsilon$$

$$D_{1212} = G_{12}$$

$$D_{1313} = G_{13}$$

$$D_{2323} = G_{23}$$

Where $\Upsilon = \frac{1}{1-\nu_{12}\nu_{21}-\nu_{23}\nu_{32}-\nu_{31}\nu_{13}-2\nu_{21}\nu_{32}\nu_{13}}$

For material stability, these parameters must satisfy the following restrictions:

$D_{1111}, D_{2222}, D_{3333}, D_{1212}, D_{1313}, D_{2323} > 0$

$|D_{1122}| < (D_{1111}D_{2222})^{1/2}$

$|D_{1133}| < (D_{1111}D_{3333})^{1/2}$

$|D_{2233}| < (D_{2222}D_{3333})^{1/2}$

$det(D^{el}) > 0$, which leads to:

$$D_{1111}D_{2222}D_{3333} + 2D_{1122}D_{1133}D_{2233} - D_{2222}{D_{1133}}^2 - D_{1111}{D_{2233}}^2 - D_{3333}{D_{1122}}^2 > 0$$

VITA

John Russell Owen was born on May 7, 1956, in Richmond, Virginia and is an American citizen. He was raised in the town of Jarratt, Virginia and graduated from Greensville County High School, Emporia, Virginia in June, 1974. He received his Bachelor of Science in Mechanical Engineering from the University of Virginia, Charlottesville, Virginia in May 1981. After graduation, he worked for 17 years in numerous engineering capacities for Philip Morris, Richmond, Virginia where he became a licensed Professional Engineer and a certified Quality Engineer. In 1998, John left a successful career in industry to pursue his interests in Biomedical Engineering. Since 1999, he has been working full-time in Orthopaedic Research at Virginia Commonwealth University where he has co-authored 25 published papers. In the fall of 2006, he officially enrolled in the Master of Science program at Virginia Commonwealth University. In 2009, John was inducted into The Honor Society of Phi Kappa Phi and the VCU chapter of Alpha Eta Mu Beta National Biomedical Engineering Honor Society. Portions of the work related to his graduate studies have been presented at the American Society of Mechanical Engineer's Summer Bioengineering Conferences in 2006, 2008, and 2009 and at the Orthopaedic Research Society's annual meetings in 2006 and 2009. Also, portions have been published in the journal of *Biomechanics and Modeling in Mechanobiology* in 2006 and 2010. Following graduation, John will continue his work in Orthopaedic Research and desires to pursue of a Doctoral degree in Biomedical Engineering at Virginia Commonwealth University.